A Search for Dark Matter with the Large Underground Xenon Detector

By

JEREMY ALLEN MOCK
B.S. (Case Western Reserve University) 2008

DISSERTATION

Submitted in partial satisfaction of the requirements for the degree of

DOCTOR OF PHILOSOPHY

in

Physics

in the

OFFICE OF GRADUATE STUDIES

of the

UNIVERSITY OF CALIFORNIA

DAVIS

Approved:

S. Mani Tripathi, Chair

Robert Svoboda

Manuel Calderon de la Barca Sanchez

Committee in Charge

2014

To my family and friends for their help and support throughout.

CONTENTS

List of Figures

List of Tables

ABSTRACT

A Search for Dark Matter with the Large Underground Xenon Detector

The Weakly Interacting Massive Particles (WIMP) has been postulated as a candidate that constitutes dark matter, which dominates the matter density in the universe. The Large Underground Xenon (LUX) detector is a 370 kg (112 kg fiducial) dual-phase xenon time projection chamber operating 4,850 feet underground at the Sanford Underground Research Facility in Lead, South Dakota with the goal of detecting WIMPs. A refined understanding of detector response is required in order to make such searches more sophisticated. The LUX simulation includes a new physics model, the Noble Element Simulation Technique, which accurately predicts the scintillation and ionization yields as well as the prompt and electroluminescence pulse shapes in xenon. These models, combined with a new technique for in-situ, low-energy neutron calibration, allow for the extension of the WIMP detection regime into a lower-energy region. A novel analysis technique for the removal of spurious, high-rate background events facilitates the reduction of conservative analysis thresholds. Both of these improvements, which lead to an increased sensitivity of LUX to low-mass WIMPs, are described in this thesis. While no discovery is reported, this work establishes the most stringent 90% confidence level upper limit on the WIMP-nucleon cross-section of 7.43×10^{-46} cm^2 for a WIMP with mass 33 GeV/c^2.

ACKNOWLEDGMENTS

I would like to begin by acknowledging my research advisor, Mani Tripathi, for the countless hours we spent together going through plots and ideas. The experience working with him taught me what it means to really be an experimental physicist. His knowledge and wisdom also helped me to keep things in perspective and to understand what is most important to me in life. The time working with him was valuable and irreplaceable. I would also like to thank Robert Svoboda for the time he was willing to spend talking with me. His endless supply of new ideas kept the group moving at times, and I can only hope some of his creativity rubbed off on me.

I would never have finished this work without the help of Matthew Szydagis. His drive and motivation to succeed and do what is right exemplifies academic integrity, and his encyclopedic knowledge of all things xenon is unmatched. I would like to thank Richard Ott for his guidance on code writing and advanced statistics and mathematics. And Aaron Manalaysay, who has more experience in this field than all of us. All three of these people were vital to my success.

I would like to thank my core group of friends who I rely upon to keep me sane outside of the office, especially John Crocker, Miles Frampton, Mike Squires, and Justin Dhooghe. I do not know how I would have made it through without our football and television watching sessions. Of course, I should not forget those friends who have moved on, like Kevin Glynn and David Cross, who were around during first year problem sets. I wish you all the best.

To my office mates, Mike Woods, John Felde, Nick Walsh, and Sergey Uvarov, thank you for the quiet days and the noisy days. Thank you for the physics discussions and the analysis discussions. Thank you for all the help you provided.

To the LUX South Dakota group, living on site without Patrick Phelps, Attila Dobi, Markus Horn, Rachel Mannino and Carmen Carmona would not have been the same. Those nine months were a lot of fun, and I wouldn't give them up for anything.

To my parents and sister, who bet on how long I would be here, I just want to point out that you all lost. You all severely underestimated my time. But thank you for weekly phone calls and visits and support. And to Wei, thank you for being with me at the end and helping

me get through the process of writing down my work. Just being there was enough, and you surpassed it. For that I am forever grateful.

And for anyone I might have forgotten to mention, thank you too! My work is a reflection of the influence each of you has had on me, as am I, and I am forever in your debt.

Chapter 1

Dark Matter

Preamble

I began working on a dark matter search experiment as an undergraduate at Case Western Reserve University. In fact, I still remember the look of joy on the face of my advisor when he entered the laboratory and announced that the project known as the Large Underground Xenon detector had been funded. Of course, at that time I knew very little about the physics, but I became enamored with the detector technology and how it all worked. I knew that this was a project I wanted to continue working on.

And continue working on it I did. I entered graduate school to continue my education. As I learned more of the physics of dark matter, I became even more captivated. I also was able to contribute heavily to the design and construction of the detector, a very exciting experience for me. During my graduate-school tenure, results from various experiments began to come out claiming discovery of low-mass dark-matter particles. I became very interested in this idea, and I wanted to pursue it as my thesis topic.

Below I will present my own investigation into the existence of these particles, using a large xenon detector deployed in the Black Hills of South Dakota. The experience has not always been easy, but it has certainly been rewarding. I am excited to close this chapter of my life, and I am excited for what the next has in store.

1.1 Evidence for the Existence of Dark Matter

Throughout the course of history, scientists have looked to the stars to learn about the properties of the universe in which we reside. Upon careful study, evidence began to emerge that some of the mass in the universe was not visible by detection of electromagnetic radiation. This matter, which does not emit light is referred to as dark matter, and it must exist in some form to explain these observations.

1.1.1 Early Indications

An interesting astronomical parameter is the existence of a well defined relationship between the brightness of an object and the mass of that object. In fact, using the mass of the sun as a standard, measuring the luminosity of a distant object can provide an excellent estimation of the mass contained within. This has been the technique astronomers have used to determine the mass of distant galaxies and clusters of galaxies, and it was not until the early 1930s that any issues with this technique were discovered.

Fritz Zwicky was one of the first to make such an observation. He noted that because the mass-to-light ratio depended on the type of star being observed, the technique was useful for measuring the mass of a single star or a small number of stars, but it became increasingly inaccurate when one is studying galaxies or clusters of galaxies. In these cases, an estimation of the population density of each class of star must be made. While studying the Coma cluster of galaxies, Zwicky utilized a different technique for measuring the mass of the cluster. He measured the doppler shifts of the galactic spectra to determine v_s, the velocity component along the line-of-sight, for each of the galaxies. For a spherically symmetric velocity distribution, however, the magnitude of the total velocity, v, can be estimated as $\overline{v^2} = 3\overline{v_s^2}$ [1]. Assuming basic Newtonian gravity, Zwicky used the virial theorem to equate the measured velocity dispersion of the member galaxies with the mass of the cluster. He discovered that the luminosity method indicated a mass which was approximately 10% of that measured from velocity dispersion. He concluded that the majority of the mass contained within a galaxy must be non-luminous [1].

1.1.2 Galactic Rotation Curves

Some 40 years later, Vera Rubin and her colleagues continued to investigate the non-luminous matter by studying the velocity dispersions of components within a single galaxy. Newtonian dynamics states that the gravitational force is directly proportional to the mass of the object and inversely proportional to r^2, its distance from the gravitational center:

$$F_g = \frac{GmM(r)}{r^2}. \tag{1.1}$$

Here, m is the gravitational mass of the object and $M(r)$ is the mass contained within some radius r. Assuming a circular orbit and spherical symmetry, the centripetal force can be equated with the gravitational force to derive a relationship between rotational velocity, contained mass, and radius as

$$v = \sqrt{\frac{GM(r)}{r}} \tag{1.2}$$

As shown in Figure 1.1 for galaxy NGC 5603 [2], rotational velocity initially increases with radius as more and more mass is included within its orbit. However, as radius increases beyond the edge of visible matter, the rotational velocity should decrease in a simple relationship given by $v \propto 1/\sqrt{r}$, following the *Luminous* plus *Gas* curves in Figure 1.1.

Rubin sought to demonstrate this [3] by studying 60 isolated galaxies that were aligned such that stars on one side of the galactic center were moving away from the observer while stars on the other side were moving toward the observer. The stars themselves proved too faint to measure accurately, so spectral lines from clouds of hydrogen gas near stars were measured to obtain the rotational velocities, again from the doppler shifts. The observed rotational velocities deviated from what was expected from (1.2). Rather than decrease with increasing radius, the velocities of objects continued to increase and eventually reached an asymptote at large radii. A similar observation, from [2], is shown in Figure 1.1 as the data points. Her data allowed Rubin to conclude that the luminous distribution of a galaxy is not a guide to the mass distribution of the galaxy, and that an additional, non-luminous matter distribution with behavior shown in Figure 1.1 as the *Dark matter* curve must be present in order explain the behavior.

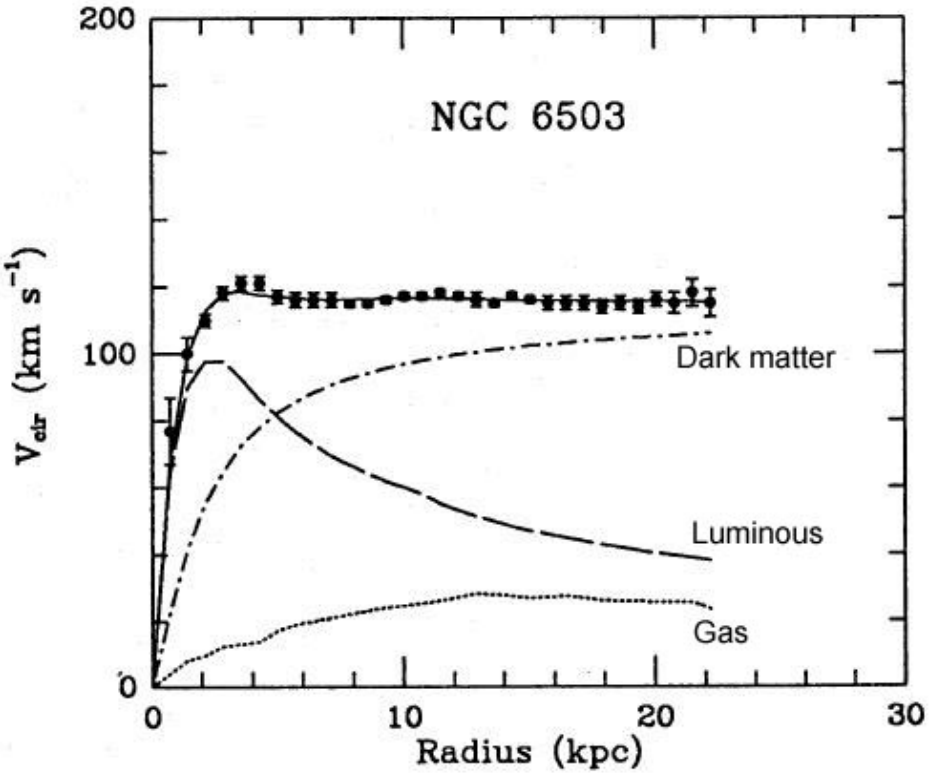

Figure 1.1. An example of the expected and measured rotational velocity curves as measured by Begeman, Broels and Sanders [2]. The *Luminous* plus *Gas* curves show the expected behavior of the galactic objects, assuming the luminous matter is the source of the dominant gravitational effect. The data points show the observed behavior. Data similar to this led Rubin to postulate that the luminous distribution of a galaxy is not a guide to the mass distribution of the galaxy, and that an additional, non-luminous matter distribution with behavior shown as the *Dark matter* curve must be present [3].

1.1.3 Colliding Galaxies

The previously presented evidence supporting the existence of non-luminous matter assumes that Newtonian dynamics applies on galactic scales. It is well measured that gravity behaves in this way on scales similar to the size of the solar system, but the galactic evidence of Zwicky and Rubin can be explained by modifying Newtonian gravity for larger scales [4]. The collision between two clusters of galaxies provides an opportunity to test the idea of a modified dynamics as opposed to dark matter.

A cluster of galaxies contains both galaxies and a large amount of intergalactic gas, with the majority of the luminous matter existing as intergalactic gas. Within a galaxy cluster, the constituent components acquire similar, centrally symmetric spatial distributions according to the gravitational potential. When two such clusters collide, the individual galaxies do not interact with each other, but the intergalactic particles experience high pressures from the collisions which cause atomic excitations and subsequent de-excitations, emitting observable X-rays. The collisions experienced by the intergalactic particles cause the galaxies within each of the clusters to decouple from the intergalactic gas. An example system is 1E 0657558, where such a collision is clear [5].

The gravitational potential of a galactic system can be measured using a weak lensing technique. It involves measuring the distortions of images of galaxies located farther from the observer than a large gravitational potential. The amount of distortion is proportional to the mass contained within the gravitational potential [6], which is referred to as the gravitational lens. This technique was used to build a gravitational profile for the collision in 1E 0657558. The *Chandra* X-ray observatory measures the X-ray emissions from the atomic de-excitations of colliding intergalactic particles. The results, shown in Figure 1.2, are striking. In this figure, the green contours show two clearly separated gravitational centers while the color profiles show the X-ray spectra from the intergalactic particles [5]. The gravitational centers have clearly decoupled from their respective intergalactic particles. A modification of Newtonian dynamics cannot explain this effect because the amount of mass required to create the observed gravitational profile is larger than the intergalactic particles, which represent the dominant source of luminous matter in the mass of clusters.

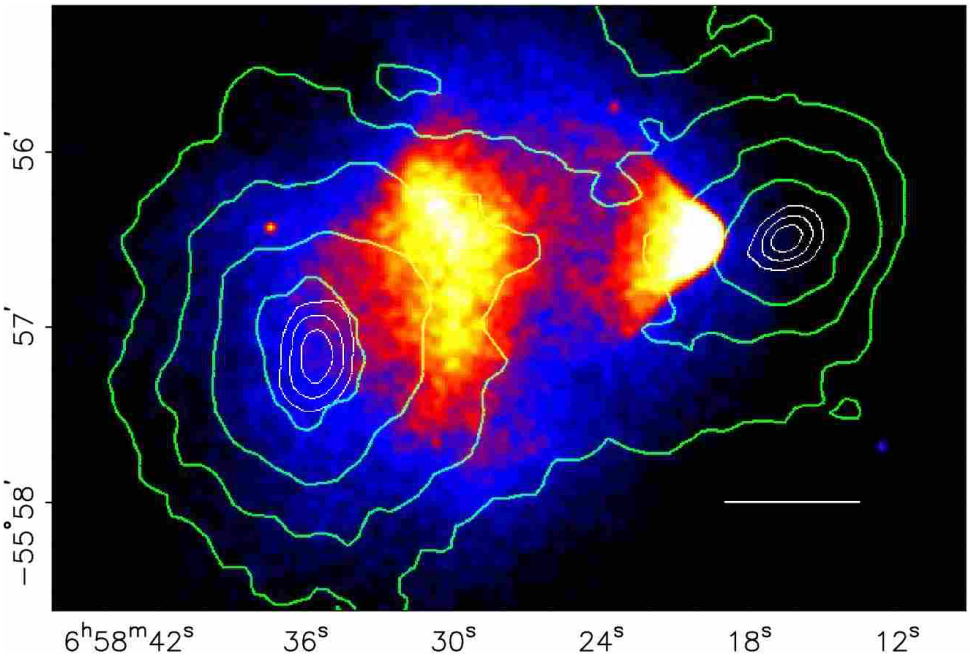

Figure 1.2. The gravitational potential and X-ray emission from colliding galaxy clusters 1E 0657558. The green contours, derived from weak lensing, show two clear gravitational potentials from this collision while the colors show the X-ray emission from the interaction of the intergalactic gas atoms. The intergalactic gases are the largest component of the baryonic mass contained within the clusters, and they are clearly decoupled from the gravitational centers. This necessitates the existence of some additional form of mass providing gravitational effects in the clusters. Figure from [5].

This leads to the conclusion that the gravitational potential and luminous, baryonic matter have been physically decoupled, necessitating the existence non-luminous matter consisting of something other than baryons, referred to hereafter as “non-baryonic”.

From the pioneering work of Zwicky to the highly advanced cosmological studies that are carried out today, the evidence continues to amass suggesting that non-luminous matter is prevalent in the galaxies and structure of the universe. This dark matter must exist as an explanation for the missing mass and the otherwise unexplained gravitational effects that are measured in galaxies and clusters of galaxies.

1.1.4 ΛCDM Model of the Universe

The Hot Big Bang model of the universe [7] postulates that the universe began as a singularity of energy, and the scale size proceeded to expand exponentially through the epoch of inflation. After this time, the universe continued to expand linearly with rate H, the Hubble

constant. The early universe was a plasma of ionized atoms and photons and electrons existing in thermal equilibrium. During the period before the epoch of recombination, electrons and photons interacted mainly by Thomson scattering,

$$\gamma + e^- \rightarrow \gamma + e^-, \tag{1.3}$$

which happened readily, causing the universe to be opaque. As the universe continued to expand the average temperature decreased and the photons became less energetic, causing the interaction rate Γ of the Thomson scattering to decreased. When Γ decreased below H, the photons were no longer in thermal equilibrium with the electrons, and the universe became transparent. These thermally decoupled photons, relics of the Big Bang, were first measured in 1965 as the Cosmic Microwave Background (CMB) radiation by Penzias and Wilson at Bell Labs [8].

Precision measurements of the CMB yielded interesting results [7]. First, in any given direction in the sky, the CMB energy spectrum is that of an ideal blackbody. Second, a dipole distribution emerged, indicating the universe is not perfectly homogenous today. In fact, the dipole indicates the solar system is moving at ~ 330 km/s with respect to the rest frame of the CMB. If the dipole effect is accounted for, a third property emerges. Small temperature fluctuations were discovered, indicating the non-homogeneity of the universe at the time of CMB decoupling. The mean temperature and fluctuations of the CMB are

$$\langle T \rangle = 2.725K \tag{1.4}$$

$$\langle \frac{\delta T}{T} \rangle = 1.1 \times 10^{-5} \tag{1.5}$$

Since the average CMB temperature varies by 30 μK, it is nearly isotropic.

The small anisotropies in the CMB, shown in Figure 1.3, provide additional information about the composition of the universe. These fluctuations indicate certain CMB photons have been additionally red or blue shifted from the mean temperature in (1.5). To explain these small deviations, consider a relic photon that exists in a gravitational potential well at the epoch of decoupling. That photon will lose energy upon climbing out of the well and gain an additional red shift. Conversely, a CMB photon at a gravitational potential "hill"

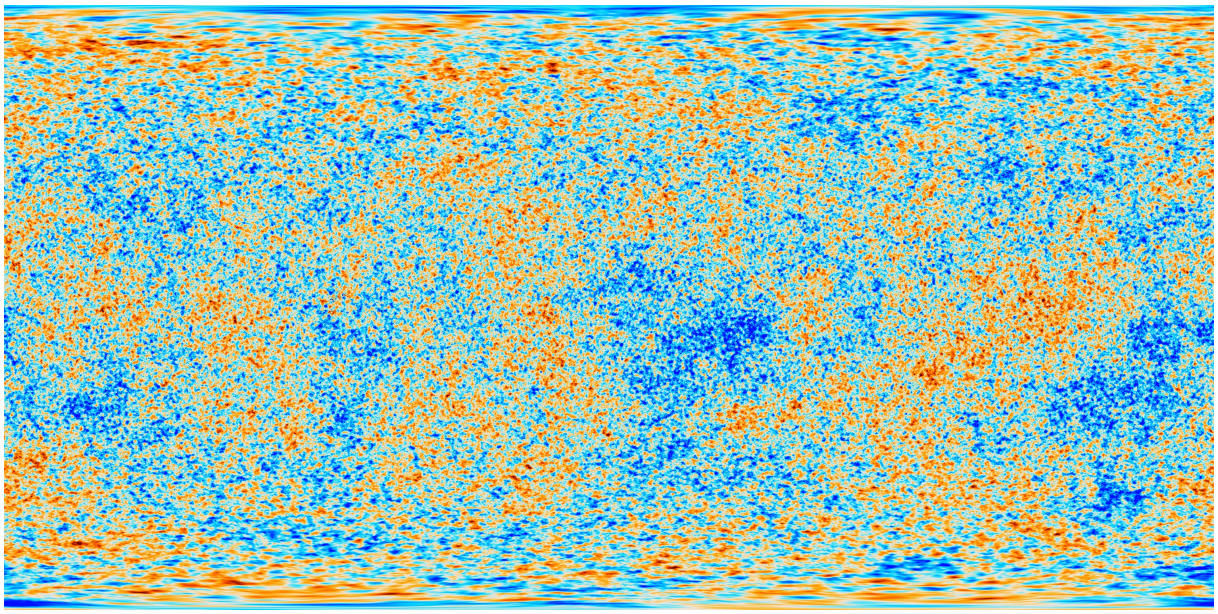

Figure 1.3. The Cosmic Microwave Background radiation after the background subtraction of the galactic plane and the solar system dipole. The average photon temperature is 2.725 K with fluctuations of 30 μK. The anisotropies indicate clumps of dark matter since CMB photons in those regions experience additional red or blue shifts resulting from gravitational interactions. The dark matter component of the universe is much larger than the baryonic component, so these clumps lead to large scale structure formation. Figure from [9].

will gain energy as it falls and gain an additional blue shift Since the gravitational potential is always negative, a potential “hill” means the potential has fluctuated above the average value. The small anisotropies observed in the CMB exist because the gravitational potential was not isotropic at the epoch of photon decoupling [7].

The ΛCDM model of the universe [10] where Λ is the cosmological constant and CDM stands for Cold Dark Matter, is currently considered the standard model of cosmology. It is derived from cosmological observations, and it includes six main parameters to fully describe the behavior of the universe. The parameters and descriptions are listed in Table 1.1. Based on cosmological measurements [9], it is known that baryonic matter accounts for ∼5% of the energy density of the universe, while dark matter is ∼23% of the energy density. Because dark matter is a much larger component of the energy density of the universe compared to the baryonic matter, the CMB anisotropies indicate that dark matter exists in "clumps." This produces local gravitational fields that attract the baryonic matter leading to

	Description	$Planck + WP + highL + BAO$
$\Omega_b h^2$	Baryon Density Today	0.02214 ± 0.00024
$\Omega_c h^2$	Dark Matter Density Today	0.1187 ± 0.0017
$100\theta_{MC}$	100 × approximation to r_*/D_A(CosmoMC)	1.04147 ± 0.00056
τ	Thomson optical depth - reionization	0.092 ± 0.013
n_s	Scalar spectrum power-law index	0.9608 ± 0.0054
Ω_Λ	Dark Energy Density Today	0.692 ± 0.010

Table 1.1. Select cosmological parameters for the ΛCDM model of the universe. Reproduced from [9].

the formation of large scale structure in the universe [7]. In fact, it has now been shown via large scale computer simulations that galaxy formation does not proceed as observed in the absence of dark matter [11].

1.2 Dark Matter Candidates

There is compelling evidence for the existence of dark matter on large scales in the universe. The nature and composition of the dark matter, however, is not well understood. In the ensuing sections, various candidates for dark matter are discussed.

1.2.1 Baryonic Dark Matter

The simplest explanation for the nature and composition of dark matter is to assume it is non-luminous baryonic matter. [6]. Big Bang Nucleosynthesis (BBN) is an important component of the standard cosmological model that deals with the formation of light baryons. This theory predicts the abundances of the light element isotopes of D, ^{3}He, ^{4}He, and ^{7}Li. This process occurs at temperatures of order 1 MeV, corresponding to the first few minutes immediately following the big bang. ^{4}He is primarily produced, comprising approximately 25% of the baryonic mass, followed by about 10^{-5} of D and ^{3}He and about 10^{-10} of ^{7}Li [12]. Comparison between prediction and measured abundances of these light isotopes constrains the baryonic component of the energy density of the universe to ∼2.3% [9]. As noted in Table 1.1, the dark matter density is larger than the BBN constraints on the amount of baryonic

matter, necessitating the existence of a non-baryonic form of dark matter.

1.2.2 Massive Compact Halo Objects

It is possible that a large amount of baryonic mass may reside in objects known as Massive Compact Halo Objects, or MACHOs [6]. MACHOs would be composed of normal baryonic matter, emit almost no radiation, and drift through interstellar space unassociated with a planetary system. Examples of MACHOs would be black holes, neutron stars, brown dwarfs, or unassociated planetary bodies. These objects are difficult to detect because they must be detected gravitationally. Weak lensing studies of stars in satellite galaxies such as the Large Magellanic Cloud are conducted to search for a gravitational effect from such objects. The surveys measured the fraction of the galactic halo mass from MACHOs to be no larger than 20%, making them an unlikely source of the dark matter in the universe. This fraction was expected to be 70%-80% [6].

1.2.3 Neutrinos

Another intriguing dark matter candidate is the neutrino [7]. Since it has been shown that the neutrino has a small, but non-zero, mass, it could account for the dark matter. A relic population of neutrinos, similar to the CMB, could have decoupled from the early universe and exist as a cosmic neutrino background. The number density of these relic neutrinos has been calculated to be

$$n_\nu = 3.36 \times 10^8 m^{-3}. \tag{1.6}$$

This corresponds to twenty million cosmic neutrinos passing through a human body at any moment. If neutrinos were to account for the dark matter in the universe they would each need to have a mass around 4 eV, which is unlikely given current measurements [9].

There are other astronomical issues with neutrinos as the dark matter in the universe. Cosmic neutrinos have a Fermi-Dirac distribution, so they have a maximum space density [13]. Certain types of galaxies, such as dwarf irregular galaxies, have very high dark matter densities. Given the maximum space density, neutrinos cannot be the dark matter in these types of galaxies [14, 15]. Further, neutrinos would have relativistic velocities, hence they would be considered hot (or, warm) dark matter. Because they are moving with such a

high velocity, they would smooth CMB fluctuations on smaller scales. Neutrinos as the dark matter could lead to the formation of superstructures like galaxy clusters, but it is difficult to model relativistic neutrinos leading to the formation of smaller structures such as individual galaxies. In fact, all types of hot dark matter would have similar problems [13]. This becomes less problematic if it is discovered that one type of neutrino is substantially more massive than the others, though this seems unlikely given mass difference measurements between flavor masses [7].

The discovery that neutrinos have non-zero mass implies the likely existence of additional SU(3)×SU(2)×U(1) singlet fermions, which can be very light, in which case they are referred to as sterile neutrinos. These additional particles can make up the dark matter. Because of the small Yukawa couplings, the keV sterile neutrinos are out of equilibrium at high temperatures, so they are not produced in the freeze-out from equilibrium [16], like other candidates are as discussed below. One possible method of production is from neutrino oscillations [17], whereby active neutrinos oscillate into sterile neutrinos which are not in thermal equilibrium. Constraints imposed by X-ray observations force the mass of a sterile neutrino to be as low as 1-3 keV [18]. If sterile neutrinos are generated via a different mechanism, the corresponding mass range can be relaxed by more than a factor of 3 [19].

1.2.4 Axions

Another proposed form of dark matter is the axion [6]. The combined action of charge conjugation (C), parity (P), and time reversal (T) is symmetric. CP, however, is not an exact symmetry, and certain weak interactions involving quarks violate CP, as has been experimentally demonstrated [20, 21]. Quantum Chromodynamics (QCD) predicts that strong interactions should have a much larger CP violation. This would lead to a non-zero electric dipole moment of the neutron, however, lack of experimental evidence has limited the CP-limiting parameter in QCD. If an additional global symmetry, $U(1)$, is introduced and spontaneously broken, the CP-violating phase becomes dynamical and allowed. The boson resulting from this symmetry breaking is the axion, a particle with a non-zero mass, which could account for the dark matter in the universe. The phenomenology of the axion is modeled by the scale of the symmetry breaking. The mass of the axion has been constrained

by laboratory searches, stellar cooling, and supernova dynamics to be very light, with mass $m_a < 0.01$ eV [22]. It couples so weakly with other matter that it was never in thermal equilibrium with early universe and hence, could be the cold dark matter observed today. There are several experiments underway actively searching for axions [23, 24], though the parameter space for the axion to be a viable dark matter candidate is getting smaller.

1.2.5 Weakly Interacting Massive Particle

An attractive candidate dark matter particle is the Weakly Interacting Massive Particle (WIMP) [6]. WIMPs are stable particles that arise from extensions of the standard model of electroweak interactions. The most common forms to be discussed are heavy fourth-generation Dirac and Majorana neutrinos, discussed above, and the neutralino and sneutrino that can arise in certain supersymmetric models. Typical WIMP masses are in the range 10 GeV to a few TeV, and they are proposed to interact with ordinary matter through some weak-like process. The remainder of this thesis discusses other WIMP properties and a direct search for WIMPs in the universe.

1.3 WIMPs

Imagine a particle created with the big bang that fell out of thermal equilibrium with the early universe similar to the decoupling of CMB photons discussed above. Such a particle could have a relic abundance in the universe today, and could be the cold dark matter in the universe. This hypothesized particle is referred to as the Weakly Interacting Massive Particle, or WIMP.

1.3.1 Unit Convention

Before discussing WIMPs in great detail, note the unit conventions that will be employed throughout this work. First, a "natural" unit scale will be assumed such that $\hbar = c = 1$. Therefore, mass will be reported in units of energy. The areas of detected pulses, described in subsequent chapters, will be in units of photoelectrons (phe). One unit of phe is equivalent to the area of the waveform generated as the response of the detector to a single detected photon. Pulse areas denoted with the subscript "c" indicated those pulses that have been corrected, and those denoted with the subscript "b" indicate pulse areas as measured by the

bottom PMT array only. Finally, pulse widths are denoted in units of samples. One sample is equivalent to 10 ns.

1.3.2 WIMP Miracle

If a new, stable particle existed, it could have a significant abundance today [7]. Similar to the formation of CMB photons, such a particle, χ, might have existed in thermal equilibrium and in high number in the early universe. As long as the temperature of the universe exceeds the mass of the χ particle, m_χ, the particle will continue to be in thermal equilibrium and the universe will be opaque to χ. The equilibrium abundance is maintained by annihilation of χ into standard model particles l, and the reverse interaction:

$$\chi\overline{\chi} \rightarrow l\bar{l} \tag{1.7}$$

$$l\bar{l} \rightarrow \chi\overline{\chi} \tag{1.8}$$

As the universe expands and cools, the process (1.8) becomes increasingly disfavored kinematically, and the density of χ decreases. When the universe expands to cool below m_χ, the remaining χ particles freeze out and form a relic cosmological abundance which exists as dark matter in the universe.

Now consider the details of the mechanism leading to this relic abundance. In thermal equilibrium, the number density n_χ^{eq} is proportional to the number of internal degrees of freedom of χ and is related to either the Fermi-Dirac or Bose-Einstein distribution, depending on the particle. At high temperatures, there are roughly as many χ particles as photons, but as temperature decreases, n_χ is Boltzmann suppressed by [25]

$$n_\chi \propto (m_\chi/T)^{3/2} e^{-m_\chi/T}. \tag{1.9}$$

If the expansion of the universe was slow enough to maintain constant thermal equilibrium, the WIMP density would still be Boltzmann suppressed and there would be no WIMPs. The universe is, however, not static.

When the temperature, $T \gg m_\chi$, χ has a high number density and (1.7) occurs rapidly. As T falls below m_χ, n_χ falls exponentially and the annihilation rate $\Gamma = \langle\sigma_a v\rangle n_\chi$ where

$\langle \sigma_a v \rangle$ is the thermally averaged total cross section times velocity, v, for self annihilation of χ into lighter particles. When Γ falls below H, the reaction from (1.8) ceases and a relic abundance of χ remains.

This can be modeled simply by the Boltzmann equation:

$$\frac{dn_\chi}{dt} + 3Hn_\chi = -\langle \sigma_a v \rangle \left[(n_\chi)^2 - (n_\chi^{eq})^2 \right]. \tag{1.10}$$

In this equation, H is the Hubble parameter, $(n_\chi)^2$ accounts for the depletion of WIMPs due to self annihilation, and $(n_\chi^{eq})^2$ accounts for the creation of WIMPs from lighter particles. In thermal equilibrium, the right side of the equation is zero and the number density of WIMPs is inversely proportional to the volume of the universe. A numerical solution of (1.10) yields the behavior observed in Figure 1.4. As time increases, the number density decreases exponentially, denoted by the solid curve, until the epoch of WIMP freeze out, leaving behind a relic density of WIMPs, denoted by the dotted lines. If such a particle exists, its present mass density is

$$\Omega_\chi h^2 \sim 3 \times 10^{-27} cm^3 s^{-1} / \langle \sigma_a v \rangle. \tag{1.11}$$

It is noteworthy that this result is independent of the WIMP mass and depends only on the self annihilation cross section. Now assume that this new particle has weak-scale interactions. In this case, the annihilation cross section is $\langle \sigma_a v \rangle \sim 10^{-25}$ cm^{3}s^{-1}. By simply assuming that dark matter interacts at the weak scale , the correct order of magnitude for dark matter abundance from ΛCDM is predicted. This remarkable coincidence is known as the "WIMP miracle" [26].

1.3.3 Standard Halo Model

The detection signature of WIMPs will depend on the density of dark matter in the Milky Way, specifically in the neighborhood of the Earth. Therefore, it is important to have some understanding of, and develop a basic model for, how WIMPs might be distributed locally. The simplest assumption is to assume the Copernican principle that the Milky Way galaxy is similar to other spiral galaxies, which can be studied from the outside. Since cold dark matter should clump where galaxies exist, it is reasonable to assume there is a clump sur-

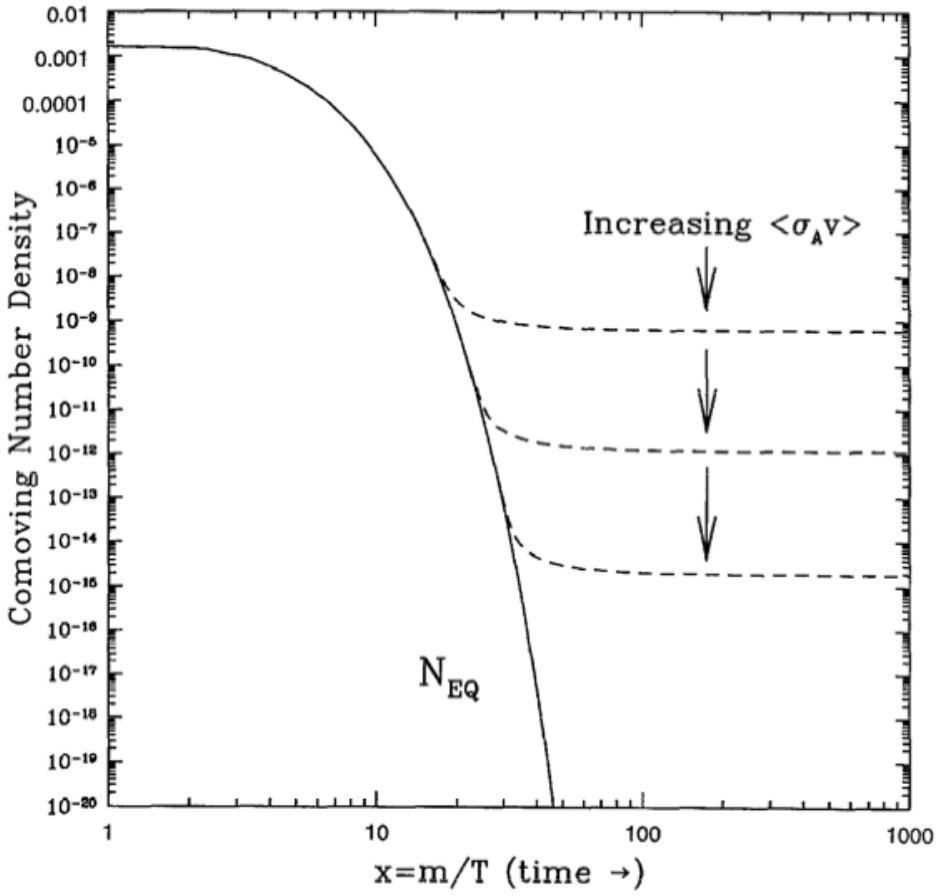

Figure 1.4. The number density of WIMPs plotted against time. As the universe expands and cools, WIMPs remain in thermal equilibrium and the abundance is Boltzmann suppressed. When the expansion rate of the universe drops below the annihilation rate of the WIMPs, a relic abundance freezes out and remains as the dark matter, similar to the decoupling and freeze out of photons leading to the formation of the CMB. Figure from [26]

Parameter	Description	Value
ρ_χ	local WIMP density	0.3 GeV/cm^3
v_o	circular velocity of the sun in galactic frame	220 km/s
v_{esc}	galaxy escape velocity	544 km/s
v_{earth}	earth velocity	245 km/s
v_{WIMP}	mean WIMP velocity	232 km/s

Table 1.2. The Standard Halo Model is the simplest model of the dark matter distribution. It assumes an isotropic, isothermal sphere of dark matter. Some important parameters of the model are listed.

rounding the local galaxy. A typical spiral galaxy is theorized to be immersed in a spherical dark halo, so it is natural to assume the same of the distribution within the Milky Way [26].

The simplest model of the local dark matter distribution is called the standard halo model (SHM) which assumes an isotropic, isothermal sphere of dark matter that envelopes the galaxy. A commonly used model has been developed by Navarro, Frenk and White [27], which incorporates a Maxwell-Boltzmann WIMP velocity distribution in the galactic frame, truncated at the galaxy escape velocity v_{esc}. Other important parameters of the SHM, such as WIMP density ρ_o, are summarized in Table 1.2 [28]. The remainder of this work assumes the SHM.

This assumption will present a bias on the results because changing the model parameters will change the expected WIMP interaction rate. However, these parameters must vary by a factor of $\sim$10 for the effect to be larger than 10%.

1.3.4 Detection of WIMPs

If WIMPs exist, they should be detectable on the earth by searching using one of three methods. First, direct detection of dark matter requires dark matter to scatter elastically off a target, depositing energy and producing a detectable signal. WIMP scattering off nuclei and the detection of axions through the interaction with photons in a magnetic field provide two such examples. Second, indirect detection of dark matter involves searching for the high energy particles produced when two WIMPs annihilate. Several experiments, for example,

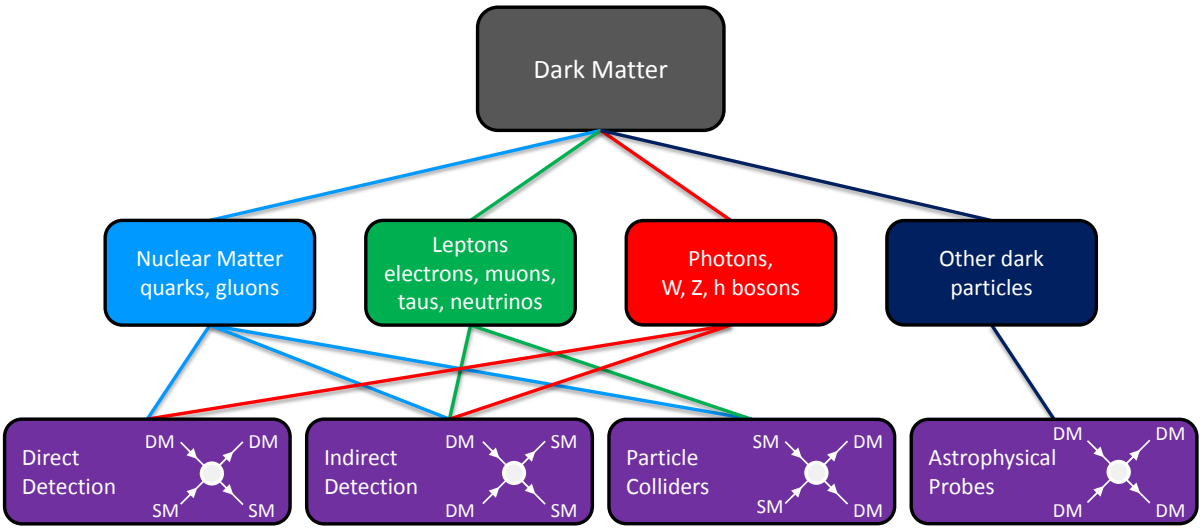

Figure 1.5. Dark matter may have interactions with one or more of four categories of particles: 1.) Nuclear matter detectable; 2.) Leptons; 3.) Photons and other bosons; and 4) Astrophysical probes. These interactions can be detected directly, indirectly, at particle colliders, or some combination of three. Astrophysical probes are generally studies of the gravitational effects of missing mass. Figure from [29]

are searching for high energy gamma rays originating from the galactic center as the highest concentration of WIMPs should exist there. Another example of indirect dark matter detection is observing the gravitational effects caused by WIMPs on the surrounding astronomical bodies. Lensing effects used to determine dark matter densities are indirect measurements. Finally, particle accelerators such as the Large Hadron Collider (LHC) can collide two standard model particles and create two WIMPs which would be detected as missing energy with a different signature than neutrino missing energy. These search strategies are shown in Figure 1.5 [29].

Because the nature of dark matter is complex, multiple methods and searches are used. To date, no conclusive evidence of WIMP interaction has been observed, so a limit on WIMP cross section plotted versus WIMP mass is the normal figure of merit to describe sensitivity and rule out parameter space. An example, discussed in detail below, is shown in Figure 1.6 A subset of these search methods will be described.

1.3.4.1 Indirect Dark Matter Searches

Indirect dark matter searches do not aim to detect dark matter particles themselves. Instead, they search for the standard model particles that are produced in the annihilation of two WIMPs. Signals include photons, neutrinos, or positrons. The Alpha Magnetic Spectrometer (AMS) experiment [30] is an example of an indirect dark matter search experiment. It is located on the International Space Station. It is searching for evidence of e^+/e^- pairs resulting from WIMP annihilation in the center of the galaxy using a magnet spectrometer. IceCube [31] is an example of a terrestrial indirect WIMP search. It is a large Cherenkov detector searching for neutrinos that could come from WIMP scatters. This type of search is becoming relevant in sensitivity. For example, the Fermi Gamma-Ray Space Telescope observations of Milky Way satellite galaxies have excluded some thermal WIMP models [29].

1.3.4.2 Particle Colliders

Collider experiments can search for dark matter production in the form of missing energy following a collision. At the LHC, protons (quarks and gluons) collide at high energies, and many different particles are produced with various rates. Missing energy coupled with the correct combination of output particles could be an indication of WIMP pair production. For example, both ATLAS and CMS at the LHC searched for events containing one photon and large missing energy [32]. Collider searches can readily create lighter particles, so they are poised to search for light WIMPs while the direct and indirect searches are more sensitive to higher mass WIMPs. Also, collider searches are less susceptible to the spin-independent and spin-dependent challenges that plague direct dark-matter searches, as evident in Figure 1.6. The left pane shows the spin-independent cross-section limits as a function of WIMP mass. The current best direct searches (brown, pink) are compared with the collider mono-photon search. The right pane shows the spin-dependent cross-section limits. Direct searches are shown in pink, cyan, and black. Note that in both cases, the collider searches have higher sensitivities at lower masses. This is due to the fact that colliders can readily produce light particles while direct searches are limited by the detector thresholds. In the spin-dependent case the collider searches are more sensitive than the direct searches [32].

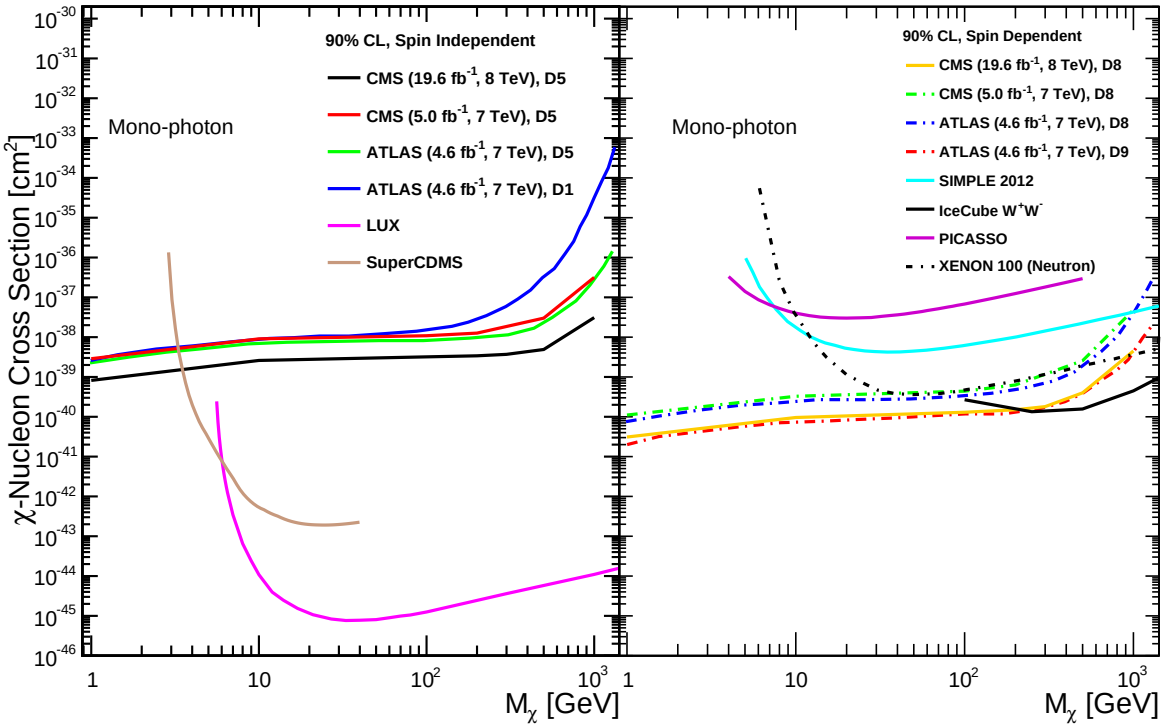

Figure 1.6. The current best limits on cross-section and WIMP mass given no conclusive evidence of WIMP detection from mono-photon collider measurements and direct dark-matter searches. The left pane shows the spin dependent limits. SuperCDMS and LUX are currently the most sensitive spin-independent direct dark matter searches. Those searches lose sensitivity at low WIMP mass due to threshold effects. Collider searches are most sensitive at low WIMP mass because of the machine's readiness to produce low mass particles. The right pane shows the spin-dependent limits. Direct dark matter searches PICASSO, IceCube, and Xenon100 are less sensitive than the mono-photon collider search. A direct search has limited sensitivity to spin-dependent interactions because all that matters is the net spin of the nucleus, not the overall number of nucleons. For example, all major isotopes of Argon have even number of protons and neutrons, so no net spin for either, thus direct searches employing Argon have no sensitivity to spin-dependent WIMP interations. Figure from [32]

1.3.4.3 Direct Dark Matter Searches

Direct searches for dark matter involve the elastic scattering of WIMPs off a target nucleus. The detectors all behave in a similar fashion in that they detect nearly any particle that interacts regardless of the particle type. Thus, they are highly sensitive to backgrounds, so care must be made for background minimization. Since a WIMP is expected to have net charge of zero, neutron interactions in a direct dark matter search will be identical to a WIMP interaction. Charged particle interactions tend to have a different signature, so discrimination between charged background signals (electron recoils, or ER) and neutral WIMP interactions (nuclear recoils, or NR) is possible.

Several experimental techniques are used to detect WIMPs directly, and a subset will be discussed here. The first subset are cryogenic detectors [33]. These detectors contain semi-conductors such as Germanium or Silicon cooled to sub-kelvin temperatures. Both germanium and silicon have isotopes that are sensitive to spin-dependent interactions, though the spin expectation values are quite low, making these detectors better suited for measuring spin-independent interactions. When a WIMP interacts with the target, it deposits a small amount of energy in the form of heat. A superconductor held at a temperature near its transition temperature absorbs this heat and goes normal. During the initial energy deposition, cooper-pairs in the target are freed and swept by an electric field to a charge collector. ER events have different heat-to-charge ratios than do NR events, allowing for the discrimination between WIMPs and charged backgrounds. One advantage of this type of detector is that they have a very low detection threshold to NR interactions, thus giving them a higher sensitivity to low mass WIMPs. SuperCDMS is one such example of this type of detector. In terms of direct dark matter searches, SuperCDMS currently has the highest sensitivity to low mass WIMPs for spin-independent interactions [34], shown in brown in the left pane of Figure 1.6.

Next, consider dual-phase liquid/gas noble-element detectors. Example targets include argon and xenon. Argon has no sensitivity to spin-dependent interactions and xenon has limited sensitivity, so these detectors are also best suited to measure spin-independent interactions. A dual-phase xenon detector is the basis for the work presented here, so detailed

discussions of this type of detector are in the following chapters. A brief introduction is presented here. When a particle scatters off the target, in the liquid phase, it excites atomic electrons, moving them to higher orbital levels. The subsequent de-excitation results in a prompt scintillation signal. The energy deposition also produces ionization electrons which are drifted in an electric field and collected. The charge-to-light ratio is different between ER and NR events, allowing for discrimination between WIMPs and backgrounds [33]. This type of detector is more sensitive to higher WIMP masses. The Large Underground Xenon (LUX) detector is currently the most sensitive dual-phase noble-element detector [35], employing xenon as its target. In the left pane of Figure 1.6, the LUX 2013 result is shown in magenta. It is more sensitive that SuperCDMS and the collider searches at WIMP masses above $\sim$6 GeV.

Finally, consider threshold detectors. In this type of detector, a superheated liquid is used as the target. By carefully tuning the temperature and pressure, it can be made insensitive to charged particle energy depositions, a very powerful background rejection technique. A dense energy deposition, like that from an NR interaction, will provide the necessary energy for nucleation, creating a bubble. Acoustic sensors detect these bubbles to provide the incident particle information. A drawback to this type of detector is its sensitivity to alpha interactions which form a problematic background. Acoustic differences between neutral interactions and alpha interactions provide rejection. By careful choice of the target fluid, this type of detector can be well-suited to measure spin-dependent WIMP interactions [36]. PICASSO is one example of a threshold detector [37]. It is poised as a sensitive direct search for spin-dependent WIMP interactions, shown in Figure 1.6, right pane, magenta. As these detectors become larger, the sensitivity will increase to be more competitive with collider searches.

As noted, Figure 1.6 shows the collider search results alongside the best limits from direct detection searches for both spin-independent and spin-dependent interactions. Of course this is not the complete picture. Certain experiments ([38–42]) have claimed discovery, though the observed signal has yet to be corroborated by a different detector technology.

1.3.5 WIMP Elastic Scattering

Now, consider the direct detection method of searching for WIMPs. The following is a description of the calculation of the expected WIMP scattering rate in a detector. Assuming the SHM, a charge-neutral WIMP can scatter elastically off a target nucleus. As indicated in Table 1.2, WIMPs are non-relativistic and hence, the expected kinetic energy of a nuclear recoil from a WIMP-nucleus interaction is not expected to exceed ∼100 keV. The measured WIMP-nucleus interaction rate in such a detector will therefore depend highly on the energy threshold for detection [43].

In the simplest case where the detector is stationary in the galaxy, the differential scattering rate, in units of (counts/kg/keV/day), is nominally expected to be smoothly decreasing with the form [44]

$$\frac{dR}{dE_R} = \frac{R_o}{E_o r} e^{-E_R/E_o r} \tag{1.12}$$

where E_R is the recoil energy, E_o is the incident kinetic energy of a WIMP with mass M_χ, r is a kinematic factor $r = 4M_\chi M_T/(M_\chi + M_T)^2$ for target nucleus of mass M_T, R is the event rate per unit mass, and R_o is the total event rate. An experiment measures the differential rate, or left side of (1.12), and the relation allows for a corresponding limit placed on R_o, for each assumed M_χ. A limit on R_o can be converted to a limit on cross section by assuming the SHM.

Of course, in reality it is not that simple. The right hand side of (1.12) is not perfectly featureless but instead depends on several factors. The detector is not stationary in the galaxy but is actually located on the earth, orbiting around the sun, moving with the solar system through the galaxy. The detection efficiency of nuclear recoils is different from that of the background electron recoils, resulting in a relative efficiency factor. The target may consist of more than one element or isotope. The resulting sensitivity will be different for spin-dependent (axial) and spin-independent (scalar/vector) interactions. Spin-independent interactions occur when the WIMP scatters coherently off the nucleus, and the scattering rate $\propto A^2$. For spin-dependent interactions, the scattering amplitude changes sign with spin direction so that, although the interaction with a nucleus is coherent, when the nucleon scattering amplitudes are summed, paired nucleons effectively cancel each other out. Only

residual nucleons contribute, so a target with an odd number of protons or neutrons is required to detect axial interactions. And finally, there will be nuclear form-factor corrections due to the finite size of the nucleus. All of these factors have been treated in great detail in [44].

In the calculations that follow, the formalism presented in [28] is followed. Because spin-dependent interactions are out of the scope of this work, concentration will be placed on coherent spin-independent interactions. Taking into account the corrections listed above, (1.12) can be recast as

$$\frac{dR}{dE_R} = N_T \frac{\rho_\chi}{M_\chi} \int_{v_{min}}^{\infty} v f(v) \frac{d\sigma}{dE_R} d^3v \tag{1.13}$$

where $f(v)$ is the local dark-matter velocity distribution in the detector rest frame, v_{min} is the minimum speed the WIMP must have for a nucleus to recoil with energy E_R, and the differential cross section $d\sigma/dE_R$ is

$$\frac{d\sigma}{dE_R} = \frac{1}{2v^2} \frac{M_N \sigma_n}{\mu_{ne}^2} \frac{(f_p Z + f_n (A-Z))^2}{f_n^2} F^2(E_R) \tag{1.14}$$

In (1.14), σ_n is the WIMP-nucleon interaction cross section, μ_{ne} is the WIMP-nucleon reduced mass, and f_n and f_p parameterize the dark matter couplings to neutrons and protons, respectively. For simplicity, assume $f_n = f_p$, though in specific models this may not be the case.

The nuclear form factor, $F(E_R)$, is modeled as the Helm form factor from [44]:

$$F^2(E_R) = \left(\frac{3[sin(qR) - qRcos(qR)]}{(qR)^3} \right)^2 e^{-q^2 s^2} \tag{1.15}$$

where $q = \sqrt{2 M_N E_R}$, $R = \sqrt{c^2 + \frac{7}{3}\pi^2 a^2 - 5s^2}$, $c = 1.23A^{1/3} - 0.60$ fm, $s = 0.9$ fm, and $a = 0.52$ fm. This model agrees to within a few per cent with more complex parameterizations available. The dark matter velocity distribution is parameterized as

$$f(v) = \frac{1}{N}(e^{-v^2/v_o^2} - e^{-v_{esc}^2/v_o^2});\ v < v_{esc} \tag{1.16}$$

where N is a normalization constant and v_o is the circular speed of the sun about the center of the galaxy. When $v > v_{esc}$, $f(v) = 0$. Combining all of these factors together, and assuming

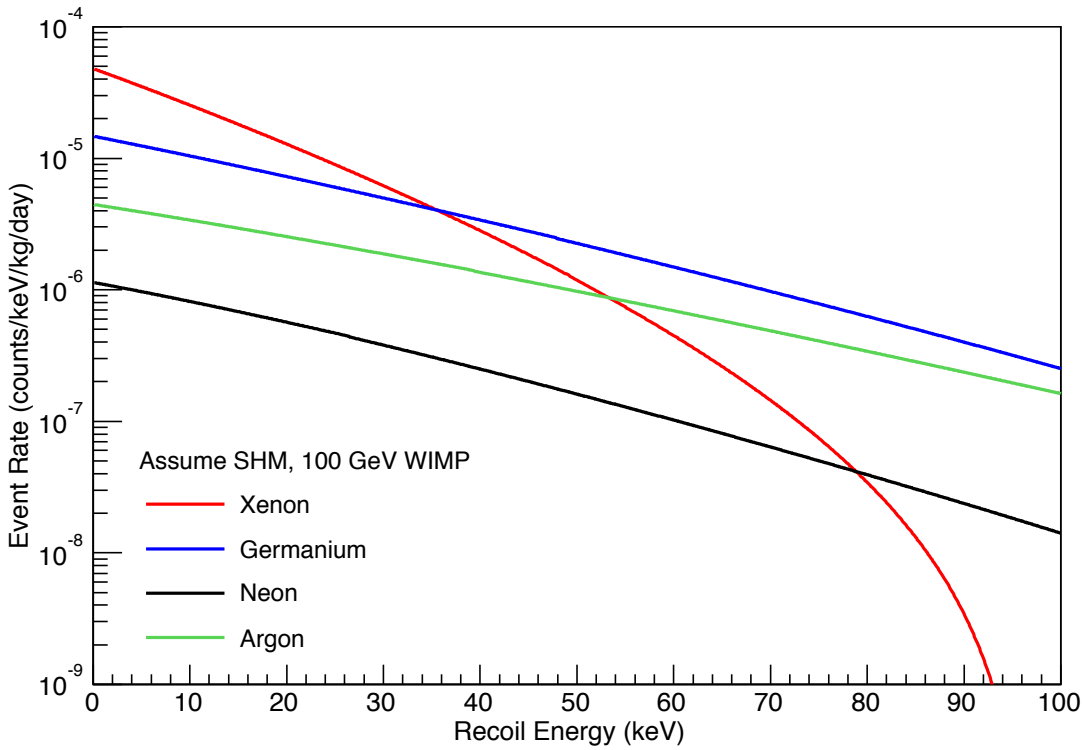

Figure 1.7. The differential event rate of WIMP elastic scattering off various nuclei, assuming spin-independent interactions. To calculate these rates, the following assumptions are made: the SHM (Table 1.2) parameter values, $M_\chi = 100$ GeV, and $\sigma_n = 10^{-45}$ cm^2. At the lowest recoil energies, xenon is the most sensitive target, but its sensitivity falls off due to form factor considerations.

the SHM, the differential scattering rate for various target materials can be compared, shown in Figure 1.7. These interaction rates, expressed in counts/kg/keV/day, are quite low. For example, assuming $M_\chi = 100$ GeV, and $\sigma_n = 10^{-45}$ cm^2, a 100 kg xenon detector would expect to observe about 1 event in an entire year. This information clearly shows the large effect the spin-independent coherence term has on the expected rate: xenon has the largest nucleus so it is the most sensitive. The decline in rate is more dramatic in xenon than the other targets due to suppressions from the nuclear form factor. The expected rate, highly dependent on the model, is used to understand the mass and cross section of the incident WIMP to quantify its properties.

Chapter 2

The Large Underground Xenon Detector

The Large Underground Xenon (LUX) detector is used in a direct search for cold dark matter. It operates as a fixed target of liquid xenon at a depth of nearly a mile underground at the Sanford Underground Research Facility in South Dakota. In late 2012, the LUX detector commenced operations, making it the world's most sensitive direct dark matter search experiment.

LUX is a dual-phase noble-element time projection chamber using xenon as the target. Similar types of detectors make use of other noble elements in place of xenon, but they all work based on the same principles. In this chapter, the principles governing the operation of a noble element detector will be discussed. The choice of xenon as a detector medium instead of other noble-elements will be motivated. Finally, the LUX detector will be described in detail.

2.1 Noble-Gas Detectors

A time projection chamber (TPC) employing a noble gas as a detection medium operates following a basic principle in dual phase operation, and these types of detectors have been in operation since the 1960s [45–48]. The pressure and temperature are carefully controlled such that the bulk of the medium is in the liquid phase while a small gas region is maintained. A particle enters the liquid region (referred to as the target) and scatters elastically off either a nucleus or an electron. This causes an energy deposition as the target particle recoils, producing scintillation light and ionization electrons. A uniform electric field surrounding

the target region causes the ionization electrons to drift through the liquid region toward the interface between the liquid phase and gas phase. Upon their arrival, another, typically higher, electric field is employed to extract the drifted electrons from the liquid into the gas region where they are accelerated, producing electroluminescence light. The set of signals produced by prompt scintillation and delayed charge collection provides information about the nature and amount of the original energy deposition.

Additionally, because the ionization electrons drift at a constant speed, the length of the drift time from the interaction site to the gas region allows for the calculation of the drift distance. This, together with the information obtained about the location of the collected charge in the XY plane allows for full three dimensional position reconstruction of events. With this information, a central, fiducial volume can be considered within the target to reduce the background signals which occur near the edges of the detector.

2.1.1 The Choice of Xenon

A dual-phase noble gas TPC is a very useful technology for use in the search for WIMP dark matter. Several detectors utilizing the argon, xenon, and neon are in operation or under development [36, 49]. These detectors share several common features that make them ideal for rare-event searches. Because drifting ionization electrons quickly reach terminal velocity, the length of the drift indicates the depth of the event within the liquid volume. This information, coupled with the XY location of the collected charge allows for three dimensional position reconstruction. The scalability is straight forward: in principle, to have a more sensitive detector all that is needed is a larger container of the target. For these reasons, this type of detector is an attractive one to build.

There are, of course, many reasons to choose one type of target over another. For example, in the scintillation process described in detail in the following sections, Argon detectors allow for better discrimination between charged and neutral interactions leading to better background rejection based on a greater separation in the singlet and triplet decay channels [43]. Argon is also less expensive to procure; however, argon extracted from the atmosphere contains the ^{39}Ar isotope, which is radioactive with a half-life of 269 years [50]. Given its trace isotopic abundance, this results in an activity of $\sim$1 Bq/kg, emitting 565 keV naked

betas and presenting an internal background to a potential argon detector. To mitigate this, argon could instead be mined from the earth (where most of the ^{39}Ar has decayed), but this nullifies the cost savings of choosing argon.

Xenon, in contrast, has benefits that far outweigh its drawbacks, making it a better choice as a detector medium. Since a WIMP signal is a nuclear recoil with deposited energy in the few keV range, detection can depend dramatically on the detector threshold. As shown in Figure 1.7, xenon is the most sensitive material to the lowest energy recoils. This is due to xenon having a larger nucleus than the other noble gasses, thus a higher spin-independent coherence term. Xenon has no long-lived radioactive isotopes, so there is no xenon internal background to overcome. It has a high Z and high density which gives rise to excellent shielding against external gamma-rays. This allows for the design of smaller detectors with competitive effective target masses, with very low background rates. Finally, xenon has isotopes with odd numbers of neutrons, giving it some sensitivity to spin-dependent interactions [43]. Further, as for all noble elements, xenon does not absorb its own scintillation light, thus enabling the construction of large transparent detectors. It also has very low electronegativity, which makes it feasible to drift electrons over large distances, provided that other impurities are minimized. Finally, because of its inert nature, it allows for the deployment of chemical bettering techniques for purification. For these reasons, LUX utilizes xenon as a target, and xenon will be the focus of this work moving forward.

2.1.2 Xenon Energy Partitioning

A xenon detector is sensitive to any particle that enters its target volume whether the incident particle is charged or uncharged. An interaction involving an electron or gamma happens via the coulomb force, and was earlier defined as an electron recoil (ER). A neutral particle interaction, such as that from a neutron or WIMP, occurs via elastic scattering off the nucleus, defined earlier as a nuclear recoil (NR). ER interactions have different signatures than NR interactions allowing for the separation of signal (NR) from background (ER). Figure 2.1 shows the process of energy deposition in xenon, which can occur via one of three channels discussed below.

First, some energy will be lost to “heat” in the form of kinetic energy imparted to sec-

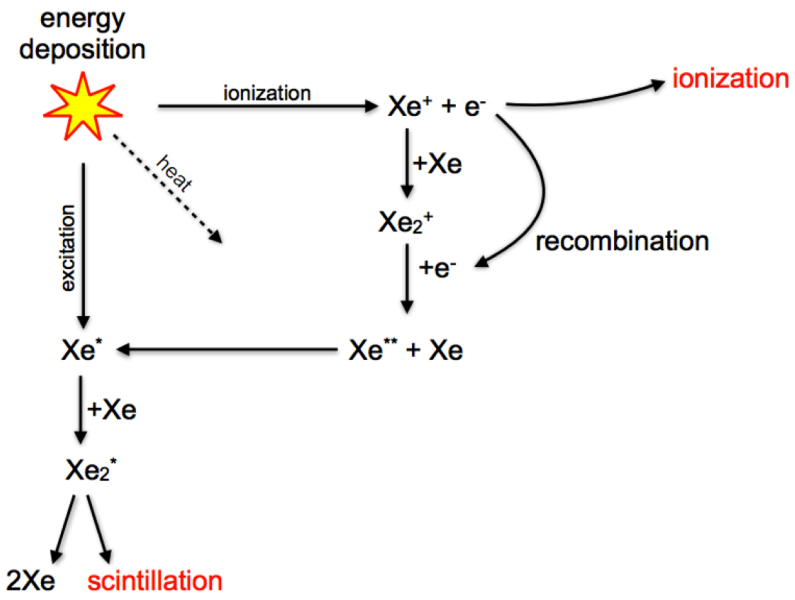

Figure 2.1. The response of xenon to an energy deposition. An incident particle can transfer energy as undetectable heat, directly excite xenon leading to scintillation light, or ionize the xenon, producing free electrons. Those free electrons can either combine with the xenon ions and add to the initial scintillation or escape the interaction site and drift in an electric field to a charge collector.

ondary nuclear recoils or sub-excitation electrons [51, 52], both of which do not produce any detectable signal. Due to a difference in track length, for the same recoil energy, the amount of energy loss from heat differs between ER and NR interactions. This leads to the definition of two energy scales, keV$_{ee}$ and keV$_{nr}$ used to describe the observed energy from ER and NR events, respectively. Because these energy scales refer to the observed energy, an ER and NR event of the same incident energy will be observed to have different amounts of deposited energies. Thus careful calibrations are necessary.

Second, consider the excitation path. When an incident particle causes a recoil, it causes some amount of direct excitation of atomic xenon, Xe*. This Xe* combines with a ground state atom Xe to form an excited dimer Xe$_2^*$. The excited dimer is what de-excites and produces two 7 eV (177 nm) photons as scintillation light. Because an excited dimer produces the scintillation, the liquid xenon atoms are practically transparent to the photons produced by the molecular component. These photons will propagate far enough for detection [52].

Finally, the initial energy deposition can ionize the xenon, producing free electrons.

These electrons have some probability to recombine with the positively charged xenon ions that are created. Following the chain in Figure 2.1, recombination will lead to additional scintillation light produced at the interaction site [52]. Light produced at the interaction site by direct excitation or by excitation following the recombination of an ionization electron is referred to as the primary scintillation, or S1 signal. The scintillation yield from this process depends on the presence of an electric field, and its strength.

The ionization electrons that are liberated in the initial recoil have some probability to escape, even when no electric field is present. In order to collect and measure them, a xenon TPC has an electric field applied across the target volume. The applied electric field liberates ionization electrons from the interaction site and drifts them to a charge collector. As one might expect, the recombination probability decreases as the drift electric field increases.

Mathematically, the partitioning of energy is modeled with a Platzman equation [52] as

$$E_{dep} = N_{ex} W_{ex} L^{-1} + N_i W_i L^{-1} \tag{2.1}$$

$$= N_i L^{-1} (\alpha W_{ex} + W_i) \tag{2.2}$$

$$\alpha \equiv N_{ex}/N_i. \tag{2.3}$$

In (2.1), E_{dep} is the amount of energy deposited in a single interaction, N_{ex} is the number of excitons created, N_i the corresponding number of ions, L is the Lindhard factor and W_{ex} (W_i) the work function, or energy required, for the creation of of excitons (ions). The ratio of excitons to ions, α, has a theoretical value of 0.06 for liquid xenon [53, 54]. From (2.1), the number of excitons and ions can be calculated, and from that the actual number of photons and electrons can also be calculated

$$N_i = \frac{E_{dep} L}{\alpha W_{ex} + W_i} \tag{2.4}$$

$$N_{ex} = \alpha N_i \tag{2.5}$$

$$N_\gamma = N_{ex} + r N_i \tag{2.6}$$

$$N_e = N_i (1 - r) \tag{2.7}$$

where r is the same recombination probability mentioned above [55]. Because NR events deposit smaller amounts of detectable energy, the resulting recoiling xenon atoms tend to have shorter tracks than those produced by ER interactions. Thus, the recombination probability for ER and NR events will be different, leading to a difference in the charge-to-light ratio between ER and NR interactions. This allows for discrimination between backgrounds (ER) and signals (NR).

Because NR events, as discussed above, involve interactions between heavy, uncharged particles, they tend to have very short tracks in the target. Because of this, NR events tend to deposit the majority of their energy in the "heat" channel, thus rendering this energy undetectable to a dual phased xenon detector. The Lindhard factor, L, is a measure of the amount of energy lost to heat, in an attempt to reconcile NR energy depositions with the ER ones. A larger value of L corresponds to a smaller amount of energy deposited as heat. For ER events, tracks in the target tend to be longer and L is assumed to be 1. For NR events in this type of detector, and in the recoil energy scales of interest, L ranges between 0.1 and 0.2. As defined above, this leads to the energy scales keV$_{ee}$ and keV$_{nr}$ for ER and NR respectively [55]. Lindhard theory is more appropriate to solid crystal scintillators, and in order for it to apply to xenon the Hitachi correction is employed [51].

Instead of using the Lindhard factor, many experiments use instead the "effective Lindhard Factor," L_{eff}, also known as the relative scintillation efficiency, defined as the ratio of zero-field light yields of ER and NR events as

$$L_{eff} = \frac{N_{\gamma nr}}{N_{\gamma er}} \frac{E_{er}}{E_{nr}}. \tag{2.8}$$

In this relation, the "er" subscript indicates a reference ER, typically chosen to be a 122 keV gamma. If, for example, the recombination were complete at zero field, one would see $L = L_{eff}$, but neither ER nor NR events undergo complete recombination at zero field [56].

An event schematic in a dual-phase xenon detector is shown in Figure 2.2. All of the features are apparent: an initial energy deposition leads to primary scintillation (S1) and ionization. The ionization electrons either recombine and add to the S1 signal, or escape the interaction site and drift to a charge collector. In this schematic, the collected charge leads to an electroluminescence signal (S2), also detected as photons. The charge-to-light

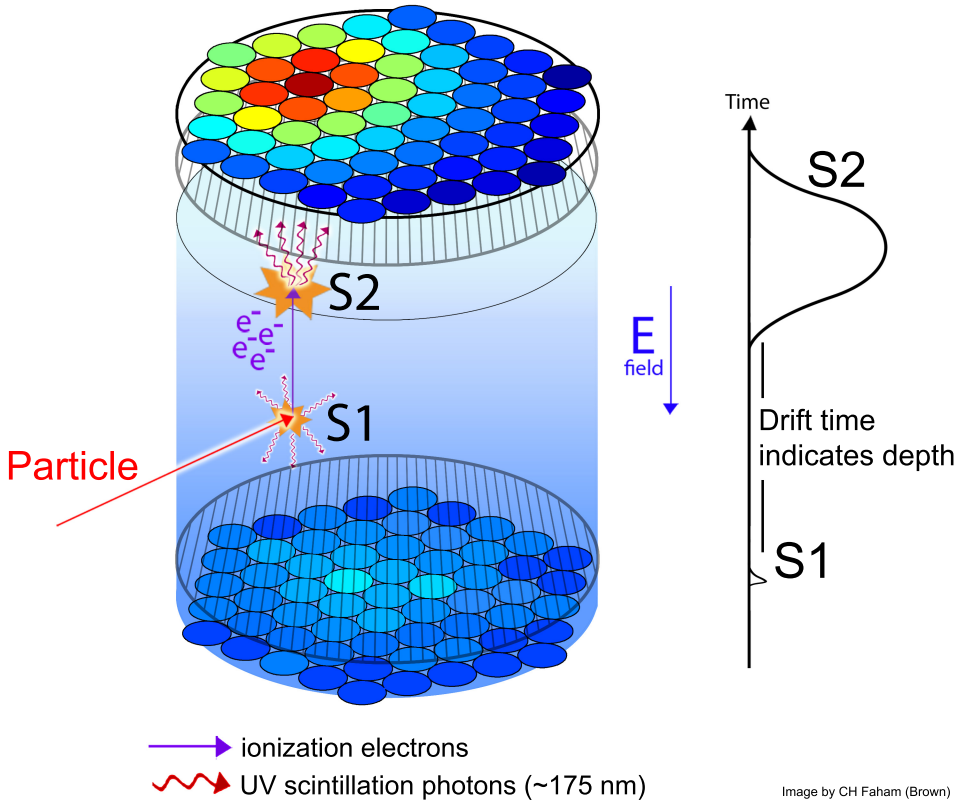

Figure 2.2. An event schematic in a dual phase xenon detector. An incident particle enters the target volume, in this case liquid xenon, and deposits energy. This causes direct excitation and ionization of atomic xenon. The ionization electrons can recombine at the interaction site and excite additional atoms. These collective excimers leads to the S1, or primary scintillation, signal. The ionization electrons that do not recombine will drift in an electric field to the gas region where they are extracted and accelerated, producing an S2 or electroluminescence signal.

ratio depends on the incident particle type and energy. Further properties of S1 and S2 signals are discussed in the following sections.

2.1.3 Primary Scintillation

The primary scintillation signal in xenon is generated via two processes. When an incoming particle enters the target medium, it deposits energy through either direct atomic excitation, leading to the creation of a dimer in the excited state, or ionization, which produces free electrons. The free electrons can either escape the interaction site or recombine within a characteristic timescale $\mathcal{O}(10$ ns), producing excited dimers, similar to those created by

Singlet lifetime	3.1 ± 0.7 ns
Triplet lifetime	24 ± 1 ns
Recombination Time	$\mathcal{O}(10)$ ns
Singlet/Triplet - ER from direct excitation (γ induced)	0.17 ± 0.05
Singlet/Triplet - ER from recombination (γ induced)	0.8 ± 0.2
Singlet/Triplet - ER from both processes (α induced)	2.3 ± 0.51
Singlet/Triplet - NR (neutron induced)	7.8 ± 1.5

Table 2.1. Parameters that affect the shape of the S1 pulse in liquid xenon detectors. The lifetimes for the singlet and triplet dimer states are listed. The ratios of the number of excitations in the singlet state to those in the triplet state are also listed for various cases. ER events corresponding to direct excitation or recombination have different ratios for γ induced recoils. ER ratios for α interactions and NR ratios are single valued.

direct excitation. These excited dimers exist in either a triplet state or singlet state. The de-excitation of all dimers produces the total primary scintillation signal, known as S1 [57], and it can be characterized by three fundamental time constants: the singlet lifetime, the triplet lifetime, and the recombination time, as well as the ratio of singlet states to triplet states. These properties for liquid xenon are summarized in Table 2.1. The ratio of the number of singlet states to triplet states is different for direct excitation and recombination processes for electron recoils based on experimental data [57] The de-excitation lifetime of the dimer depends on whether it is in the singlet or the triplet state, given by the decays ${}^1\Sigma^+_{excited} \rightarrow {}^1\Sigma^+_{ground}$ and ${}^3\Sigma^+_{excited} \rightarrow {}^1\Sigma^+_{ground}$. The ratio of the number of excitations in the singlet state to those in the triplet state is dependent on the target medium, recoil type, electric field, and dE/dx. The S1 pulse is also determined by the recombination time, which is inversely proportional to the ionization density [57]. The denser a charge distribution, the easier (and faster) it is for an ionization electron to recombine.

The recombination time constant is the dominant component of the S1 pulse shape when no electric field is applied, but the presence of an electric field exponentially quenches recombination. As the field gets stronger, electrons are more easily stripped away and are less likely to recombine. Therefore, as the applied electric field goes to infinity the number of

ionization electrons that recombine goes to zero [58], and the triplet decay time constant dominates the time structure of S1 pulse shape.

The case of nuclear recoils is different because the high density of ionization results in rapid recombination, so the recombination time is essentially zero. Thus, the only parameter necessary to describe the time evolution of the pulse is the ratio of production of singlet and triplet states.

The ability to discriminate between NR and ER interactions is what makes a xenon detector powerful. Given the differences in the Singlet/Triplet lifetimes for each process as outlined in Table 2.1, one could imagine performing a liquid-only experiment with no applied drift field and measuring the falling edge of the S1 pulse shape. Since the singlet and triplet lifetimes are different, the pulse shape produced by an ER and an NR interaction would be slightly different; however, in practice, these lifetimes are too similar to adequately discriminate, so a dual phase detector with non-zero field is used instead.

2.1.4 Electroluminescence from Drifted Charge

The initial energy deposition produces prompt scintillation and ionization electrons. If these electrons can be collected and measured, discrimination between ER and NR events is possible. To achieve this, an electric field is applied across the target to drift these ionization electrons to a charge collector. Rather than collecting the charge with some anode and charge amplifier, it is simpler to use the properties of xenon to convert the ionization electrons into a proportional amount of delayed scintillation light.

The delayed scintillation, or S2 signal, is produced in a TPC by electrons that have escaped recombination, are drifted through the detector volume, and are extracted to a higher electric field region, where they produce light via electroluminescence. The shape of the S2 pulse, for events originating not near the liquid-gas interface, is roughly Gaussian with characteristic width determined by several parameters: a) the mean free path for electrons to produce photons in xenon gas, b) the drift velocities in the detector volume drift region and the electroluminescence region, c) the singlet and triplet state lifetimes, and d) the electron diffusion in the drift region and the electroluminescence region.

The number of photons produced by electrons in the electroluminescence region is a

linear function of electric field per unit density, also known as the reduced field, according to [59]

$$\frac{n_{ph}}{x} = \left(0.140\frac{E_e}{N} \times 10^{17} - 0.474\right) \times N \times 10^{-17}. \tag{2.9}$$

In (2.9), n_{ph} is the number of photons produced per ionization electron, x is the distance traveled by the electron in cm, E_e is the electric field given in V/cm and N is the number density of the gas in atoms/cm^3. The distance traveled by the electron, x, is understood to be the mean free path of the electron to produce one photon in the electroluminescence region.

The ionization electrons in the drift region propagate along the direction of the electric field, and quickly reach terminal velocity (v_{drift}) due to collisions with xenon atoms [60–62]. Upon extraction into the electroluminescence region, the electric field typically increases. They collide with xenon atoms, deposit energy, and are re-accelerated. In the case of liquid xenon as the DR, there are two established empirical models for drift speed [60, 61].

In a manner similar to the S1 process, the S2 pulse is generated via the direct excitation and subsequent de-excitation of the xenon. The de-excitation contains a singlet and a triplet component, with characteristic time constants. The average singlet decay time constant is 5.88 ± 5.5 ns and the triplet decay time constant is 100.1 ± 7.9 ns [63–72]. The triplet lifetime and singlet lifetime in gas are different than in liquid. There is no large consistency between these measurements except for the 100 ns triplet lifetime.

Ionization electrons that drift in a TPC will experience diffusion in three dimensions: the longitudinal (parallel to the direction of drift) and the transverse (perpendicular to the direction of drift) diffusions. The transverse diffusion is rotationally-symmetric about the longitudinal axis. The resulting electron cloud is an ellipsoid with minor axis along the direction of drift. The diffusion can be described as [73]

$$\sigma_L = \sqrt{2D_L\Delta t} \tag{2.10}$$

$$\sigma_T = \sqrt{2D_T\Delta t} \tag{2.11}$$

$$\Delta t = \Delta z / v_{drift} \tag{2.12}$$

where, σ_L and D_L (σ_T and D_T) are the longitudinal (transverse) diffusion width and constant respectively, Δt is the drift time, and Δz is the longitudinal drift distance. Transversal diffusion in the drift region has no first-order effect on the shape of the S2 pulse, which is mostly determined by the temporal (hence longitudinal) distribution of electrons. In fact, the transverse diffusion is smaller than the position resolution of a typical TPC [74–76]. The longitudinal diffusion in liquid xenon is an order of magnitude smaller than transverse, but it has a critical effect on the S2 shape because it dictates when the electrons are extracted from the liquid into the gas. Both longitudinal and transverse diffusion in gas have a negligible effect on the S2 pulse shape as long as the Δz of the event is large. The following reasons describe why: a) the atomic density is much lower, b) the electric field in the gas region is much higher leading to a smaller value of Δt in (2.10), c) the drift distance in the gas is smaller than in the liquid, and it is identical for each event.

The S1 and S2 pulses are the result of complicated physics. To assist in the understanding and to accurately simulate the physical detector, a software model to simulate these pulse shapes incorporating the features described above was developed. This model is described in more detail in subsequent chapters.

2.2 The LUX Detector

LUX is a dual phase xenon time projection chamber with 370 kg of liquid in the active volume. The detector was assembled completely on the surface, with construction completed in summer 2011. After a proof-of-concept operational run on the surface, LUX was transported underground, in a hermetically sealed fashion, in July 2012. Underground deployment and detector commissioning began in earnest and continued through spring 2013. The first science run was completed in summer 2013, and a first result was published in early 2014.

LUX operates in a fashion similar to that described in the sections above, with the ability to discriminate between ER and NR events. It is a counting experiment sensitive to nearly any particle interaction but searching for a rare process. The standard way to discover new physics with this type of detector is to minimize and completely understand all interactions of known processes. In principle, the design goal is one where zero signal (NR) events from

backgrounds are observed during the rare event search. Therefore, any signal observed should be the result of some new phenomenon, for example elastic scattering of WIMPs off nuclei. For this reason, the background signals in LUX must be minimized.

2.2.1 LUX Design Goal

The goal of LUX is to be sensitive to WIMPs with spin-independent cross-sections of 2×10^{-46} cm^2 in the $\sim$100 kg fiducial volume of the detector. This corresponds to an expected WIMP rate of 0.5 events/100kg/month. This requires that over the 90 day WIMP search period, zero WIMP candidate events can be due to a background interaction. Primary sources of backgrounds are ER events from γs that leak into the WIMP search band and NR interactions from neutrons. Based on past experiments's successes [77, 78], LUX is designed to reject 99.3 - 99.9 % of ER events assuming a 50% acceptance of NR events. This powerful rejections leads to a goal for γ and β rates in the fiducial volume of $< 8 \times 10^{-4}$ events/kg/keV/day. An overview of LUX deployed in the underground laboratory is shown in Figure 2.3

2.2.2 Background Mitigation

To achieve the desired sensitivity of LUX, ER and NR background interactions must be minimized. If LUX was operated on the surface of the earth, it would be perpetually saturated due to interactions with cosmic ray muons. To mitigate these interactions, the detector is operated deep underground at the Sanford Underground Research Facility in Lead, SD. The underground facility shields LUX with 4850 ft, or 4300 m.w.e. (meters of water equivalent), of rock overburden. This stops all but the highest energy muons from reaching the detector. The simulated flux of muons that could interact with the active volume is 4.4×10^{-9} cm^{-2}s^{-1} [79]. These particular high-energy muons can interact directly in LUX, adding to the ER background, or interact with the rock in the underground cavern producing spallation neutrons which could produce additional NR backgrounds.

Spallation neutrons are not the only source of background from the cavern rock. The measured ^{238}U (^{232}Th) levels in the surrounding rock is 0.16 (0.20) ppm or 2 (0.8) Bq/kg. Potential ER and NR backgrounds from these sources are mitigated by deploying the LUX

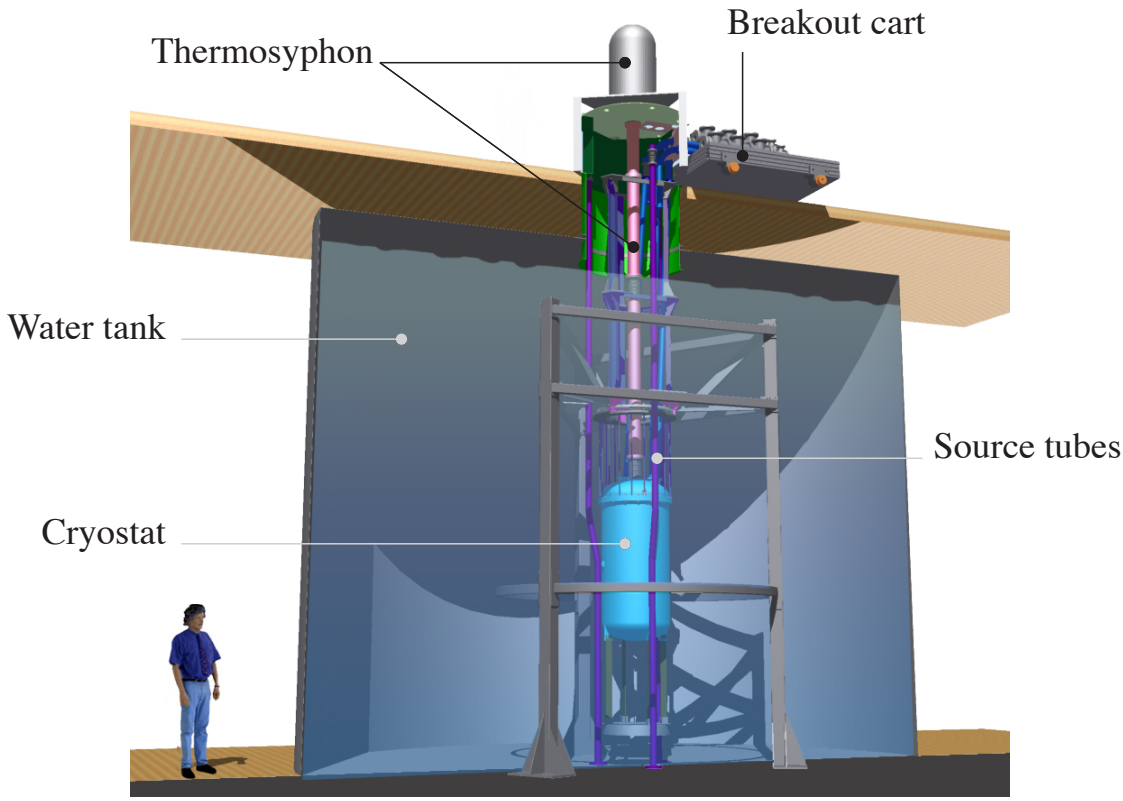

Figure 2.3. A drawing of the LUX detector as deployed in the underground laboratory. The active volume of the detector, contained within the cryostat, sits within a 76,000 gallon (300 tonne) water tank which shields it from ER and NR backgrounds from natural radioactivity in the surrounding rock and spallation neutrons produced by cosmic ray neutrons. The thermosyphon provides the cooling power to liquify the xenon, thus producing the target. The breakout cart provides a dry connection between the front end electronics and the detector, located 16 feet below in the water tank.

detector within a 76,000 gallon water tank, shown as part of Figure 2.3. The LUX shield is 7.6 m in diameter and 6.1 m tall. The water shield reduces the external backgrounds such that the dominant background source is associated with intrinsic radioactivity of internal detector components.

Furthermore, the water shield is an active muon veto. Only the highest energy cosmic ray muons will penetrate to the depth of the underground laboratory. Per simulations, these muons have an average energy of 321 GeV and are traveling nearly radially inward [79]. Therefore, if such a muon were to enter the LUX water tank, it would produce approximately 200 Cherenkov photoelectrons in the 20 ten inch photomultiplier tubes (PMTs) deployed within the water tank. The interior of the tank is also lined with tyvek sheet material, as it is highly reflective of the Cherenkov radiation. The combination of the PMT coverage and the reflectivity of the tyvek leads to $> 90\%$ efficiency in tagging and rejecting events that result from cosmic ray muons. A photograph of the Cherenkov water shield under construction is shown in Figure 2.4.

The final type of background to mitigate results from intrinsic radioactivity of internal detector components. Every material has some intrinsic amount of U/Th/K, and a material screening program to measure these internal contaminations is used to carefully select the most radio-pure materials. Highly sensitive gamma-ray-spectrometers are used to measure the rates of long-lived radioactive impurities within the detector materials. These levels are cataloged and included in the LUX simulation to ensure that the background goals outlined above are achieved. A further discussion of the material screening program and subsequent background model is found in detail in Chapter 4.

2.2.3 Detector Internals

The design of the LUX detector is conceptually simple. It is essentially a large, cylindrical container filled with liquid xenon. Of course, it is technically much more complicated, and these aspects are described.

2.2.3.1 Cryogenics

As a dual phase detector, LUX must operate at a temperature and pressure that allows for xenon to be present in both the liquid and gas states. Furthermore, according to (2.9), the

Figure 2.4. The interior of the LUX water shield. Tyvek panels are being applied to the sides and top of the tank as this material is highly reflective of the Cherenkov photons that are produced when a high energy muon enters the water. 20 ten inch photomultiplier tubes complete the veto system.

	Density (g/cc)	Tensile Strength (MPa)	^{235}U (ppb)	^{232}Th (ppb)	^{40}K (ppm)
Titanium (CP1)	4.5	434	< 0.2	<0.4	< 0.2
Stainless Steel	8.03	860	0.17	0.57	3
Copper	8.94	220	< 0.035	< 0.063	< 0.12

Table 2.2. Properties of three common materials used to build rare-event search experiments, such as LUX. Titanium is an attractive metal given that it is less dense than both stainless steel and copper, and it is a stronger metal than copper. It also contains lower levels of intrinsic radioactivity. All measurements quoted are from direct gamma ray spectroscopy using a Germanium detector. Data from [80, 81].

number of scintillation photons produced is directly proportional to the number density of the medium. Thus, as the pressure increases, the number density increases, and the denser medium leads to more scintillation light. To maximize the scintillation light, LUX xenon pressure was 2 atm, corresponding to a temperature of ∼165 K.

This temperature and pressure are maintained using a cryostat, which consists of two nested vessels built from radio-pure materials. Standard practice in the field has been to construct the vessels from a combination of copper and stainless steel. Copper stock can be obtained that has very low levels of intrinsic radioactivity, but it is very malleable. Stainless steel, on the other hand, tends to contain higher levels of radioactivity, but it is stronger. LUX was the first such experiment to use titanium to construct the cryostat vessels. Titanium is less dense than both steel and copper, and it is stronger than copper. LUX was able to obtain enough titanium stock (∼325 kg) with low levels of intrinsic radioactivity with which to build the vessels. Select material properties of titanium, copper, and stainless steel are listed in Table 2.2. Following conventional design, the cryostat vessels are separated by a vacuum space to ensure no thermal conductivity between the inner vessel and the outer vessel. This allows for the careful control of the temperature. The nested cryostats, along with other features, are shown in Figure 2.5. The inner vessel serves as the xenon space. It is a 39.75 inch tall, 24.25 inch cylinder with a dome welded to the bottom and a 27.75 inch flange welded to the top. The only thermal contact between the inner vessel and the outer

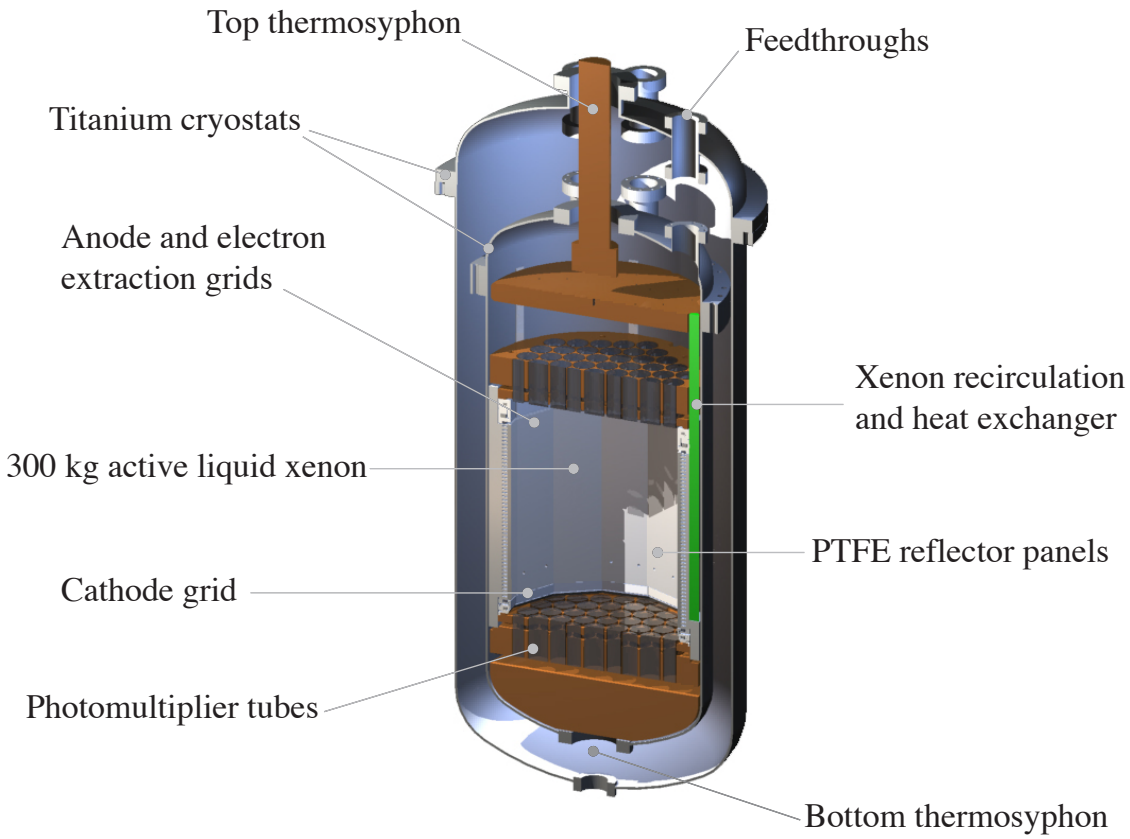

Figure 2.5. The main features of the LUX cryogenics system with some additional information about the internal detector components. Stable temperature control is allowed because of the titanium cryostats. The thermo-syphon system (top and bottom shown) provides the cooling power necessary to maintain the liquid xenon temperature. The target liquid is contained within the inner titanium vessel and is surrounded by teflon panels used to reflect the ultraviolet scintillation light to the PMT arrays. The anode and cathode grids provide the electric field that drifts the ionization electrons to the top of the active volume where the electroluminescence occurs.

vessel occurs at three feedthroughs which allow for instrumentation cables to penetrate the active volume.

The boiling point of xenon is higher than that of nitrogen. Hence, liquid nitrogen is used in conjunction with thermal impedances to maintain the temperature of the liquid xenon. A thermo-syphon system is used to deliver the liquid nitrogen cooling power to the xenon. A thermo-syphon consists of a sealed tube with some amount of nitrogen gas. At the top,

the tube is immersed in a liquid nitrogen bath. This condenses the gas inside, making it heavier. Gravity pulls the condensed gas to the bottom of the tube which is attached to the detector. The warm detector transfers some heat to the thermo-syphon, causing the condensed nitrogen gas to evaporate and rise back to the top where the process repeats. In this way, heat is effectively wicked from the detector. Each LUX thermo-syphon is capable of delivering ∼500 W of cooling power, and four thermo-syphons are attached: One each at the top and the bottom, and two along the sides.

2.2.3.2 Time Projection Chamber

The LUX TPC is a dodecagonal plastic structure contained within the inner titanium vessel enclosing the target volume. The internal structure of the TPC, shown in Figure 2.6, is fully supported by hanging from the upper titanium dome that mates with the inner titanium vessel. Because of radio purity concerns (see Table 2.2), the main structural material used in the construction of the TPC is copper, as is evident in Figure 2.6,. The copper used is C101 oxygen free high thermal conductivity (OFHC) grade material. This ultra-pure copper contains low levels of intrinsic impurities making it an ideal material to use near the target.

There are four main pieces of copper. Working from the top, the uppermost piece is mounted directly to the inside of the titanium dome. It is a 55 cm diameter disk that is 5 cm thick. It connects to the top thermo-syphon to provide cooling power directly to the xenon. Since copper is a high-density material, it also serves as a shield from gammas. Finally, all other components hang directly from this piece of copper via six titanium straps.

Next, 15 cm below the top gamma shield is the top PMT array. This copper piece contains 61 holes arranged in a honeycomb patters to support the 61 PMTs in the top array. The exposed copper surface facing the target, in the space between PMTs, is covered in polytetrafluoroethylene (PTFE) material to aid in the reflection of scintillation light to the PMTs. The bottom PMT array, located at the lower end of the active region, is a mirror image of the top array.

The bottom piece of copper acts as a gamma shield as well. It has a rounded bottom designed to fit into the domed structure at the bottom of the titanium vessel, which also serves as a xenon excluder by filling up most of the available volume. Otherwise, this space

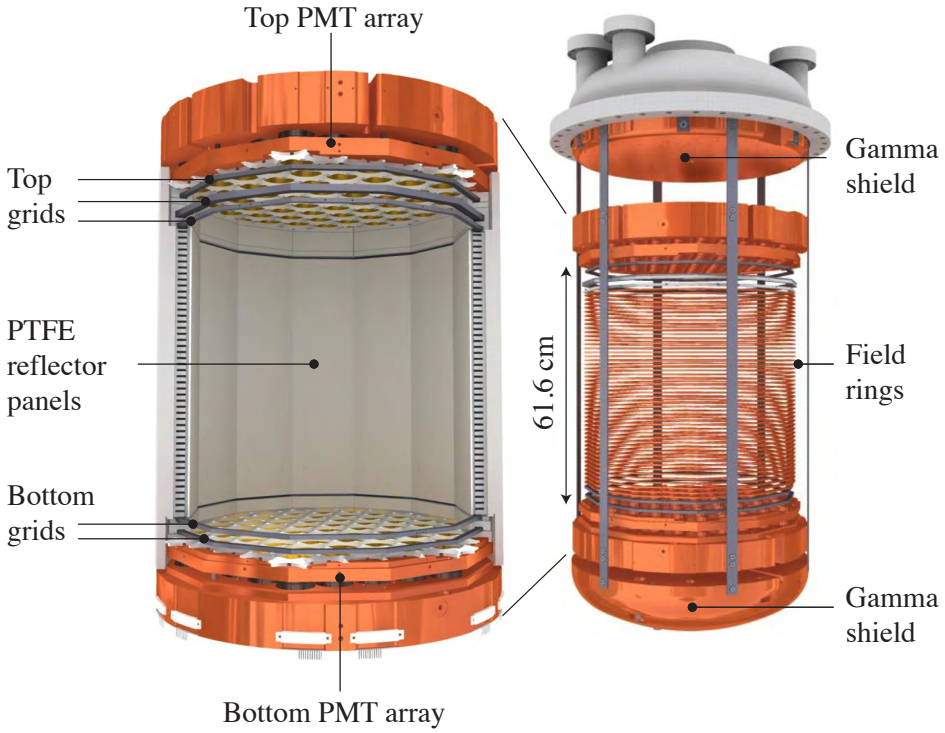

Figure 2.6. The internal structure of the LUX TPC. The gamma shield connects directly to the top thermo-syphon, and the remainder of the internal structures hang from it. The top and bottom PMT arrays contain 61 PMTs in copper support structures. The PTFE reflectors provide $> 90\%$ reflectivity to the ultraviolet scintillation light. From bottom to top, the grids are: 1.) Bottom PMT shield; 2.) Cathode; 3.) Gate; 4.) Anode; 5.) Top PMT shield.

would be filled with inactive liquid xenon, which would have been a waste of this expensive material and may also have been a source of spurious scintillation signals. The bottom gamma shield also acts as a thermal sink as it is connected directly to the bottom thermo-syphon.

Between the top and bottom PMT shields is open space. This is the active region of the detector and is filled mostly with liquid xenon. The active region is surrounded by twelve PTFE panels, giving the interior its dodecagon shape. PTFE is chosen because it is highly reflective to ultraviolet xenon scintillation light. The PTFE also acts to support the field shaping rings, discussed below.

In order for the active volume to be a TPC, an electric field must be applied. This is accomplished via voltages applied to five grids of thin wires spaced throughout the volume.

First, the top and bottom most grids, referred to as the top grid and bottom grid, contain 206 μm wire spaced 1 cm apart. These grids are placed 2 cm from the top and bottom PMT arrays to shield the photocathodes from the high voltages that are applied to the other grids. Optically, these grids are 98% transparent and thus allow for efficient light collection.

Located 4 cm above the bottom grid is the cathode. It contains the same 206 μm wire spaced 5 mm apart, giving it 96% transparency. The cathode and bottom grid are mechanically designed such that 100 kV could be applied to the cathode (with bottom grid at ground) and neither grid would experience any mechanical issues. During the initial science run of LUX, various issues limited the applied cathode voltage to be -10 kV.

The liquid surface, maintained by the weir, is nominally 49.5 cm above the cathode. Mounted 5 mm below the liquid surface is the gate grid. This grid uses 50 μm wires spaced 5 mm apart, giving it a transparency of 99%. Its purpose is to allow the drift field in the liquid to be different than the electron extraction field in the gas. It operated at -1 kV, so the drift field was 181 V/cm. Based on this drift field drift distance, the drift speed of an ionization electron is 1.5 mm/μs and the maximum drift time is 330 μs.

To ensure straight field lines pointing from the gate grid to the cathode, copper field shaping rings spaced 1 cm apart were placed from the cathode to the gate behind the PTFE. A resistor chain between the cathode and gate fixed the voltage of each field ring, with adjacent rings having a 1 GΩ resistor between them.

The distance between the gate and anode is 1 cm. The anode is mounted 4 cm below the top PMT shield in the gaseous xenon. It is constructed as a mesh of 30 μm wires spaced 0.5 mm apart, giving it a transparency of 88%. The voltage applied to the anode was 3.5 kV, so the field that extracted the electrons from the liquid into the gas was 6 kV/cm. The 1 cm spacing between these two grids defines the electroluminescence region.

See Chapter 5 for a detailed discussion of the ER and NR discrimination capabilities from calibration sources.

2.2.3.3 Gas Handling

The LUX gas handling system is designed for the continuos circulation of xenon for the removal of electronegative and molecular impurities which decrease the charge and light

collection efficiencies of the detector. The main purification is achieved in the following way: 1.) Liquid xenon at the liquid-gas interface flows into a weir. From the weir the liquid travels through a series of heat exchangers, emerging through the detector as a gas. The gas flows through a commercially available SAES MonoTorr heated getter, which removes the impurities. The gas re-enters the detector, passing through the heat exchangers, which liquify it. The purified liquid then enters the detector at the bottom. Gas flow of 50 SLPM (420 kg/day) is achieved via a diaphragm pump.

The fluid path through the heat exchangers is shown in Figure 2.7. At the top of the active region, the liquid spills over the weir into the reservoir, fixing the liquid level. The reservoir is designed to allow for temperature and circulation rate variations that otherwise would affect the liquid level. Upon leaving the reservoir, the liquid flows into the evaporator side of a dual-phase heat exchanger and evaporates. This gas then flows through a single phase (gas) concentric tube heat exchanger and leaves the detector at nearly room temperature. At the same time, room temperature gas is flowing in the opposite direction through the single phase concentric tubes and is transferring heat with the outgoing gas, beginning the cooling process. Next, this cool gas enters the condenser side of the dual-phase heat exchanger and condenses. This system has been demonstrated to work at greater than 94% efficiency [82], considerably reducing the required cooling power.

The gas handling system also allows for the injection of several calibration sources into the active region of the detector. ^{83m}Kr and methane with a small amount of ^{3}H added are introduced in small quantities as warm gasses into the circulation path after purification. The amount of calibration gas that mixes with the xenon gas of course defines the final activity of the source in the active volume. The calibration gas is carried by the xenon through the heat exchangers to enter the active volume with the liquid xenon. It quickly diffuses through the entire liquid volume, providing an internal calibration source. See Chapter 5 for a more detailed discussion of these sources.

2.2.3.4 Electronics and Data Acquisition

LUX uses two arrays, each consisting of 61 PMTs, to detect the scintillation light. The PMTs are housed in the copper holders described above and arranged in a honeycomb pattern.

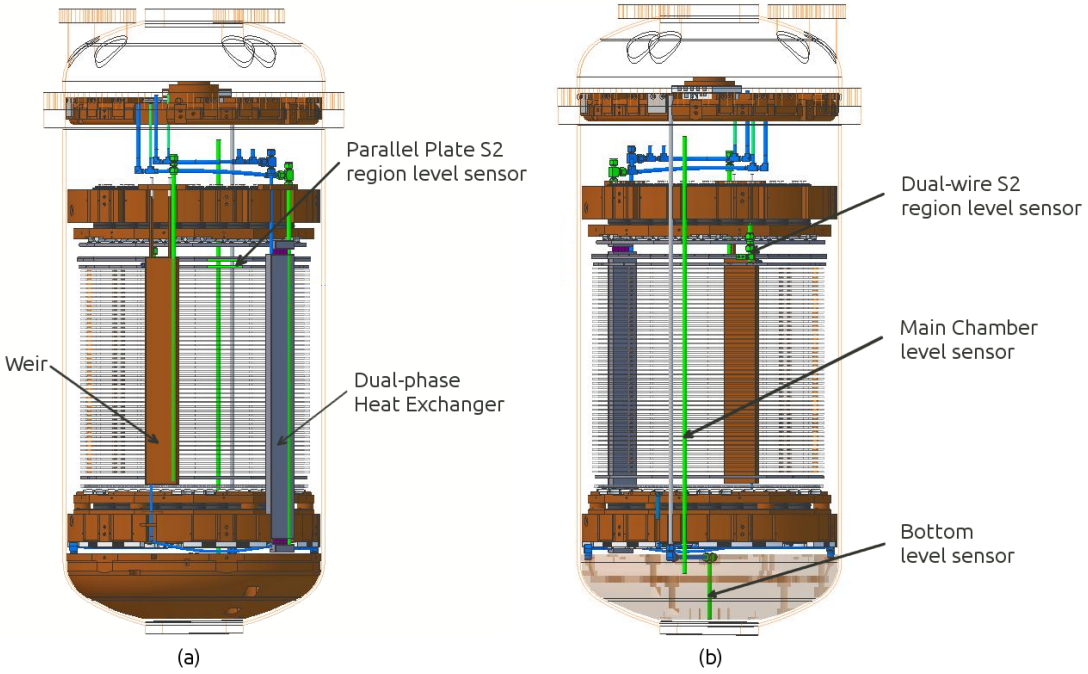

Figure 2.7. The internal circulation system in LUX. The liquid spills over the weir into the reservoir. This allows the liquid level to remain constant if fluctuations in circulation rate and temperature occur. Upon exiting the reservoir, liquid flows into the evaporator side of the dual-phase heat exchanger. It transfers heat with gas entering the condenser side and leaves the detector as a gas. The gas is purified and returned, where it is condensed in the condenser side of the dual-phased heat exchanger and re-enters the active region at the bottom.

This PMT, the 2 inch Hamamatsu 12-stage R8778, was developed specifically for operation in liquid xenon. It has a photocathode that is sensitive to the 175 nm scintillation light and has a relevant quantum efficiency of ∼33%. Operating at ∼ −1400 V, the gain of the PMTs is 3.3×10^6, with ∼34% pulse-to-pulse variation in that gain. The PMTs are cabled with coaxial cable designed for operation in cryogenic systems and are heat-sunk to prevent liquid disturbances (bubbles). Each cable is 10 m long, ensuring all signals have the approximately the same level of attenuation and equal transit time.

The signals from the PMTs are then read out by the LUX electronics chain. The design goal of the LUX electronics was to resolve > 95% of the single photoelectrons in any PMT from a fluctuation in the baseline noise. The analog chain provides two stages of amplification before digitization.

The first, the preamplifier, is located as close to the detector as possible (10 m of cable

between PMT and amplifier). It contains a single integrated circuit design that provides a gain element between the xenon space and the lab. The nominal voltage gain of ×5 can be reduced by a factor of 10 using a selectable voltage divider at the input. The operating voltage is provided by the postamplifier.

The output of the preamplifier is sent through 42 feet of 50 Ω coaxial cable to the postamplifier. The postamplifier, assuming the nominal PMT gain above, fixes the single photoelectron pulse height at 4 mV [83]. The pulses are shaped by a 4-pole Bessel filter with cut off frequency of 60 MHz. The postamplifier splits the input signal into two, sending one to the digitizer and one to the trigger.

The signals are digitized by 16 Struck 8-channel Fast ADC modules at 100 MHz with 14 bit resolution. Each has 2 × 128 k sample dual memory banks that allow for acquisition on one bank while the other is transferring data to storage. The boards are connected to a VME bus capable of transferring data at 80 MB/s. The firmware was developed by LUX to operate in Pulse Only Digitization (POD) Mode, such that only pulses that go above a predetermined threshold are digitized, drastically reducing the data storage required [83]. Individual PMT channels produce PODS, and the entire time window of interest, summed together, is a referred to as a SumPOD.

The trigger uses the pulse shape information of the PMT signals to select potential dark matter events and reject background events. It can differentiate between narrow (S1-like) and wide (S2-like) pulses. Decisions can be made by looking for narrow pulses, wide pulses, or a combination of both types of pulses within a time region. The system uses two 14-bit, 64 MHz, 8-channel digital signal processors. Data are shared between these signal processors and the trigger builder where the decision is made. If the trigger decides an event is interesting, it sets a flag in the Struck digitizer; however, all data, regardless of trigger flag, are digitized and written to disk.

An event is defined as a 1 ms window in the time stream where an S2-like pulse was detected by the trigger. After acquiring an 8-hour dataset, the trigger information is used to group the PODs and SumPODs into these event windows. By definition, the event window contains 350 μs of time before the S2-like pulse (the maximum electron drift time from the

S1) and 650 μs of time after the S2-like pulse (to ensure all multiple scatters are accounted for).

The detector and data acquisition systems were designed to work as described above. The actual operation and performance is described in detail in Chapter 6.

2.2.4 LUX Construction

The LUX detector was designed to be fully constructed on the surface and transported underground as a completed unit. The surface construction of the xenon space occurred during a nine month time period that ended in summer 2011. This assembly took place in a clean room to keep as much contamination (dust) out of the xenon space as possible. Dust contamination would act to reduce the charge and light collection efficiencies. After a proof-of-concept operation period on the surface to fully test the detector systems and their respective operation within a water tank, the xenon was removed and the inner vessel was evacuated and the transportation procedure was begun.

2.2.4.1 Detector Transport

LUX was intended to operate within a water shield. This makes instrumenting the detector difficult because electronics and readout systems must remain dry. The solution is to connect the detector to the electronics systems via three 16 feet long 4 inch diameter stainless steel umbilicals. These umbilicals acted as extensions to the xenon space, thus extending inactive gaseous xenon all the way out of the tank. The complete assembly of the detector, including electronics connections through the umbilicals was completed on the surface.

The detector, loaded onto a transport cart and connected to the instrumentation breakout, was moved as a hermetically sealed unit from the surface assembly location to the underground laboratory. To protect the exterior surfaces and keep them clean, the transport unit was packaged in plastic and foam. Figure 2.8 shows the unit ready for transport in the surface facility. The left is the detector loaded onto the cart and the right is the instrumentation breakout. The connecting umbilicals are visible. To move the unit from the surface facility to the elevator taking it underground, it was carefully transported approximately 1000 feet outside and up a slight incline on a fork lift. A photograph of this is shown in Figure 2.9. The fork lift ensured the acceleration of the detector never exceeded gravity

Figure 2.8. The LUX detector is packaged and ready to leave the surface facility. On the left is the detector on its transport cart, and on the right is the instrumentation breakout. The three umbilicals are visible. Everything is packaged in plastic and foam to keep dust off. Photograph by Jeremy Mock.

(no extra force was applied) and the tilt was never more than one degree from horizontal. Thus the thousand feet took approximately two hours to traverse.

Once in the elevator building, the detector was loaded onto "air skates." When highly pressurized air is applied, the unit essentially hovers and can easily be pushed. This allows for high maneuverability which was required to negotiate some of the tight tunnels underground. The unit, floated on air, was pushed onto the elevator and began its decent down. A trip that normally takes ten minutes was slowed down to take almost two hours. Upon reaching the underground level, it was pushed on the air skates all the way to the underground laboratory where it was unpackaged. Figure 2.10 shows the detector being pushed with the air skates. The yellow hose carries highly compressed air from a compressor to the control panel, visible on the right of the photograph. The red hoses carry the compressed air from the control panel to the individual air skate units. The metal sheets on the ground were necessary to ensure a flat, continuous surface to hover on.

Figure 2.9. The LUX detector and instrumentation system, attached as a unit, are being transported from the surface assembly facility to the building where they will be loaded into an elevator to go underground. During this 1000 foot trip, the unit never experienced any external forces (except gravity) and was never tilted more than one degree from the horizontal. Photograh by Matt Kapust.

2.2.4.2 Underground Installation

As soon as LUX arrived underground, work began to install and commission it for WIMP search. The detector, which weighs ∼2750 pounds, needs to be lowered into the center of the water tank so the systems can be commissioned. Due to inadequate overhead clearance, the detector needed to be lowered in stages with additional infrastructure built above it with each stage. Three such stages were required. The first such stage is shown in Figure 2.11. Here, the support ring is being installed. The support ring allows LUX to be suspended one meter below any other infrastructure material, keeping as much radioactivity away as possible. Above the support ring, a tower was contracted in two stages. The cryogenic systems were installed on this tower as it was constructed, as only the xenon systems were built and sealed on the surface. The tower needed to support the weight of the detector until it was in its final assembled position when the weight was transferred to the stand, mounted inside the water tank. The final assembled system is shown in Figure 2.12. Once

Figure 2.10. The LUX Detector arriving underground and being pushed on the air skate system. Compressed air, carried in the yellow tube to the control panel, visible on the right of the photograph, pushed down from seven "air skates" that LUX rested on. This caused the transport unit to hover, and it could be pushed, providing the maneuverability necessary to negotiate the tight underground tunnels. The sheet metal visible on the ground provided a smooth, continuous surface for the air to push against. Photograh by Matt Kapust.

the assembly was complete, all the systems were integrated together over a period of several months. The commissioning was completed in early 2013. After cooling the detector and condensing the target xenon, the science run began in spring 2013.

Figure 2.11. Due to overhead clearance constraints, the detector needed to be lowered into the tank in three stages. After each stage, additional infrastructure was built above. Here, the support ring is being installed. The detector hangs one meter below the support ring, and all other infrastructure is mounted above it. This minimizes the material close to the detector. Photograh by Jeremy Mock.

Figure 2.12. The LUX detector installed in the water shield. The weight is fully supported by the detector stand, the large structure mounted to the floor of the tank. The detector hangs from the support ring. Above the support ring is the infrastructure that delivers cryogenics and circulation systems. The tube in the background guides calibration neutrons into the active volume (discussed in later chapter). The scientist in the photo is the author, Jeremy Mock. Photograh by Matt Kapust.

Chapter 3

Modeling and Simulating LUX

The LUX detector is a complex amalgamation of systems designed to search for a rare process. To fully understand the integration of these systems, a full and accurate simulation is useful and necessary. The two main goals of a simulation of LUX are: 1) to model the processes underlying the response of the detector to the passage of particles and 2) understand the properties and efficiencies of the detector, which lead to the formation of measurable quantities and recorded data. To achieve these goals, two software packages were developed. The latter goal is addressed by the LUXSim package, which builds an accurate model of the detector in software, and the former is handled by the Noble Element Simulation Technique (NEST) package, which accurately simulates the complex scintillation physics in a noble element such as xenon. Both of these are discussed below.

3.1 LUXSim

The standard high energy physics simulation package, developed at CERN, is called Geant4, a toolkit for the simulation of the passage of particles through matter [84, 85]. Geant4 has been expanded to include low energy nuclear processes, thus making it useful for rare event searches like LUX. In the typical Geant4 framework, the primary particles are generated separately from the active detector components, providing a clear distinction between the beam and the hardware used to measure the beam. Because LUX is searching for a very rare process, recording simulated data only from active detector components is not enough as passive components can have effects on the low energy depositions as well. The LUXSim

package [86] was developed to allow all detector components to actively engage in the energy deposition and subsequent photon propagation processes.

To accurately simulate LUX, a complete and accurate model of the detector geometry and an inventory of physical processes is necessary in code. Geant4 allows one to import schematic drawings of systems to build a geometry file, but this is not the approach used in LUXSim. Rather, each component is built from a library of materials. This means each component can have an arbitrary number of radioactive sources attached to it, a necessity given that large sources of background are the detector materials themselves. It also allows for components to be shaped in as-built configurations, which can differ from the designs.

A LUXSim rendering of the detector geometry is shown in Figure 2.6. This design should be compared to Figure 2.5, the design concept. Nearly all features are included, such as the PMTs, reflectors, teflon walls, copper shields, field shaping rings, internal circulation components, titanium cryostats, wire grids external detector stand, water tank components, water, and cavern rock. The grids wires are each individually built because the transmission of light changes with the photon angle of incidence, and individual wires prove to be a more accurate model than a semi-transparent membrane.

In addition to the radioactivity levels, each material also has many other properties defined by the simulation. For example, optical properties must be defined for each material, since both the light and charge signals are measured via scintillation (S1 and S2). Since individual energy depositions can be quite small, LUXSim must be able to handle light propagation and collection down to the single photon level. Optical properties of liquid xenon have been studied [88], and these have been included in the simulation. Some optical parameters, such as the absorption length, must be carefully estimated. Because xenon is transparent to its own scintillation light, loss mechanisms are dominated by interactions with impurities within the xenon. The levels of impurity are not necessarily constant as the getter is continuously removing them, so a conservative estimate of 100 m is used [86] for the photon absorption length.

As described in the previous chapter, LUX uses two banks of PMTs to measure the scintillation light. The PTFE reflectors that line the active volume serve to channel scintillation

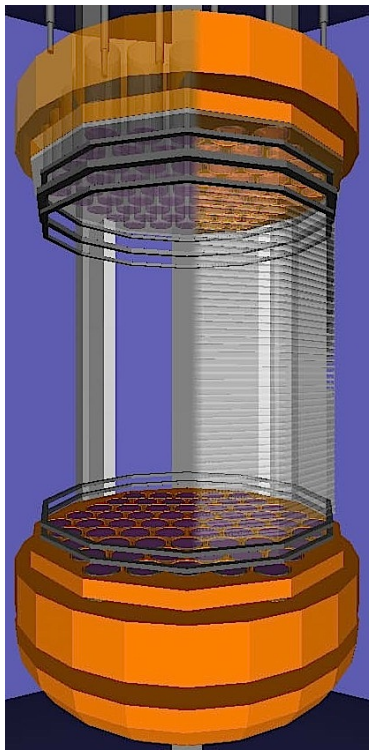

Figure 3.1. A rendering from LUXSim of the LUX detector. Note the major components of LUX are included in the simulation. Compare to Figure 2.5. Figure from [87]

light to the PMTs. The reflectivity of PTFE must be included in LUXSim to accurately simulate photon propagation through the volume. Measurements from [89] suggest that the reflectivity of PTFE is 100% diffuse at normal incidence, but has a specular component which increases with the angle of incidence.

In order to simulate the background rate, LUXSim uses and extends built-in Geant4 methods for placing radioactivity within the active volume or within detector components. Individual isotope decay information is imported from the Evaluated Nuclear Structure Data Files (ENDF) [50]. Decay generators that are included in the LUXSim package include AmBe, ^{252}Cf, ^{83m}Kr, lithium neutron generator, muon and spallation neutrons, ^{210}Pb, ^{226}Ra, ^{222}Rn, a WIMP generator, activated ^{129m}Xe and ^{131m}Xe, and the uranium and thorium decay chains. These specially modified generators are used to model the background spectrum. For calibration purposes, a user can put any isotope anywhere in the detector and the appropriate ENDF decay information is used.

Geant4 provides an excellent framework for building the LUX detector and handling energy deposition and scintillation photon propagation, as well as record keeping. It does not, however, offer a built-in method for handling dual phase xenon detectors. The physics of xenon scintillation is not included in any physics list, and the charge yield is highly dependent upon the applied drift electric field, a property that Geant4 does not take into account. To handle this more advanced physics, the Noble Element Simulation Technique (NEST) [55] software package was developed as an additional library for Geant4.

3.2 Noble Element Simulation Technique

The Noble Element Simulation Technique (NEST) software package [55] was developed as a set of additional libraries for use with Geant4 to simulate the scintillation, recombination, and electroluminescence properties that occur when a particle interacts in xenon. NEST uses energy-dependent and electric field-dependent models to determine the scintillation and ionization yields for both electron and nuclear recoil events, as well as a recombination model vetted against all known available experimental data. In this section, the models used in NEST are described.

3.2.1 Scintillation and Charge Yield

When a particle deposits energy in liquid xenon, it produces scintillation and ionization electrons, which are detectable, and thermal radiation which is undetectable. The number of scintillation photons produced, N_γ, is given by (2.6), and the number of electrons, N_e, by (2.7). Because any energy that is deposited as heat is modeled by the Lindhard factor, it is generally assumed that N_γ and N_e are perfectly anti-correlated. The relationship between the two is completely dependent upon r, the recombination probability. The recombination probability is known to be a function of the energy loss per unit length (dE/dx) and the applied electric field [90].

Doke *et al.* [91] derived a scintillation yield model for liquid xenon from Birks' Law. NEST uses a similar approach but models the recombination probability instead. This separates the scintillation yield into two constituent parts: the light from direct excitation and that from recombination. It is useful to express the recombination model in a piecewise

way dependent upon the track length of the incident particle. "Long" tracks are defined to be those that are longer than the mean ionization electron-ion thermalization distance of 4.6 μm [92]. For long particle tracks, typically resulting from higher energy depositions, a modified Birks' Law is used to model the recombination probability. In this formalism, electron-ion pairs are arranged in a long cylindrical pattern. The NEST recombination model for long tracks is

$$r = \frac{A\frac{dE}{dx}}{1+B\frac{dE}{dx}} + C \tag{3.1}$$

$$C = 1 - A/B. \tag{3.2}$$

A, B, and C are the model parameters that are tuned to fit the available data. The first term in (3.1) represents recombination that occurs when an ionization electron is captured by an ion other than its parent, known as volume recombination. The second term represents Onsager recombination, or those ionization electrons that recombine with their parent ions [91, 93]. A final constraint on the model is that as dE/dx approaches infinity, r goes to one.

For "short" particle tracks, the Thomas-Imel box model is used to model the recombination probability [51]. Here, electron-ion pairs are arranged in a box geometry [90, 93]. The recombination probability model for short tracks is

$$r = 1 - \frac{ln(1+\xi)}{\xi} \tag{3.3}$$

$$\xi = \frac{N_i e^2}{4a\epsilon kT}. \tag{3.4}$$

In this formalism, e is the electron charge, ϵ is the dielectric constant ($\epsilon = 1.96$), k is Boltzmann's constant, and T is the temperature of the liquid ($T = 165$ K).

NEST determines the recombination by tracking the recoil energies from Geant4 and applying the mathematical framework described. By tracking individual recoils, the macroscopic physics is maintained while remaining stochastic. For simplicity, NEST uses a mean work function: $W = E_{dep}/(N_{ex}+N_i) = 13.7$ eV [55]. It is expected that recombination would be enhanced at high dE/dx due to higher ionization density, but experimental results show that the recombination actually becomes independent of ionization density [51, 90, 93].

data considerations	best fit parameters
low energy points only	$\xi/N_i = 0.19$
high energy points only	A = 0.18; B = 0.42; C = 0.57

Table 3.1. The parameters of the NEST model that best fit the data. A degeneracy between A, B, and C could not be broken and is under further investigation.

This is handled in NEST because these interactions are strictly in the Thomas-Imel regime where the recombination depends on the energy (via N_i) and not dE/dx [55].

The scintillation yield model as described above applies when no drift field is applied. A, B, and C from (3.1) and ξ/N_i in (3.4) were treated as free parameters in order to fit existing scintillation yield data (see [55] for complete list of sources). An effort was made to include all available known experimental results. Various experiments quote scintillation yield as either absolute or relative. The fit to generate NEST parameters was done with absolute parameters. To translate relative data to absolute, the 511 and 122 keV lines were used as a benchmark. The mean-square of the residuals was minimized to find the optimal set of parameters for the model. Table 3.2.1 shows this best set of parameters. It should be noted that a degeneracy between A, B, and C was discovered as more than one set minimized the mean square residuals. No clear break in this degeneracy was found, so a set of optimal parameters was chosen, and work to better understand this is ongoing. Figure 3.2 shows the scintillation yield at zero field from data plotted with the NEST simulation using the best fit of parameters. Only two data sets [94, 95] are included in the figure to demonstrate the seamless transition from the Thomas-Imel parameterization to the Birks' parameterization of the NEST model. See Figure 5 in [55] for a more complete version with all world data available to date. Note also that Figure 3.2 shows only the scintillation yield because the model assumes that the charge yield is anti-correlated.

The presence of an electric field suppresses the recombination probability because ionization electrons will be less likely to recombine [49], which results in larger S2s and smaller S1s. To model the scintillation quenching, NEST parameters were tuned to available data at various electric fields. First, the presence of an electric field changes the definition of "short"

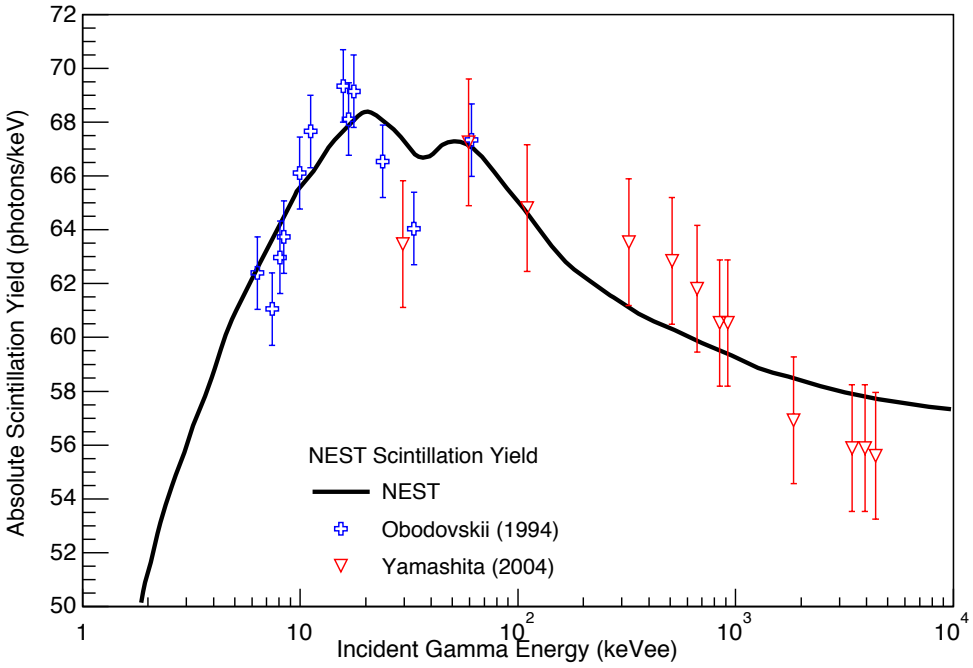

Figure 3.2. The scintillation yield NEST model at zero field compared with two data sources to demonstrate the validity of the piecewise nature of the model. See Figure 5 in [55] for the complete set of available world data.

and "long" in terms of the track length. The crossover point, dependent on the applied field, is best modeled as [55]

$$r = 69.5\sqrt{\frac{1}{E}}\,\mu m \tag{3.5}$$

where E is the electric field in V/cm. The Thoman-Imel and Birks' Law functions of the scintillation model do not change with electric field; however, the parameterizations do change. A, B, and C in (3.1) gain a field-dependent component in the form of a power law:

$$A = B = 19.2\,(E + 25.6)^{-0.83} + 0.27 \tag{3.6}$$

$$C = 0. \tag{3.7}$$

For short tracks, the field dependence of ξ/N_i is different for ER and NR events. This was necessary as no single electric field parameterization could be found to fully describe both

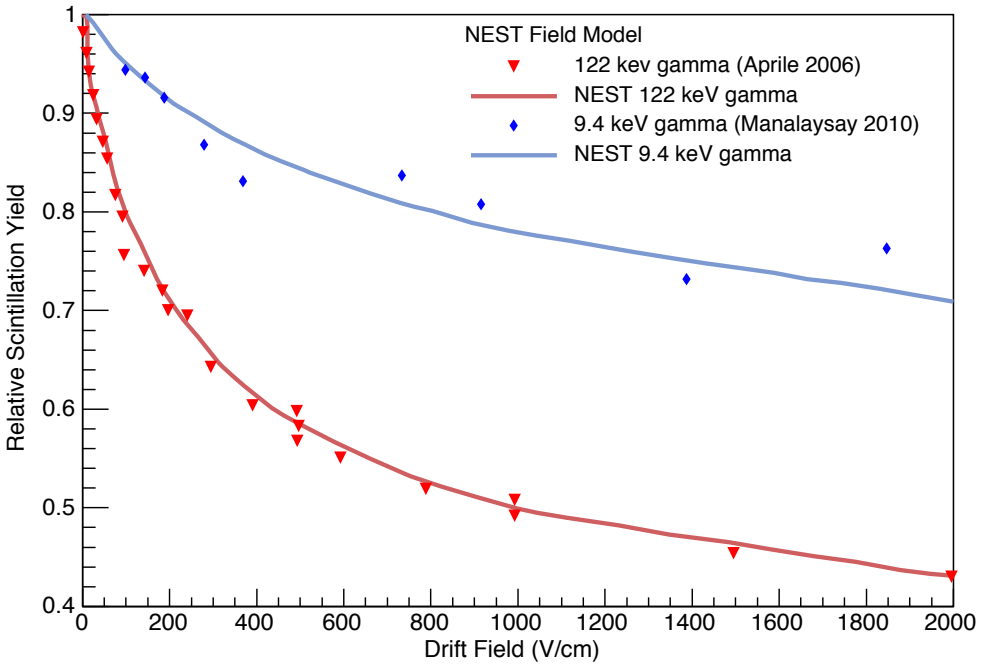

Figure 3.3. The NEST model for scintillation yield as a function of electric field. The model is compared with data from two different sources of different incident energy [96, 97]. The scintillation yield is relative (normalized) to the zero field value, unique for each given incident energy.

types of interactions. The field dependence of the Thomas-Imel parameter is

$$\left(\frac{\xi}{N_i}\right)_{ER} = 0.057\,(E)^{-0.12} \tag{3.8}$$

$$\left(\frac{\xi}{N_i}\right)_{NR} = -0.15\left(\frac{E}{V/cm} + 215.3\right)^{-0.018} + 0.21 \tag{3.9}$$

The electric field dependence of the scintillation yield model in NEST is shown in Figure 3.3 for ER events at two different energies [96, 97].

To effectively model LUX, NEST must accurately reproduce data not only for ER events but also for NR events. An example of a simulation of NR events including the NEST model is shown in Figure 3.4. The relative scintillation efficiency L_{eff} is plotted as a function of the recoil energy. This factor takes into account the fact that NR events lead to additional energy partitioning into the undetectable heat channel. Using the Hitachi correction to the Lindhard formalism presented in (2.1) at zero field, NEST can reproduce detector data [98–

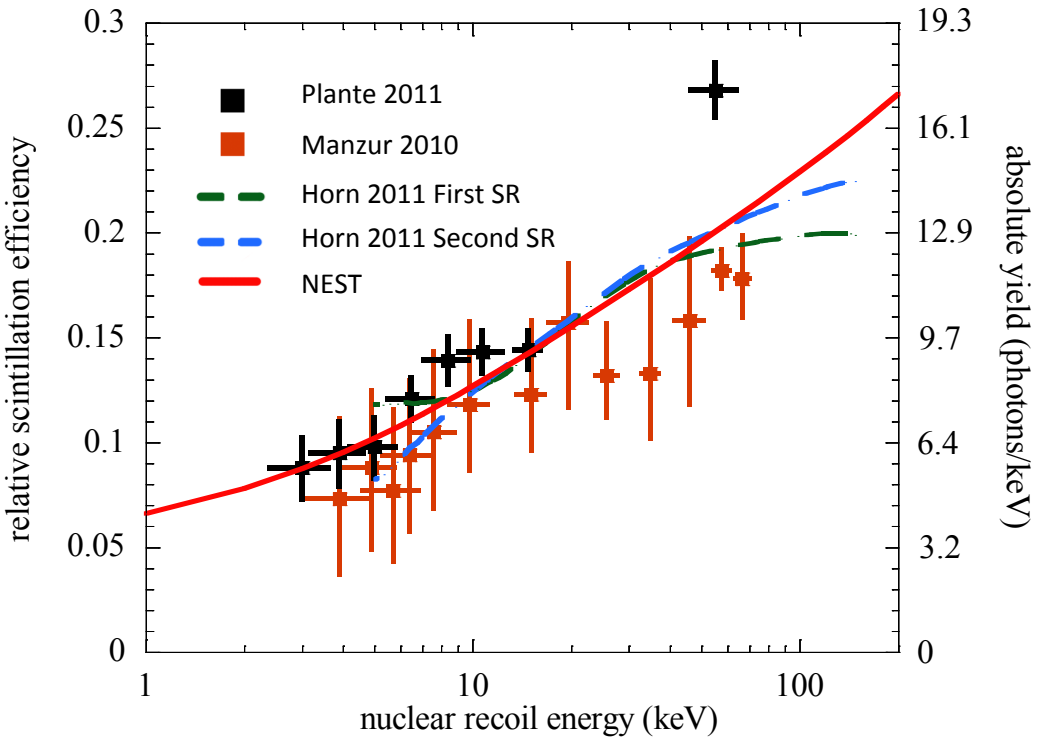

Figure 3.4. The NEST model for NR scintillation yield with the Hitachi correction to the Lindhard factor at zero field as a function of incident particle energy. The same scintillation model developed for ER events is applied here leading to excellent agreement with available data.

100] with the same models (3.4 and 3.1) used in the ER case.

3.2.2 Pulse Shape

Not only does NEST model the scintillation and charge yield in xenon, but it is also includes code that is used to generate accurate temporal profiles for S1 and S2 pulses, commonly referred to as “pulse shape”.

3.2.2.1 S1 Pulse Shape

As discussed in Section 2.1.3, the microphysics governing the S1 timing characteristics is an amalgamation of a triplet state decay, a singlet state decay, and the time associated with the recombination of ionization electrons, as well as the ratio of singlet to triplet states. In addition, effects due to detector geometry and signal processing add further modifications to the pulse shape. The NEST model, however, certainly does not include detector effects as

those are incorporated into a larger Geant4 model, in this case LUXSim. NEST includes as its values of the singlet and triplet lifetimes an experimentally determined error-weighted world average, determined by (3.10), and empirically determined values for the singlet to triplet ratios to simulate this aspect of the S1 pulse shape.

$$\bar{\tau} = \sum_i \left(\frac{\tau_i}{\sigma_i}\right) / \sum_i \left(\frac{1}{\sigma_i}\right) \tag{3.10}$$

$$\bar{\sigma} = \left[\sum_i \frac{1}{\sigma_i}\right]^{-1}. \tag{3.11}$$

Data from [57, 58, 63, 101, 102, 102, 103, 103, 104] are also in the NEST world average weighted by their respective errors. The singlet to triplet ratio model in NEST is simplified to ignore the dependence on electric field and dE/dx because experimental data are lacking in these regards. Table 2.1 lists the parameters that are included in the S1 NEST pulse shape model.

Since the recombination time is the dominant aspect of the S1 pulse shape produced by ER events, NEST includes a model of this effect as well. To first order, dE/dx is proportional to ionization density, so it follows that the recombination time is inversely proportional to the dE/dx [57]. Due to second order effects such as thermal diffusion and atomic line emission and absorption, the dE/dx is not directly proportional to ionization density, but the NEST framework does not include these effects because such second order effects were not needed for the model to explain observed scintillation yields [55]. Simply modeling the recombination time constant as inversely proportional to dE/dx, however, did not reproduce observations — the second-order effects are more important to this process. Hence, a sophisticated model motivated by the recombination probability (3.1) was instead developed. The recombination time is modeled as the inverse of the recombination probability:

$$\tau_{r,0} = \hat{\tau} \times \frac{1 + B\frac{dE}{dx}}{A\frac{dE}{dx}} \text{ ns}. \tag{3.12}$$

Here, $\hat{\tau}$ is a normalization factor, and no electric field is applied. However, the Onsager (C) is not included because it accounts for geminate recombination, a fast process with a negligible effect on the overall recombination time [55].

The normalization parameter $\hat{\tau}$ in (3.12) is applicable to ER, and it must be extracted from data. The standard practice is to fit a single exponential to the falling edge of the S1 pulse, a procedure that groups the singlet, triplet, and recombination time into one time parameter. It is also common to cite 45 ns [102] as the recombination time constant, but this time corresponds only to a 1 MeV electron, ignores the energy dependence of the recombination time, and is actually a single exponential fit encompassing all time constants and not the recombination time. The approach presented here leads to a more accurate, energy-dependent representation of the recombination time constant.

In the procedure to determine $\hat{\tau}$, the singlet and triplet lifetimes remain fixed per Table 2.1. Initially $\hat{\tau}$ is fixed and single-exponential fits are made to the falling edges of simulated S1 pulses as a function of energy. The extracted single exponential parameter is compared to data from [58], [103], and [105]. Next, $\hat{\tau}$ is varied and the process is repeated until the error between simulation and data is minimized. For ER events, a value of 3.5 ns was determined for $\hat{\tau}$. Figure 3.5 shows the decay time versus energy as derived from the single exponential fits. Various experimental data are also shown (see [106] for complete list). As is visible in the figure, the data do not agree with one another, so some choices were made. At high energies, data from Dawson *et al.* [58] were used in the minimization because it is an extensive and more recent measurement. At low energies, XMASS [105] was used because it is a more recent experiment, and hence has better xenon purity. The recombination time model describes the high energy points very well, but is somewhat higher than [105] data points. This is understandable because those points have larger errors.

The presence of an electric field exponentially quenches recombination. As the field gets stronger, electrons are more easily stripped away and are less likely to recombine. Therefore, as the applied electric field goes to infinity the number of ionization electrons available for recombination goes to zero [58], effectively stopping recombination. The triplet decay time constant then dominates the time structure of S1 pulse shape. The electric field dependence is found from an exponential fit to data [58], and (3.12) is expanded to,

$$\tau_r = \tau_{r,0} \times e^{-0.009 E_f}, \tag{3.13}$$

where E_f is the applied electric field in V/cm. Figure 3.6 shows the single exponential fit

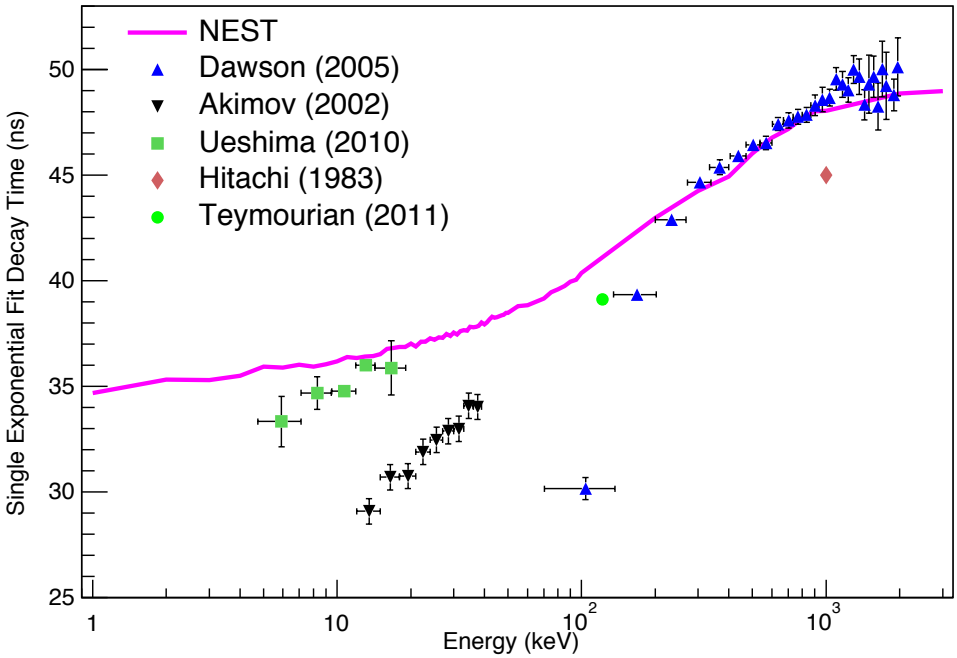

Figure 3.5. A comparison of the single exponential fit to the fall time of the S1 pulse at zero applied electric field for various data sets and NEST. The data were used to minimize the recombination time constant in the model.

to the fall time of the S1 pulse as electric field increases with (3.13) applied in the model along with the data from [58]. This is the only available data set with a non-zero field, and is at a fixed energy of 1.2 MeV gammas. Until more data become available, this model is applied at all energies.

The ratio of the number of singlet states to triplet states is different for direct excitation and recombination processes for electron recoils. These ratios are measured empirically and included in the model as 0.17 ± 0.5 for excitons and 0.8 ± 0.2 for recombining electrons [106].

Electron recoil events stemming from alpha interactions are treated differently in the model because they behave differently in the data. For alpha particles, the recombination time is zero because alphas have a high ionization density. The triplet lifetime will therefore dominate the pulse shape because it is longer than the singlet lifetime. An approximate fit to data from [58] and [101] yields a singlet to triplet ratio for direct excitation and

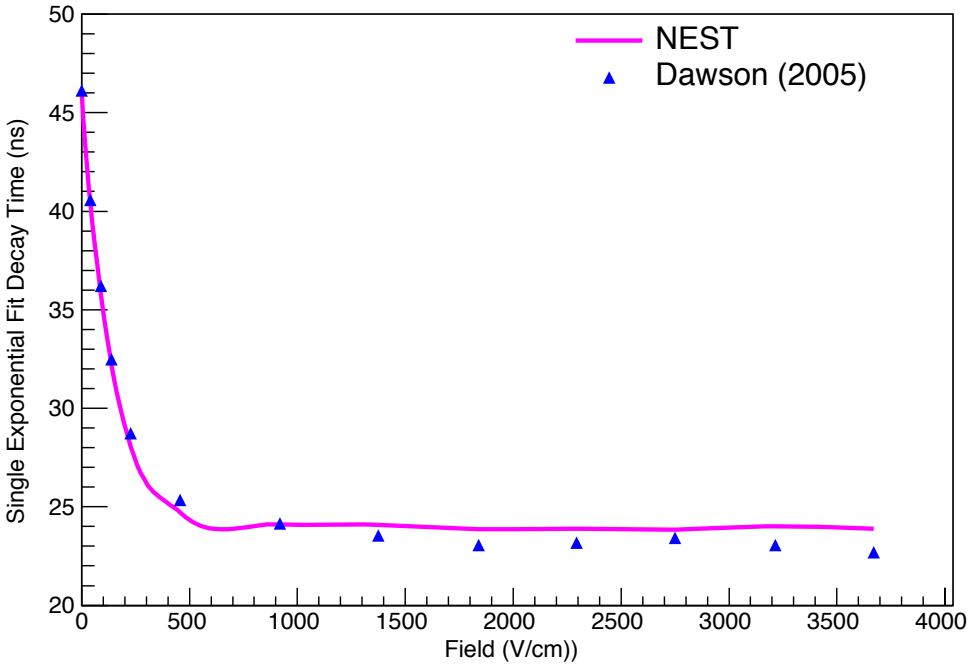

Figure 3.6. The electric field dependence of the single exponential fit to the fall time of the S1 pulse as the electric field increases for simulated 1.2 MeV gammas compared to similar data from [58]. This decay time is dominated by the recombination time constant which is modeled in this work.

recombination of 2.3 ± 0.51.

The case of nuclear recoils is different because the high density of ionization results in rapid recombination. NEST models this negligible recombination time as zero and the pulse shape is determined dominantly by the triplet time constant. Thus, the only parameter necessary to describe the time evolution of the pulse is the ratio of production of singlet and triplet states. This ratio has been measured to be 7.8 ± 1.5 for direct excitation and recombination [102, 103].

3.2.2.2 S2 Pulse Shape

As discussed in Section 2.1.4, the S2 pulse shape is defined by several physical effects. A model describing each is included in NEST. First, consider a model to calculate the mean free path of an electron to produce one S2 photon, rearranging (2.9) as

$$x = \frac{1}{N \times 10^{-17}} \left(0.140 \frac{E_e}{N} \times 10^{17} - 0.474 \right)^{-1} \tag{3.14}$$

where N is the number density of the gas in atoms/cm^3, E_e is the electric field in V/cm, and n_{ph}, the number of photons produced, has been fixed as 1. The normalization factor of 0.140 has been measured to be as much as 50% lower in some instances [59], and a possible explanation for this lies in poor gas purity. This normalization factor must carry units of photons/eV. When inverted, this is $\sim$ 7 eV/photon, which is the energy of the xenon scintillation photons [52]. It is conceivable, therefore, that this particular value suggests there is $\sim$ 100% efficiency in conversion of electrical energy from the field into scintillation photons. The value of x from 3.14 is stochastically applied in NEST, providing a novel approach for this calculation. This method is not as detailed as the microphysical approach of [107], but it is pragmatic in that it allows for fast and easy simulations that are empirically accurate.

As ionization electrons drift, they continuously collide with xenon atoms, reaching a terminal velocity. Several functions were considered to model the drift velocity, such as a sawtooth pattern. These more complicated formulations were deemed unnecessary in order to reproduce the data, and a simple, constant drift velocity was implemented. A large range of values of detector parameters was provided to the Magboltz package [108], and the resulting drift speeds were tabulated into a look-up table. This table is implemented as the electron drift model in NEST.

The scintillation process leading to an S2 signal contains a singlet and triplet decay component, similar to the S1 process. Unlike the case for liquid xenon discussed above, the need to separate the singlet and triplet times for direct excitation and recombination is not important for gaseous xenon, possibly because the drifting electrons are too low in energy to substantially ionize the medium. Further, as an ansatz for xenon, the model equates the singlet to triplet ratio in gas to that in liquid, an assumption that successfully reproduces the data. These two simplified time constants provide a coherent model of this aspect of the scintillation physics.

To model the diffusion as the electrons drift through the liquid to the gas, NEST creates a cloud of ionization electrons at the interaction site per the scintillation and charge yield models presented above. The diffusion widening of the cloud is computed and applied based

on (2.10). This resulting ellipsoidal electron cloud is then drifted to the gaseous xenon region, a process which includes loss of electrons due to impurities. The effective impurity concentration is provided by the user in terms of a mean absorption length. Once the simulated cloud reaches the liquid-gas interface, individual electrons are extracted according to their arrival time.

The electron extraction time for two-phase TPCs is modeled as an exponential distribution, where the characteristic time constant is derived from a quantum tunneling probability. Electrons drift to the liquid-gas interface where they must overcome the work function barrier, assisted by the extraction field. The emitted electron current density J (Am^{-2}) at the interface is given by the Richardson-Dushman equation and is related to the temperature, T and the work function W as $J = AT^2e^{-W/kT}$. Given the strength of the extraction field, the time for an electron to overcome the potential barrier can lead to delayed emission of electrons producing an S2. This time constant is referred to in NEST as the electron trapping time.

To study this effect and find the time parameter that best reproduces available data, a simplified model of the XENON10 detector [109] was built in Geant4. The parameters used in this toy simulation were: a) in liquid xenon, applied field was 0.73 kV/cm and the drift velocity was 1.89 mm/μs, b) in gas, the electric field was 12 kV/cm and the drift speed was 8 mm/μs [110]. S2 events were simulated as a function of drift for nuclear recoil energies in the 5-50 keV range, with the number of ionization electrons provided by NEST [55]. The number of photons per ionization electron in the gaseous region was determined by (3.14). A Gaussian was fit to each generated S2 pulse, and the width was compared to data [73]. The results of this study are shown in Figure 3.7. The red points are the XENON10 data, and the green points are derived from the toy model, with physically motivated values for the parameters mentioned in the previous paragraphs and no electron trapping time effect added. As can be clearly seen, this simulation produces S2 pulse widths that are systematically lower than the measurements. Subsequently, the electron trapping time was tuned as the only free parameter until the model best fit this data. The best-fit value was found to be 140 ns, which is comparable to the expected value of $\sim$100 ns

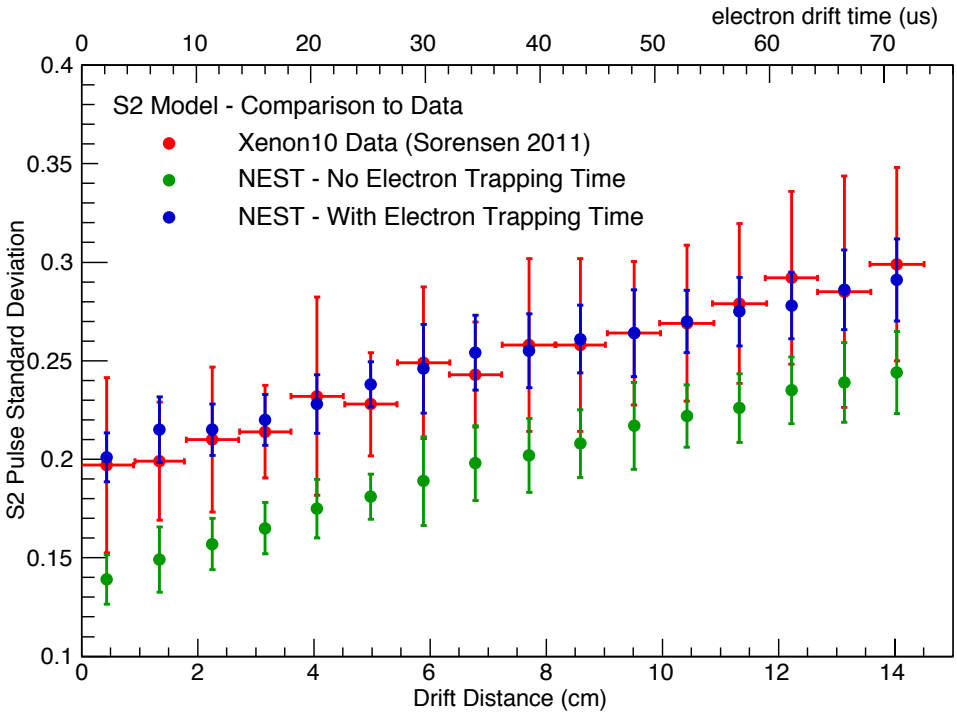

Figure 3.7. The fitted Gaussian width of an S2 pulse as a function of drift for data from XENON10 (red) [73] compared to a toy model of that detector incorporating the complete NEST model (blue). The error bars in the simulated work represent the width on the distribution of the Gaussian fit widths of the S2 pulses, due to the stochastic variation on the number of ionization electrons as provided by NEST. In the data, the error bars are a combination of this width as well as the uncertainty in the fit. The green points show the fitted width due to effects derived from first principles. Inclusion of the electron trapping time as a free parameter allows for excellent agreement between model and data.

[52]. Electrons are drifted through the liquid until they reach the phase transition surface. The electrons are emitted from the surface following an exponential distribution with the electron trapping time as the time constant. Figure 3.7, also shows the blue points, which are the simulated pulse widths after the electron trapping time is included. The addition of the electron trapping time as a free parameter is the only additional parameter added to the S2 physics described in Section 2.1.4 to produce an accurate representation of pulses.

In Figure 3.7, the error bars in the simulated work represent the width on the distribution of the Gaussian fit widths of the S2 pulses, due to the stochastic variation on the number of ionization electrons as provided by NEST. In the data, the error bars are caused by a combination of this width, the uncertainty in the fit, and the widths introduced by other

detector parameters such as data acquisition, PMT response, and analysis efforts. Because the data contains additional sources that act to broaden the pulse shapes, it is reasonable to assume the error bars will be larger than in the model which does not include these additional detector-specific effects. It should be noted that these detector-specific parameters should not affect the mean of the distribution, and this is clearly evident in the figure. The S2 width as it compares to drift distance is important in the search for low mass dark matter particles [111].

Using the same simplified model of the XENON10 detector described above, the effects of the components of the S2 pulse shape model are demonstrated in Figure 3.8. If only the ionization electron drift is modeled, the shape of the pulse is a square wave. Adding in the singlet and triplet lifetimes discussed in this section changes the pulse shape to one that resembles a shark fin [112]. The red curve shows the result of including the drift speed, the mean free path of an electron to produce a photon, and the singlet and triplet decay time constants in the model. Adding the effects of transverse and longitudinal diffusion in the gas (pink curve) and the transverse diffusion in the liquid (black curve) produces no noticeable change to the overall shape. The longitudinal diffusion in the liquid (green curve), however, produces a broadening of the shape. Because the drifting electron cloud is becoming elongated, the width increases and the height decreases, as the number of electrons (area of the pulse) remains constant. Finally, the electron trapping time parameter adds the asymmetry expected in the S2 and leads to the final simulated pulse shape.

3.2.3 Detector Response

LUXSim, incorporating the NEST models, is a powerful tool to study the effects of the detector, but at this point the recorded results are the number of S1 photons produced and the number of S2 photons produced, tracked until either propagating to a PMT or lost to efficiency. Converting these raw numbers of quanta into actual detector signals requires additional software, which simulates the analog electronics and digitizers, referred to as the simulated detector response.

The simulated detector response must read in the quanta information from NEST and LUXSim and write out a file in the standard LUX event format [113]. First, the simulated

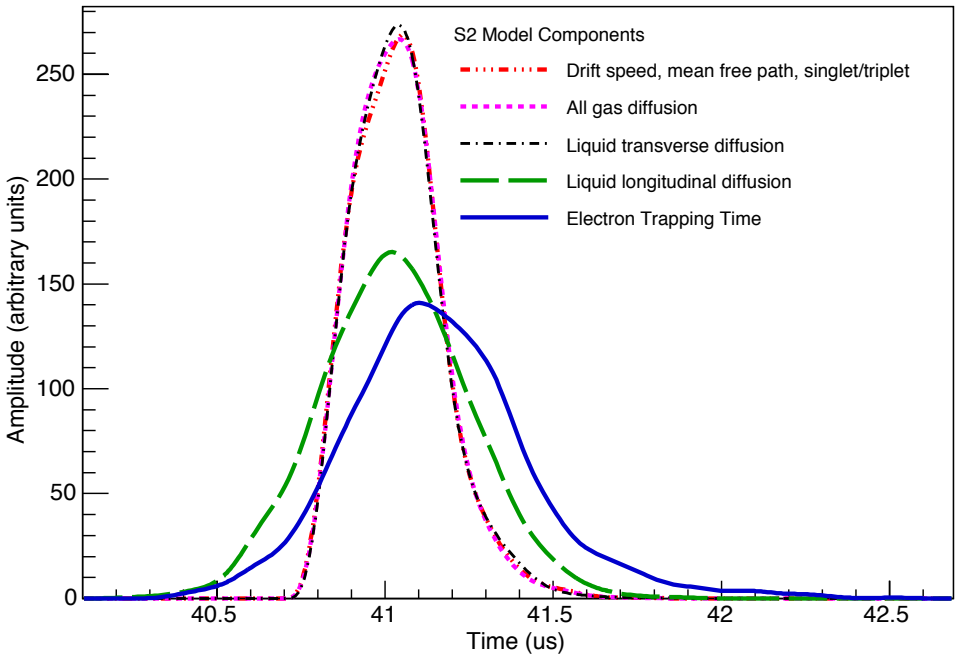

Figure 3.8. The resulting S2 pulse shape as additional model parameters are included in the simulation. The red curve shows the result of including the drift speed, the mean free path of an electron to produce a photon, and the singlet and triplet decay time constants in the model. Adding the effects of transverse and longitudinal diffusion in the gas (pink curve) and the transverse diffusion in the liquid (black curve) produces no noticeable change to the overall shape. The longitudinal diffusion in the liquid (green curve), however, produces a shift in the shape. Finally, the electron trapping time parameter adds the asymmetry expected in the S2 and leads to the final simulated pulse shape (blue curve).

detector response reads in the time a photon arrives at a particular PMT. Based on the quantum efficiency of that PMT, the scintillation photon may be converted to a photoelectron. Next, a voltage response is generated for each photoelectron, and these voltage traces are superposed and summed to define a a final pulse. The waveforms are sampled in time and height with an algorithm that contains identical parameters as the analog and digital electronics used in the experiment. Finally, the results are written to an output file that can be analyzed by the same software used to process output from the detector data acquisition system. Figure 3.9 shows graphically the process of digitizing simulation output.

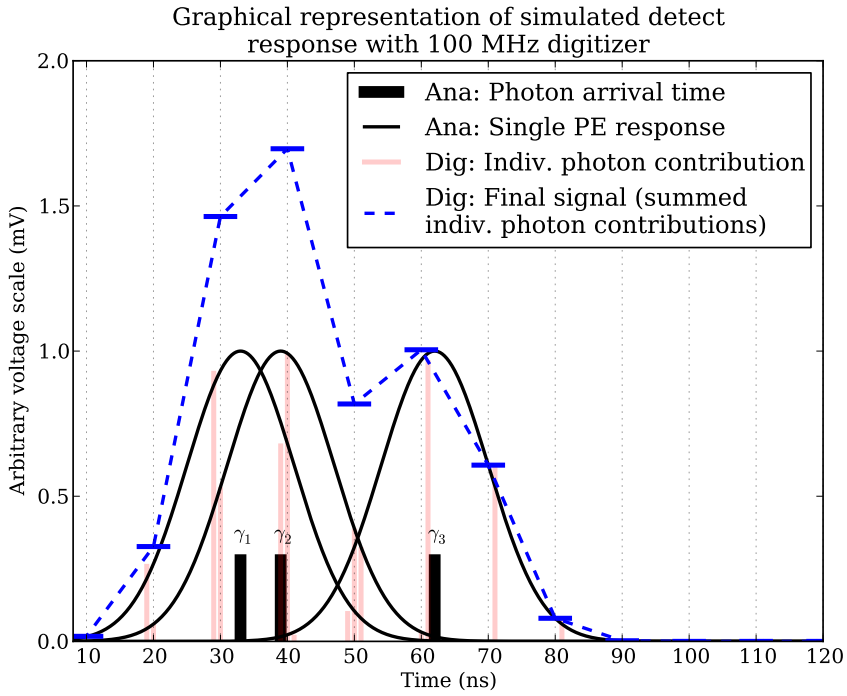

Figure 3.9. Graphical representation of simulated detector response waveform digitization. The order of operations is represented by the order of items in the legend. Analog signals are prefixed with Ana, and digital signals with Dig. Figure from [113]

3.3 Comparison of LUXSim to Data

The validity of the simulation must be verified in order to have confidence in the background model, which will be discussed in Chapter 4. Presented here are key examples of comparisons between the predictions of a complete simulation and the corresponding physical processes observed in data.

Simulations of ^{83m}Kr Injection

As xenon detectors become ever larger, external calibration sources become decreasingly useful because the xenon self shielding prevents gamma sources from penetrating deep into the fiducial volume of the detector. An internal calibration source is ideal, and LUX uses two different internal calibration sources, discussed in detail in Chapter 5. One such source is ^{83m}Kr which has half life of 1.83 hours and decays by emitting 32.1 keV and 9.4 keV gammas with a lifetime of 160 ns. The LUXSim krypton generator is used to provide a simulation of the response of LUX to this source. Figure 3.10 shows a simulated ^{83m}Kr waveform. Notice

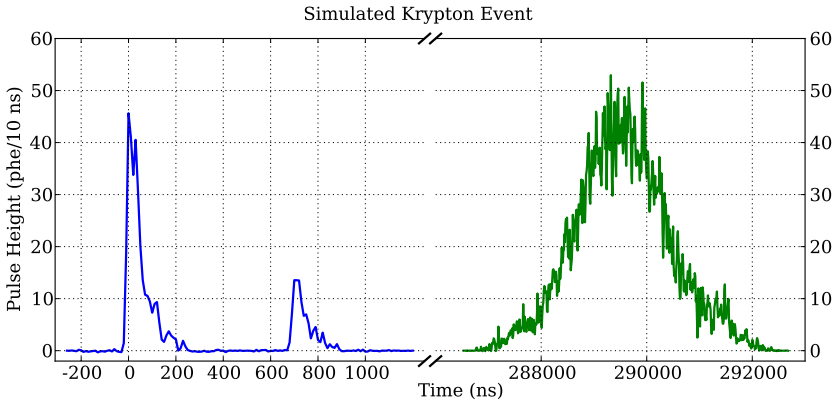

Figure 3.10. The two S1s followed by a single S2 are clearly observed. The first S1 is a result of the 32.1 keV gamma and the second S1 the 9.4 keV gamma. Figure from [113].

the separation of the multiple S1s. Such separation would not be realized based on Geant4 simulations only, without the LUXSim and NEST extensions.

Simulations of Low Energy Electron Recoils

As a final comparison between LUXSim and LUX data, consider a generic ER (gamma or electron) event that has 4.8 keV_{ee} of deposited energy. Simulating such an event and comparing the generated waveform to an event in the detector yields nearly identical pulse shapes. Figure 3.11 shows this comparison, demonstrating the accuracy of the NEST S1 and S2 pulse shape models. Note that this is intended as an illustration of the power of the simulation, as not every simulated event will match as well with the data. The small difference in the S2 width is due to a fluctuation in the area of the S2 as it relates to the energy scale.

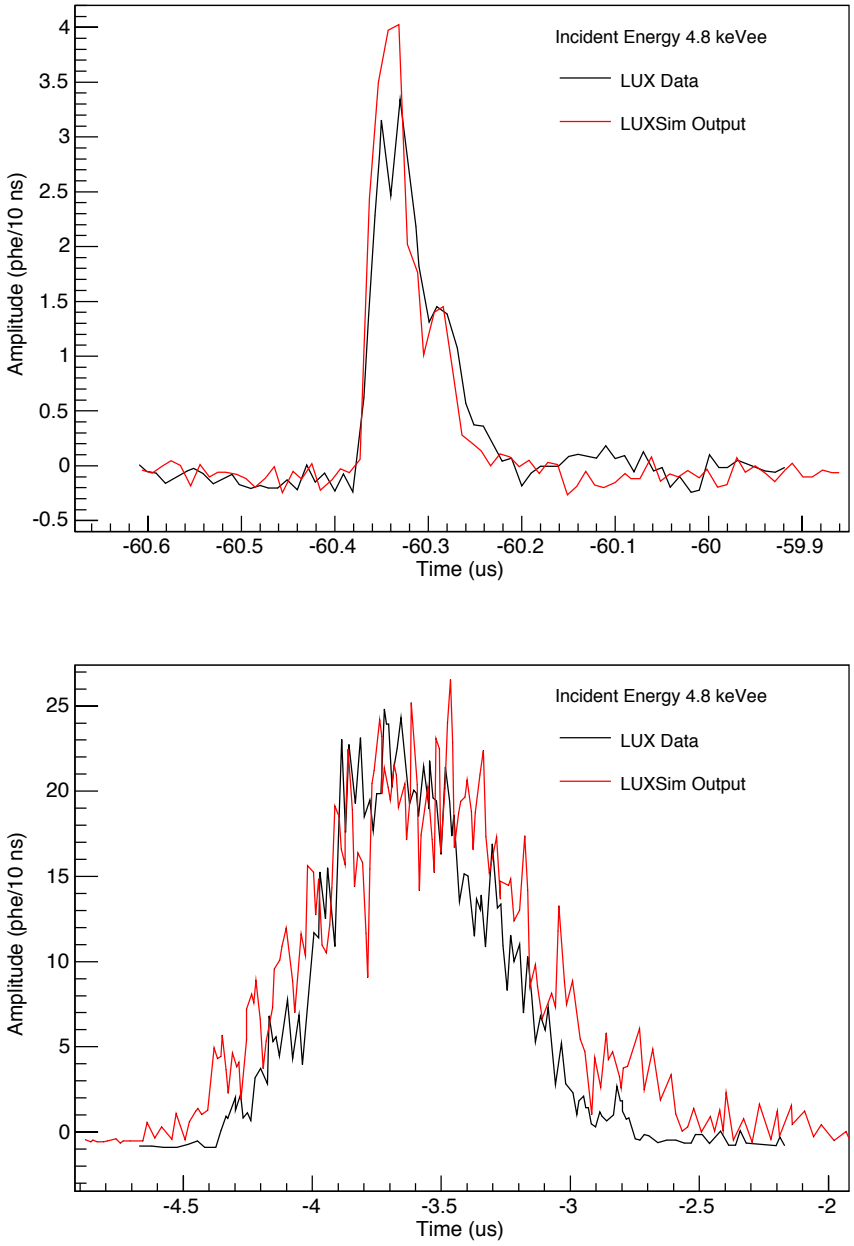

Figure 3.11. A comparison of the pulse shape of a simulated 4.8 keV_{ee} ER event and a similar event in the data. The top panel shows the S1 and the bottom the S2. The small difference between the width of the simulated S2 and the data S2 is due to a fluctuation in the energy calibration.

Chapter 4

Background Model

LUX, as a generic particle detector, is sensitive to any particle that scatters within its target volume, which makes it inherently useful as a device to search for new physics. At the same time, this sensitivity makes it difficult to carry out certain searches because any interactions beyond those of interest can dwarf the signal. In order for LUX to search for the rare process of WIMP dark matter scattering off a target nucleus, the background events, caused by interactions between the target and particles that are not WIMPs, must be minimized. Neutron backgrounds especially must be minimized as neutron scatters have a similar interaction signature to that of WIMPs. Discrimination between ER and NR allows for powerful background (ER) rejection, but potential leakage from the ER band to the NR band requires that ER backgrounds be minimized as well. This leakage is discussed in Chapter 5. The high density of liquid xenon ensures that ER background events, due to external γ-rays, occur near the edge of the target. This allows for the creation of a central fiducial volume, which is free from most ER background events. In this chapter, the various background sources and associated rates are discussed.

4.1 Radiation from Uranium and Thorium Decay Chains

Before discussing the sources of background for LUX, consider the following discussion of decay chains. All materials contain trace impurity levels, including some number of radioactive nuclei which will decay with a characteristic half-life. Most radioactive isotopes do not decay directly to stable states but rather go through several stages of decay until a stable

isotope is reached, a progression referred to as a decay chain [50]. The intermediate states between the parent and the stable isotopes are referred to as daughters. In such a decay chain, if the half-life of the parent isotope is very long compared to that of the daughters, the decay and production rates of each daughter nucleus will be in equilibrium. The decays occurring at the various stages will emit α, β, or γ particles at a constant rate. These particles can interact in the LUX detector as background events. Two such decays chains, ^{238}U and ^{232}Th, can present large backgrounds in LUX. ^{238}U has a half-life of 4.5 billion years while ^{232}Th has a half-life of 14 billion years, and they both exist in nearly all materials at some level. The complete chains, shown in Figure 4.1, demonstrate that many radioactive stages exist until a final stable state is reached.

The thorium series [50], beginning with ^{232}Th, contains radioactive isotopes of actinium, bismuth, lead, polonium, radium, and radon. The series concludes at ^{208}Pb. The uranium series [50] begins with ^{238}U and contains radioactive isotopes of astatine, bismuth, lead, polonium, protactinium, radium, radon, thallium, and thorium. It terminates with ^{206}Pb. The ^{222}Rn in the uranium series is unlike the other daughters in that it exists with a longer half-life than the other radon isotopes. Since it exists in a gaseous state, it can become airborne and adhere to a material, decay, and plate the material with ^{210}Pb, which has a half-life of 22 years. ^{210}Pb decays via α emission [50], which can pose problems as described below. Because of this, the amount of radon that various detector materials are exposed to should be reduced, by, for example, maintaining materials in a pure nitrogen purge during construction. Radon suppression was not carefully undertaken during the construction of LUX.

Figure 4.1, which shows the uranium series and the thorium series, also indicates what type of decay is associated with each stage. Downward facing arrows indicate α decays while upward facing arrows indicate β decays. Since γ decay does not change the nucleus, only its state, those type of decays are not directly visible on this figure. Most α and β decays, however, result in daughter nuclei that exist in excited nuclear states which must de-excite to their ground states via γ emission.

When β or γ particles are emitted, they can produce ER events (γ's undergo Compton

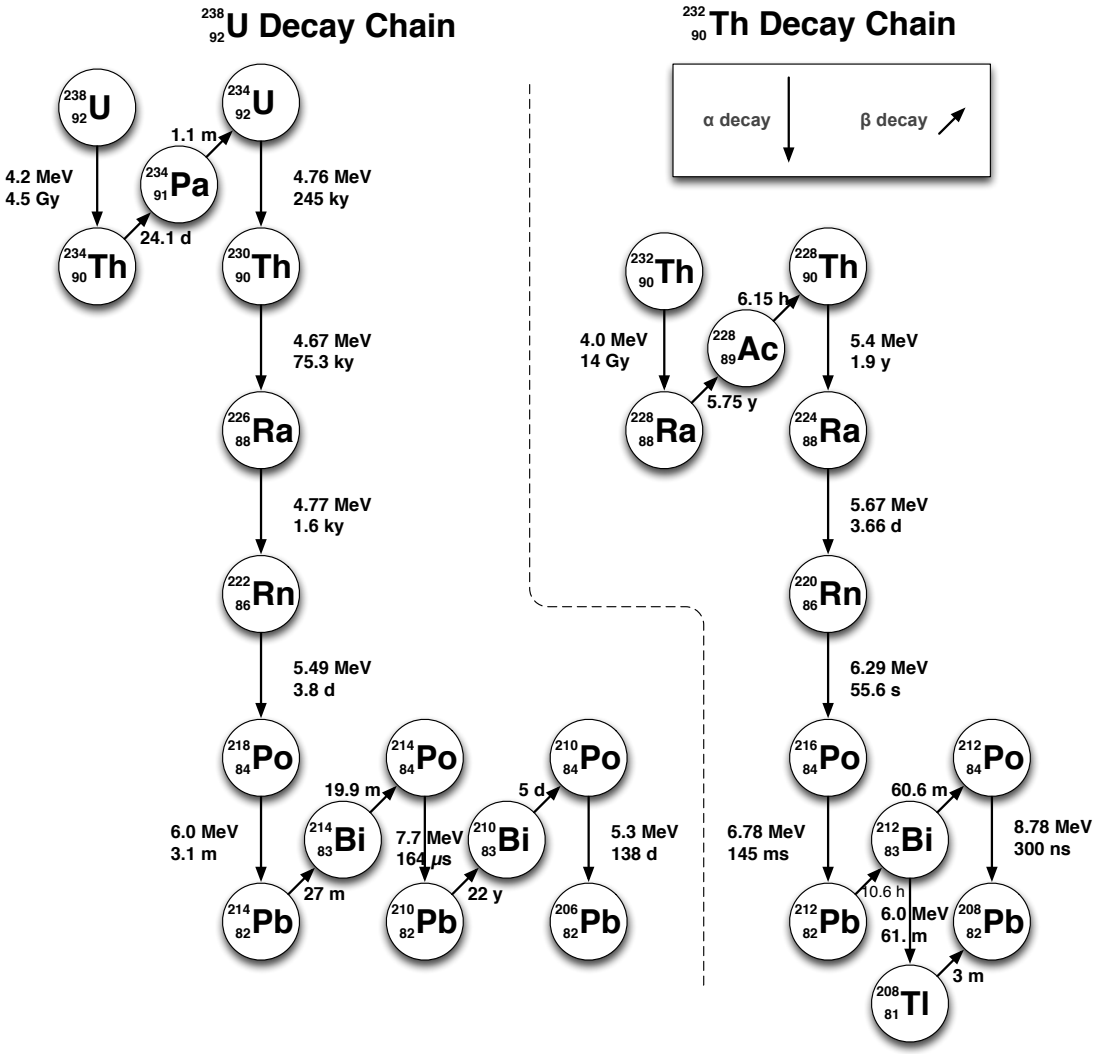

Figure 4.1. The uranium-238 and thorium-232 decay series. Each stage represents a radioactive nuclei that decays and emits α, β, or γ particles. These particles can interact in LUX and contribute to the background rate observed. Figure from [113].

scattering with atomic electrons) in LUX which can leak into the WIMP search region. An α particle incident on a low-Z material can cause fission or an (α, n) reaction resulting in the ejection of one or more neutrons [50]. The resulting neutron can interact in the target and mimic a WIMP signature. The teflon and high density polyethylene material surrounding the target provide a copious amount of such low-Z material in close proximity to the fiducial volume [114]. In the following sections, background sources are discussed beginning from the outside and working in towards the center of the detector.

4.2 Backgrounds from External Sources

The interaction of cosmic rays in LUX can contribute to the ER background rate. At sea level, the muon flux resulting from cosmic rays is approximately 2×10^{-2} s^{-1}cm^{-2} [12]. ER interactions at that high a rate would dwarf the signal from WIMP detection. To shield LUX from cosmic muons, the detector is operated at a depth of 4300 m.w.e. which stops all but the highest energy muons. The simulated flux of muons at this depth is 4.4×10^{-9} cm^{-2}s^{-1} [79], representing a reduction in flux of 7 orders of magnitude. The LUX detector is placed in the center of a 76,000 gallon (300 tonne) water tank which acts as a shield against the surviving cosmic rays and other external backgrounds. Additional discussion of the water shield is located in Chapter 2.

A high energy cosmic muon that penetrates to that depth can induce a neutron background from spallation in the rock with a predicted NR background rate of 60×10^{-9} counts/kg/keV$_{nr}$/day in the fiducial volume and WIMP search range (defined in Chapter 7). Muon-induced neutron production can also happen via a the same process in the water. The predicted rate of these backgrounds is $\times 2$ larger than those induced in the rock. The total expected NR background rate due to muon-induced high energy neutrons is thus 0.1 event in the fiducial volume in the WIMP energy search range in one year [115].

The external γ background is dominated by the decays of ^{40}K (half-life of 1.2 billion years) and the uranium and thorium chains present in the cavern rock. Careful screening of rock samples indicates that the majority of the rock material surrounding the underground laboratory contains impurities at the following levels: 0.160 ppm ^{238}U, 0.200 ppm ^{232}Th,

and 1540 ppm ^{40}K [116]. There are rhyolite intrusions in the rock with much higher activity levels: 8.6 ppm ^{238}U, 10.8 ppm ^{232}Th, and 2.9×10^4 ppm ^{40}K. Because the exact distribution of rhyolite intrusions in the rock is not known, the conservative assumption that all rock surrounding the cavern contains the rhyolite radio-impurity levels is made. A LUXSim model of the cavern indicates a reduction in the external γ-ray flux by a factor of 2×10^{-10} due to the water shield, resulting in 27×10^{-9} counts/kg/keV$_{ee}$/day of ER background events in the active xenon volume [115]. Hence, it is expected that these external sources will not contribute any ER events in a 100 day run of LUX.

The external neutron background is dominated by the fast neutrons produced in radioactive decays in the surrounding rock, produced mainly by ^{238}U spontaneous fissions, (α, n) neutrons generated by α decays in the ^{238}U, and ^{232}Th series decays. Assuming the rhyolite radio-impurity levels as a conservative measure, the estimated neutron flux incident on the water shield is 1.6×10^{-10} neutrons/cm^2/s. The water shield reduces this flux by a factor of 6×10^{-22}, leading to the prediction of 10^{-16} neutrons/year incident on the active volume [115].

The large reduction factors on the γ-ray and neutron fluxes resulting from the absorption in the water shield renders the external background sources as subdominant to the internal background sources discussed below. However, these sources are included in LUXSim to ensure the completeness of the background model.

4.3 Backgrounds from Material Radioactivity

As discussed above, all materials have intrinsic impurities embedded within them. As rare event search experiments such as LUX improve their suppression of external backgrounds, they become increasingly sensitive to internal radio-impurities. Thus, it is necessary to measure the amount of radioactive impurities contained within all materials used to build the detector.

The material screening program for LUX consisted of a low background γ-ray assay carried out for a sample of each type of construction material. High purity germanium detectors, located at the Soudan Low-Background Counting Facility (SOLO) [117] and the

Berkeley Oroville Facility were used to screen the materials. The SOLO facility is located at the Soudan Underground Laboratory with 2000 m.w.e of rock overburden, and the Berkeley Oroville Facility is located under the Oroville Dam in northern California with 180 m.w.e. overburden. This shielding allows for high-sensitivity measurements for each material sample. Overall, > 75 materials were screened through the course of detector construction [115].

The screening results are reported for the ^{232}Th and ^{238}U isotopes. For some materials that contain a significant amount of ^{40}K of ^{60}Co, those values are reported as well. The PMTs, the PTFE surrounding the active region, the copper of the internal and intermediate structures, and the titanium cryostat vessels combined account for $> 95\%$ of the detector mass. The rest of the materials, while all assayed, account each for < 1 kg of material. The dominant source of background stemming from materials will be from these high mass objects, and their radio-impurity levels are listed in Table 4.1.

Because the LUX detector was operated on the surface for two years during construction and initial proof-of-concept operation, detector material components were activated cosmogenically. Only the titanium of the cryostats and the copper internals have activation by-products that could produce measurable ER backgrounds. This activation ceased upon transport of the detector from the surface to the underground.

The titanium vessels were selected from low-background stock [80]. Titanium activates via the fast neutron (n,p) interaction, whereby a high energy neutron, most likely from spallation, interacts with and replaces a proton in the nucleus. Isotopes of titanium then activate to isotopes of scandium. The isotope of most concern is ^{46}Sc, as it has an 84 day half-life and decay mode that produces two simultaneous γ-rays with energies 889 keV and 1121 keV, both of which can generate a WIMP search ER background [50]. To estimate the total amount of ^{46}Sc produced, a sample of titanium was taken underground for two years and then screened at SOLO to establish a baseline. Then it was transported to the surface and activated for six months before taken back underground for a re-analysis at SOLO, indicating a rate of 4.4 ± 0.3 mBq/kg of ^{46}Sc. Based on this, the estimated total ^{46}Sc rate in the detector cryostats immediately upon underground arrival was 1.3 Bq [115]. Between

Component	Amount Used	^{238}U	^{226}Ra	^{232}Th	^{40}K	^{60}Co
PMTs	122 PMTs	<22	9.5±0.6	2.7±0.3	66±6	2.6±0.2
PMT bases	122 bases	1.0±0.4	1.4±0.2	0.13±0.01	1.2±0.4	<0.03
Inner field ring supports (HDPE)	18.0 kg		<0.5	<0.35		
Outer field ring supports (HDPE)	15.5 kg		<6.3	<3.1		
Main reflector panels (PTFE)	15.5 kg		<3	<1		
Cryostats (Ti)	231 kg	4.9±1.2	<0.37	<0.8	<1.6	4.4±0.3 (^{46}Sc)
Grids (stainless steel)	4.5 kg		1.4 ± 0.1	0.23 ± 0.07	<0.4	1.4 ± 0.1
Field shaping rings (Cu)	28 kg		<0.5	<0.8		<0.3
PMT mounts (Cu)	169 kg		<2.2	<2.9		<1.7

Table 4.1. γ radio-assay data for high-mass LUX detector construction material samples. The ^{238}U column lists measurements that are performed on γ ray lines from isotopes in the ^{238}U early sub-chain, defined as all isotopes above ^{226}Ra in the ^{238}U decay chain. This measurement yields large errors and upper limits due to the very low branching ratios of these γ rays, but provide the most direct measurement of ^{238}U content. Measurements listed in the ^{226}Ra column are performed on γ ray lines from the ^{226}Ra sub-chain, defined as isotopes including and below ^{226}Ra in the ^{238}U chain. The corresponding γ rays have much higher intensities than those from the ^{238}U early sub-chain, and yield correspondingly lower activity limits. Radium-226 measurements are the typical results reported from LUX counting to determine ^{238}U contamination. Both measurements are included for completeness (where available). Reported errors are statistical only. Upper limits are at 90% CL. Table reproduced from [115].

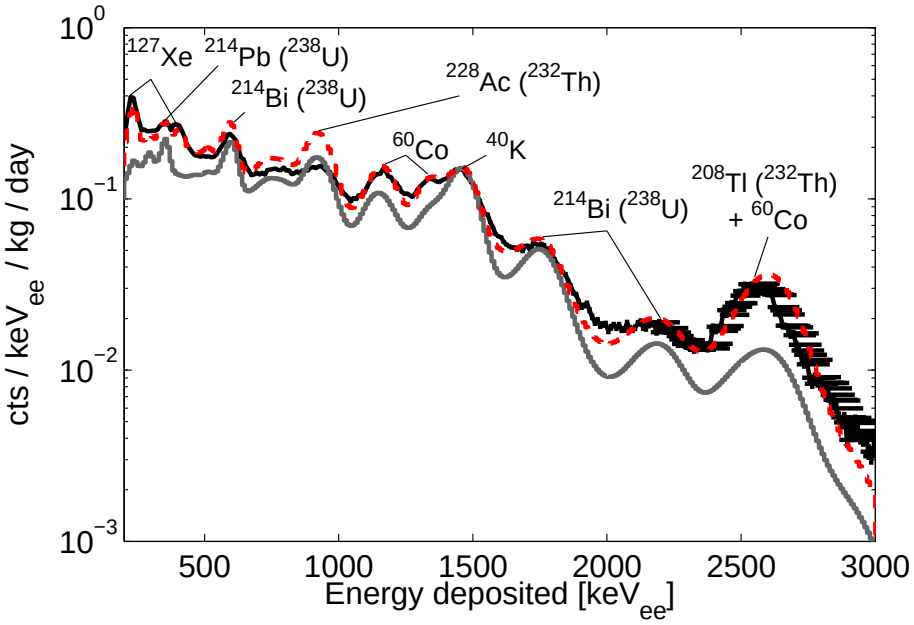

Figure 4.2. Measured γ-ray spectrum in LUX active volume with peaks identified is shown in black. A 225 kg target volume is chosen, with 2 cm removed from the top and bottom of the liquid to remove regions with irregular electric fields. Two simulated spectra are shown. The grey line is a spectrum based on positive-counting measurements alone. The red line is a spectrum with best-fit scaling for ^{232}Th, ^{238}U, ^{40}K and ^{60}Co decays. Figure from [115].

underground arrival and the start of the WIMP search, 284 days passed, allowing the ^{46}Sc to decay such that no discernible ^{46}Sc signature was present in the WIMP search data [115]. Cosmogenic activation of copper can produce ^{60}Co, which has a half-life of 5.3 years and generates γ's with energy 1.1 MeV and 1.3 MeV [50]. These can produce ER backgrounds in the WIMP search data. The estimated production rate of ^{60}Co in LUX copper at the time of arrival underground is 210 ± 10 counts/kg/day, and, after accounting for the 800 day surface exposure, an estimated decay rate of 1.0 ± 0.5 mBq/kg [115].

The results from the material screening program and cosmogenic activation estimates were incorporated into LUXSim so that a comprehensive background model could be developed. The simulated spectra were compared with measurements to refine the estimated quantities of ^{232}Th, ^{238}U, ^{40}K and ^{60}Co in the detector internals. The decay rate of each isotope was varied independently to obtain the best fit to the measured γ-ray spectrum in the target. Figure 4.2 shows the measured spectrum in black. To ensure minimal effects due

Isotope	Screening Estimate (Bq)	Best Fit (Bq)
^{238}U	0.58 ± 0.04	0.62 ± 0.16
^{232}Th	0.16 ± 0.02	0.23 ± 0.06
^{40}K	4.0 ± 0.4	3.8 ± 1.0
^{60}Co	0.16 ± 0.01	0.22 ± 0.06

Table 4.2. Screening estimate and best-fit activity values for radioisotopes modeled in high-energy γ ray analysis. Screening estimate values are taken from direct counting results. Materials with upper limits are not incorporated into the initial estimate. Errors on the best fit values are estimated to be 25%. Table reproduced from [115].

to irregularities in electric field, 2 cm was removed from the top and bottom drift regions, causing the fiducial volume to have mass of 225 kg. Two simulated spectra are considered, shown in Figure 4.2. The grey line is a spectrum based solely on direct-counting measurements. The red line is a spectrum where the decay rates were allowed to vary by a scale factor such that the best-fit values for ^{232}Th, ^{238}U, ^{40}K and ^{60}Co were achieved. The screened and fit rates are listed in Table 4.2.

As evident in Figure 4.2, the best-fit simulation peak sizes show good agreement with the data with the exception of the excess in the ^{228}Ac 969 keV line, a product of the thorium series. Scaling the activity of the thorium series can bring this line into agreement at the expense of introducing disagreements in other peaks in the chain. The deficit of observed ^{228}Ac perhaps suggests that some amount of ^{228}Ra escaped from the materials during construction, though a detailed isotope concentration model was not investigated since this deficit does not affect the ER or NR background rate in the WIMP search energy range [115]. Figure 4.3 shows the expected ER background density in the WIMP search energy range for material and external sources as a function of position with the best-fit scaling values for each background isotope.

The intrinsic radioactive backgrounds in the LUX construction materials can contribute neutron (NR) backgrounds as well. A single scatter neutron background event in LUX could mimic a WIMP signal and cast doubt on any discovery or sensitivity limit, so great care was taken to understand the potential neutron background rate. The dominant source of neu-

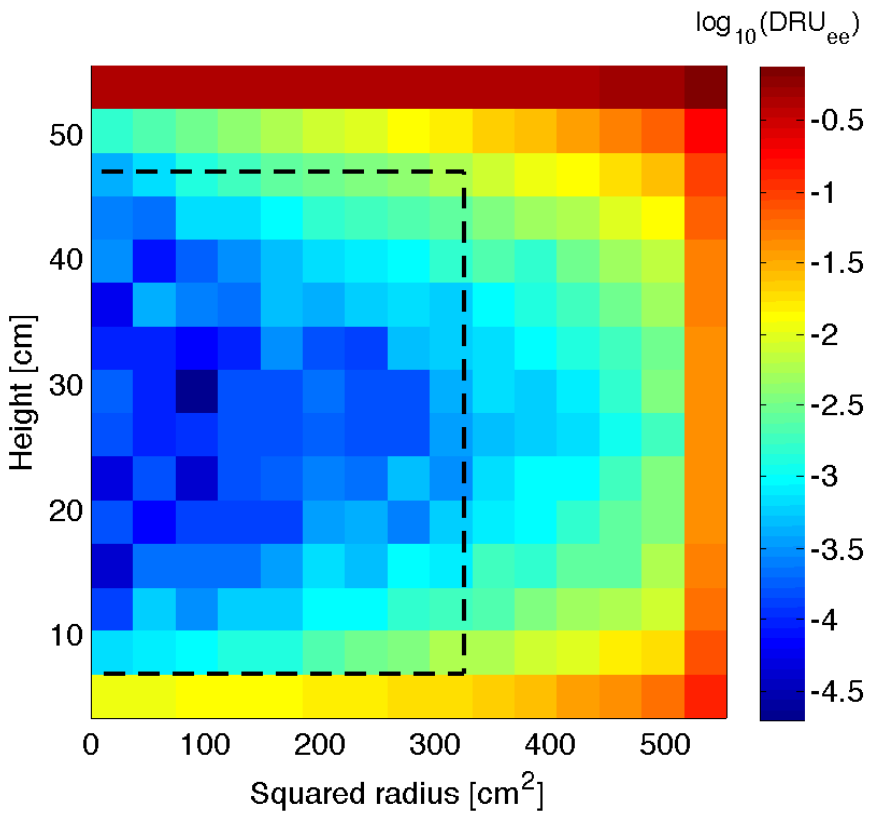

Figure 4.3. LUX γ-ray ER background density in WIMP search energy range from material and external backgrounds as a function of position based on LUXSim prediction from. The WIMP search fiducial volume is overlaid in black lines for comparison. Note the extremely low background rate observed in the fiducial volume. One differential rate unit (DRU_{ee}) = counts/keV$_{ee}$/kg/day. Figure from [115].

tron backgrounds in LUX is the ^{232}Th and ^{238}U series concentrations in the LUX PMTs [117]. The ^{232}Th and ^{238}U content in the rest of the materials contributes less than half that of the PMTs, rendering these other materials entirely subdominant [115]. The (α,n) neutron spectrum from the PMTs was calculated with the Neutron Yield Tool [118, 119]. This tool predicts the neutron rate from the PMTs from (α,n) and spontaneous fission to be 1.2 neutrons/PMT/year. Incorporating these values into LUXSim and applying a single scatter neutron cut predicts a total number of neutron events in the WIMP search energy range over the full timescale of the search in the fiducial volume to be 0.06 [115]. Thus, the ability to distinguish between single and multiple scatter events drastically reduces the neutron background rate.

4.4 Backgrounds from Internal Isotropic Sources

Thus far the discussion has been focused on backgrounds that are both external and internal to LUX, but contained in materials surrounding the active region. The external shielding, careful material selection, and self-shielding properties of xenon largely render these backgrounds as subdominant (see Figure 4.3). Now follows a discussion of backgrounds that are isotropically distributed within the target volume itself.

4.4.1 Cosmogenically Activated Xenon

Xenon has six stable isotopes: ^{126}Xe, ^{128}Xe, ^{129}Xe, ^{130}Xe, ^{131}Xe, ^{132}Xe. Thermal neutron capture can activate ^{126}Xe and ^{132}Xe to unstable isotopes ^{127}Xe and ^{133}Xe, with half-lives of 36 and 5.3 days, respectively. Additionally, ^{129}Xe and ^{131}Xe can activate to metastable isotopes ^{129m}Xe and ^{131m}Xe with half-lives of 8.9 and 12 days, respectively. Each of the radioactive isotopes will decay, and potentially produce ER background events. The activation is driven cosmogenically while the xenon is on the surface. Upon transportation from the surface to the underground, the cosmogenic activation ceases, and given enough time the radioactive isotopes decay away.

Signatures from all four radioactive isotopes were identified in data after the start of underground operations, before the start of the WIMP search. The energy spectrum of these isotopes, taken 12 days after the xenon was transported underground, is shown in Figure 4.4. A simulation spectrum was fit to the data to estimate the rates, and these results are tabulated in Table 4.3. The decays of the longer lived isotopes, ^{127}Xe and ^{131m}Xe, were tracked over the course of the WIMP search. Figure 4.5 shows the rate of each isotope plotted against the day of the measurement. An exponential was fit to the distribution, with the slope fixed per the half-life for each isotope listed in Table 4.3. These fits yield concentrations of 115 ± 20 μBq/kg for ^{127}Xe and 7.3 ± 1.5 μBq/kg for ^{131m}Xe, averaged over the the second half of the WIMP search [115]. The estimated background rate in the fiducial volume, based on LUXsim studies, is 0.50 ± 0.02 mBq/kg/keV$_{ee}$/day, averaged over the entire WIMP search [115].

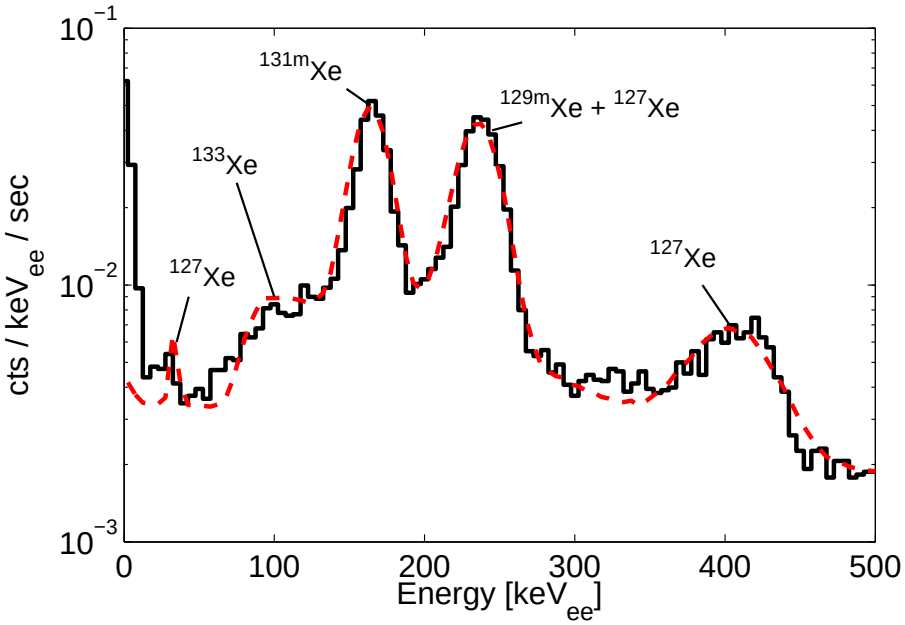

Figure 4.4. Early, pre-WIMP search data from LUX taken 12 days after the xenon was transported underground. The measured spectrum is shown in black, and the best-fit spectrum is shown in red. All four activation signatures are visible, and the best-fit rates are tabulated in Table 4.3. Figure from [115].

Isotope	Half-Life	Emitted γ Energy	Best-Fit Decay Rate
^{127}Xe	36 d	375 keV$_{ee}$	2.7 ± 0.5 mBq/kg
^{129m}Xe	8.9 d	197 keV$_{ee}$	3.6 ± 0.7 mBq/kg
^{131m}Xe	12 d	164 keV$_{ee}$	4.4 ± 0.9 mBq/kg
^{133}Xe	5.3 d	81 keV$_{ee}$	3.6 ± 0.7 mBq/kg

Table 4.3. The isotope, half-life, and best-fit rate of the four activated xenon isotopes observed in LUX data 12 days after transporting the xenon underground. Best-fit data from [115]. γ energies from [50].

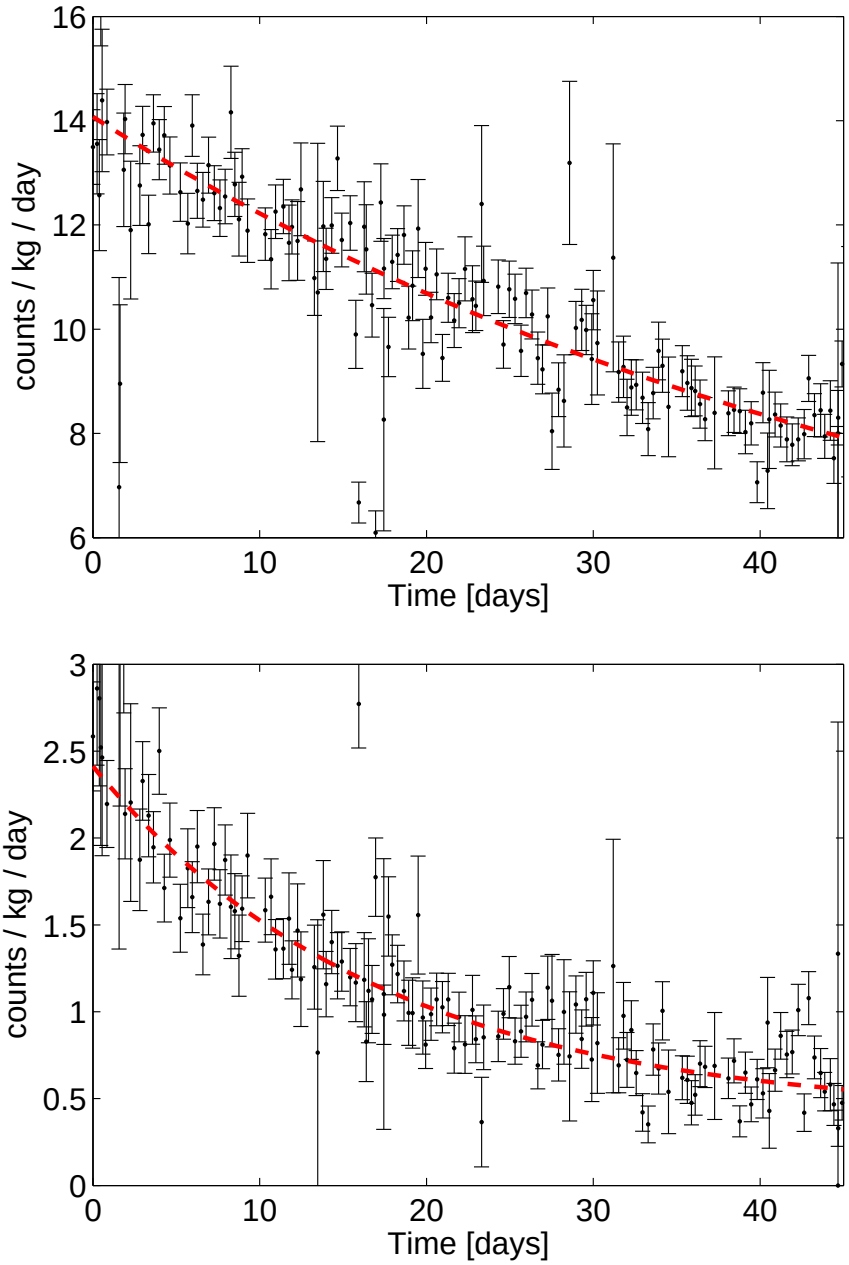

Figure 4.5. Activated xenon rates as a function of time. The *top* panel shows ^{127}Xe and the *bottom* panel shows ^{131m}Xe. The red line shows the best-fit exponential, assuming slope that of the half-life of each isotope as given in Table 4.3. Error bars are statistical. Figure from [115]

.

Decay Chain	Isotope (MeV)	Energy (MeV)	Measured energy	Half-life (mHz)	Event Rate
^{238}U	^{222}Rn	5.59	5.59	3.8 d	17.9 ± 0.2
	^{218}Po	6.16	6.12 ± 0.10	3.1 m	14.4 ± 0.2
	^{214}Po	7.84	7.80 ± 0.2	160 μs	3.5 ± 0.1
	^{210}Po	5.30	5.22 ± 0.09	140 d	14.3 ± 0.2
^{232}Th	^{220}Rn	6.41	6.47 ± 0.09	56 s	2.6 ± 0.1
	^{216}Po	6.91	6.95 ± 0.1	0.15 s	2.8 ± 0.1
	^{212}Bi	6.21	6.12 ± 0.1	61 m	14.4 ± 0.2

Table 4.4. Radon chain daughter isotopes measured in LUX during the WIMP search. Note that the α energy scale was set by the 5.59 MeV ^{222}Rn peak, so the measured energy of this peak is forced to be 5.59 MeV. Table reproduced from Table 5 in [115].

4.4.1.1 Radon

The decay of ^{222}Rn and ^{220}Rn daughters can produce low-energy ER background events in LUX. Radon daughters are identified by their α decays, which are typically in several MeV range. In LUX they produce a characteristically large S1 signal, much larger than the S1 signal generated by any γ-induced ER event. The only source of α signatures in LUX, in fact, comes from ^{222}Rn and ^{220}Rn, and their daughters, so the observation of such events provides a direct way to measure the radon concentrations [115]. There are also α decays from ^{210}Pb which was plated on to detector materials from Rn decays during construction. These tend to be on the periphery of the Xe volume, and are left out from this discussion of isotropic backgrounds.

Figure 4.6 shows the identified α's and their corresponding identifications (black), as well as functional fits to the peaks (colors). The functional fits were used to compute the total daughter rates. The radon daughter isotopes, energies, half-lives, and measured decay rates are shown in Table 4.4 [115]. The reconstructed energies of the α's are assumed to be the Q-values of the decays, which accounts for the α particle and the recoiling daughter nucleus [115].

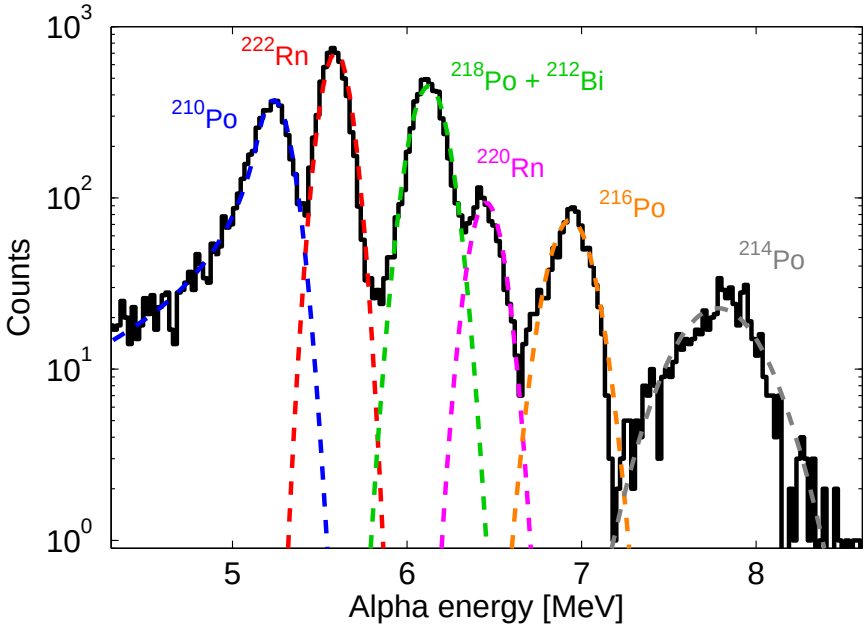

Figure 4.6. Signatures of α particles in LUX in the active volume during the WIMP search. Energy reconstruction is from S1 measurements, calibrated on the observed location of the ^{222}Rn peak. The solid black line is the measured spectrum, and the colored lines are functional fits to the peaks. These fits were used to calculate the rates of the radon daughters, and the results are tabulated in Table 4.4. Figure from [115].

Radon daughters that generate low-energy ER background events through decay are not directly measurable in LUX, though their rates can be estimated based on the parent and daughter α decays. The total estimated rate in the active volume to produce ER backgrounds from these contributions is 0.10-0.22 $\times$ 10^{-3} events/kg/keV$_{ee}$/day [115]. The background model assumes the average value when calculating WIMP interaction cross sections.

4.4.1.2 ^{85}Kr contamination

Research grade xenon procured for LUX operation, like all materials, contains some amount of impurities. As discussed in Chapter 2, the xenon circulation system acts to remove all non-noble gas impurities on a rather fast timescale. However, noble gas impurities are not removed by the getter and must be considered. Krypton, another noble element, is contained within the procured xenon at a concentration of ~130 ppb. Natural krypton contains ^{85}Kr, a 0.687 MeV beta emitter with half-life of 10.76 years with a relative abundance of 2×10^{-11} (g/g) [120]. The corresponding β-emission creates low-energy ER

backgrounds at a rate of 5 events/kg/kev$_{ee}$/day. This rate must be reduced to $< 0.2 \times 10^{-3}$ events/kg/kev$_{ee}$/day, corresponding to a krypton concentration of < 5 ppt in xenon [115].

The LUX krypton removal system uses a column of activated charcoal to separate the krypton from the system through adsorption chromatography. Different species of gas propagate through the adsorption column at different rates, allowing for precise separation of the species. After separation, the measured concentration of krypton (averaged over several samples) in the xenon was 4 ± 1 ppt [115]. The corresponding rate in the target from ^{85}Kr was estimated to be 0.17×10^{-3} events/kg/kev$_{ee}$/day.

4.4.2 Comparison of Background Model with Observations

The background estimations and measurements described in the previous sections are fully incorporated into LUXSim as the LUX background model. LUXSim is then used to generate an expected background spectrum for the WIMP search using the fiducial volume and search parameters described in Chapter 7. The measured and simulated background rates are shown as a function of position in the detector in Figure 4.7. The background expectation averaged over the entire fiducial volume and WIMP search is tabulated in Table 4.5 [115]. The background model is consistent with observed data and is used in the calculation of expected cross section as a function of WIMP mass in Chapter 7. Use of a Kolmogorov-Smirnov (K-S) tests for the height and S1 distribution shapes yields p values of 26% and 94%, respectively, when testing the model against measured data, and the radial distribution is measured to be flatter than predictions with a K-S test p value of 0.004% [115].

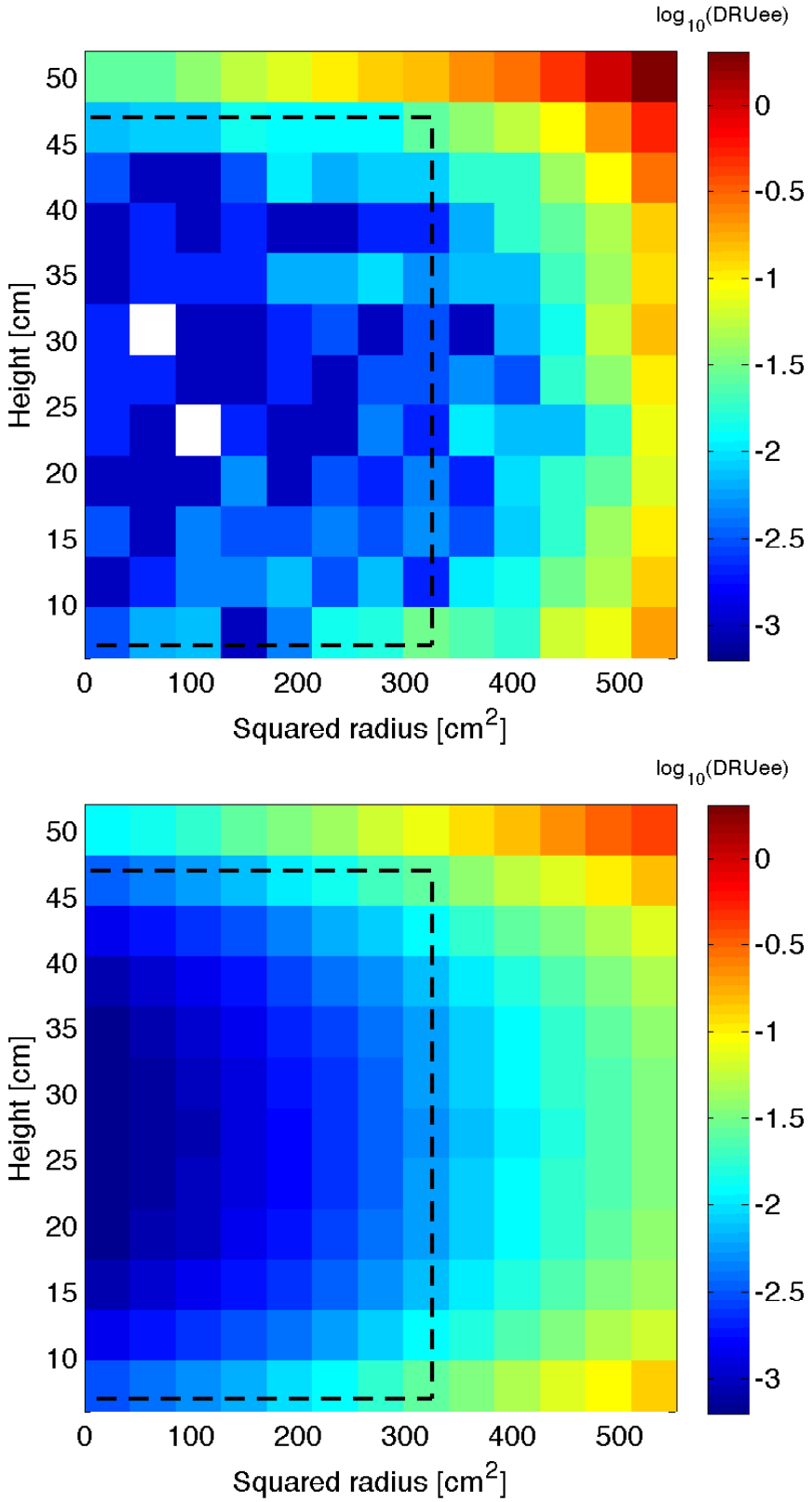

Figure 4.7. Low-energy background distribution located spatially in LUX for data (*top*) and LUXSim background model (*bottom*). The fiducial volume is indicated by the black line. The background model includes all the aspects discussed earlier in this chapter. Figure from [115].

Source	Background Rate (counts/kg/keV$_{ee}$/day)
γ-rays (material backgrounds)	$(1.8 \pm 0.2) \times 10^{-3}$
Activated Xe	$(0.5 \pm 0.02) \times 10^{-3}$
Radon and radon daughters	$(0.11 - 0.22) \times 10^{-3}$
^{85}Kr	$(0.17 \pm 0.1) \times 10^{-3}$
Total Predicted	$(2.6 \pm 0.2) \times 10^{-3}$

Table 4.5. The background model parameters that are incorporated in LUXSim. The rates are normalized for the fiducial volume and WIMP search live time window. Table reproduced from [115].

Chapter 5

Detector Calibrations

Calibrating the LUX detector is necessary to understand its response and characterize various aspects of its operation. Various radioactive sources are used to understand the detector response to ER and NR events and to characterize the light collection and charge extraction efficiencies. Due to the powerful self shielding properties of xenon, using external gamma calibration sources is difficult because the γ's do not penetrate to the central region of the target. Instead, LUX employs internal gamma and beta sources to understand the ER response and energy scale. A neutron generator is used to calibrate the NR response and energy scale. The calibration sources and results are described in this chapter.

5.1 ^{83m}Kr Calibration

^{83}Rb decays to ^{83m}Kr with a half life of 86.2 days. The metastable isotope, ^{83m}Kr, decays with a half life of 1.8 hours to ^{83}Kr, a stable noble element. The decay of ^{83m}Kr emits a 32.1 keV gamma followed by a 9.4 keV gamma, separated by a half-life of 154 ns. The decay scheme of ^{83}Rb to the stable ^{83}Kr is shown in Figure 5.1. ^{83m}Kr is an ideal calibration source for LUX based on the following properties:

- Like xenon, it is a noble gas. It can be carried with the xenon during circulation into the active volume where it will quickly diffuse, providing a volumetric calibration source.

- It has a half life of only 1.83 hours. This allowed for weekly calibrations of LUX dur-

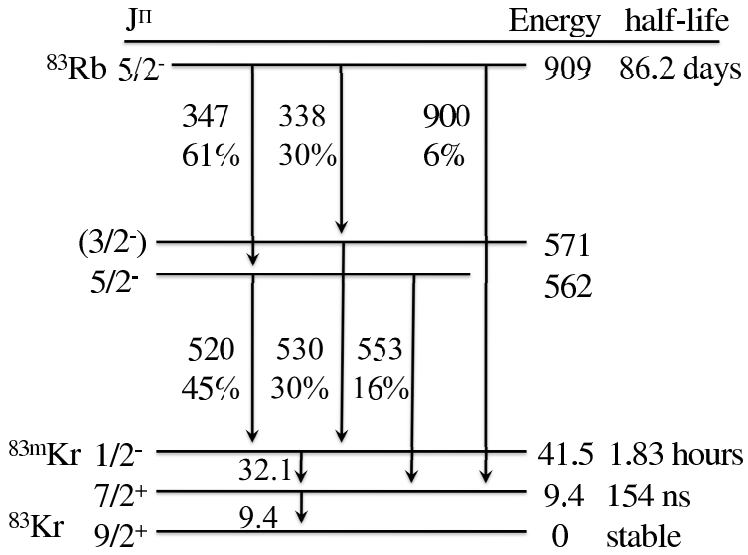

Figure 5.1. The decay scheme of ^{83}Rb to ^{83}Kr. The ^{83m}Kr intermediate state has a half life of 1.83 hours and decays via emission of 32.1 and 9.4 keV gammas. ^{83m}Kr is an ideal calibration source because it can be carried into the active volume and diffuse, providing a volumetric source, its relatively short half life allowed it to be used throughout the WIMP search to monitor the detector status, it decays via gammas that are nearer the energy range of interest for WIMP search, and it decays to a stable noble element which will not affect the ionization electrons that are produced in an interaction. Figure from [121].

ing the dark matter search for the purpose of monitoring the detector status without jeopardizing the WIMP search, because the ^{83m}Kr decayed to an unmeasurable level within a day of the injection.

- It decays via two low-energy gammas that can be used to better calibrate the energy scale of LUX for interactions that better represent WIMP scatters.

- It decays to a stable noble element which ensures that the ionization electrons produced at the interaction site and drifted to the gaseous region will not be affected as more ^{83m}Kr is injected.

A solution containing ^{83}Rb was absorbed into activated charcoal, and allowed to dry. This activated charcoal was placed in a small vessel and plumbed between two valves in a path

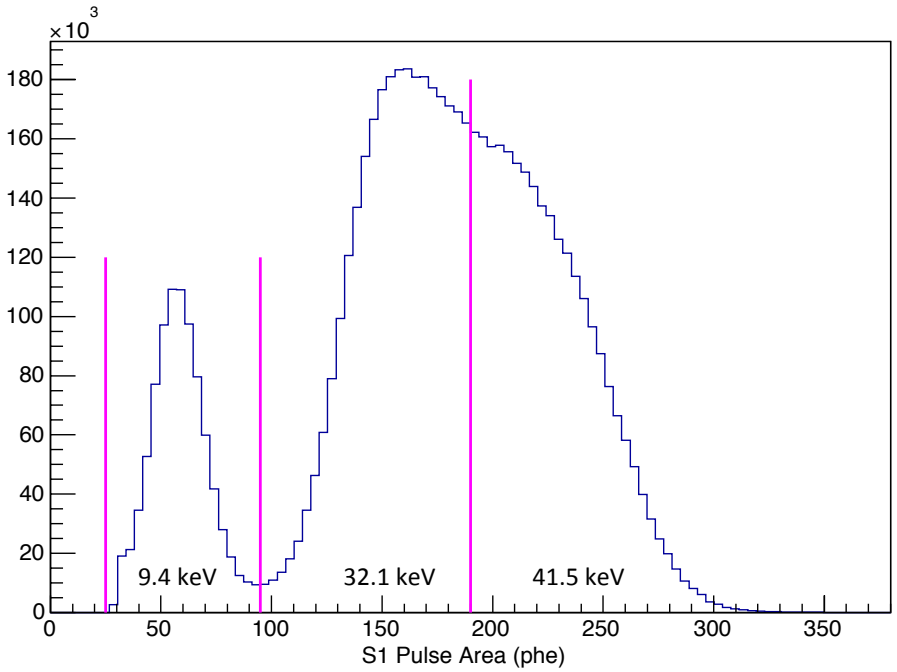

Figure 5.2. The S1 spectrum from the decay of ^{83m}Kr demonstrates the multiple S1s that can be resolved. In some cases, the 9.4 keV and 32.1 keV gammas are detected as a single S1 with area equivalent to 41.5 keV.

parallel with the main xenon circulation flow. When the valves are opened, xenon gas is allowed to flow past the activated charcoal, and some amount of ^{83m}Kr is swept by the flow and carried by the xenon to the detector. The ^{83}Rb-infused charcoal was contained with particulate filters. This ensured that only ^{83m}Kr was introduced into the detector [121].

^{83m}Kr decays consist of the emission of two gammas, so ideally they should produce two S1/S2 pairs in the detector. However, given the short 154 ns half-life of the second decay, what is observed is typically one or two resolved S1s and a merged S2. Three S1 regions are resolved in the data: one corresponding to the 9.4 keV gamma, one to the 32.1 keV gamma, and one to the 41.5 keV case in which the S1s have merged together, as shown in Figure 5.2. To calibrate with a mono-energetic source, events are selected such that each event has two S1s and a single S2. Then, a cut on S1 area is imposed such that the merged 41.5 keV S1 is also considered. This ensures mono-energetic sources for calibration.

5.1.1 Position-Dependent Corrections

Because the ^{83m}Kr diffuses into the target, it provides a uniform, isotropic, calibration source in the volume, which can be used to understand the non-uniformities in LUX. Ideally, the detector is constructed to be symmetric, but on small scales deviations are possible, such as warpage in one of the teflon reflective panels affecting the light collection at a particular spot. Also, even though they are gain-matched, variations in quantum efficiencies of PMTs could result in non-uniform response across the detector. These systematic errors bias the measured pulse areas in certain locations, causing local "hot" and "cold" spots of detector activity. To remove these systematic effects, the pulse areas are corrected by a position-dependent factor such that each pulse is normalized to those at the center of the detector (X=Y=0 cm and Z = 160 μs = 28.7 cm). The ^{83m}Kr source is used to normalize the S1 and S2 pulse areas. Once corrected, pulse areas are designated with the subscript "c."

To correct the S1 pulse area in Z, the data are broken up into 65 slices in Z, in units of μs. A Gaussian fit is made to the S1 pulse areas in each slice to determine the mean S1 pulse area. A function of the form

$$A + Bx + Cx^2 + Dx^3 + Ex^4 \tag{5.1}$$

is fit to the mean pulse areas as a function of Z to determine the Z-dependent correction, normalized to the center of the detector at Z = 160 μs. The result of this exercise is shown in Figure 5.3.

After correcting the S1 areas to the center of the detector, they must be corrected in XY as well. To do this, the detector is broken into a 25×25-cell grid, so each cell is a 2 cm-sided square. The S1 pulse areas are binned according to their XY positions, and a Gaussian fit of the areas is made to each cell. The mean areas of each cell are then normalized to the area at the center X=Y=0, providing a normalization factor for each cell to correct S1 areas that are in it. Because ^{83m}Kr was injected into the active volume regularly, the fluctuations in these correction factors was studied, and it was found that the S1 correction factors do not change at a level higher than a few per cent over the course of the WIMP search. Therefore, the same S1 correction factors were applied to all the WIMP search and calibration data.

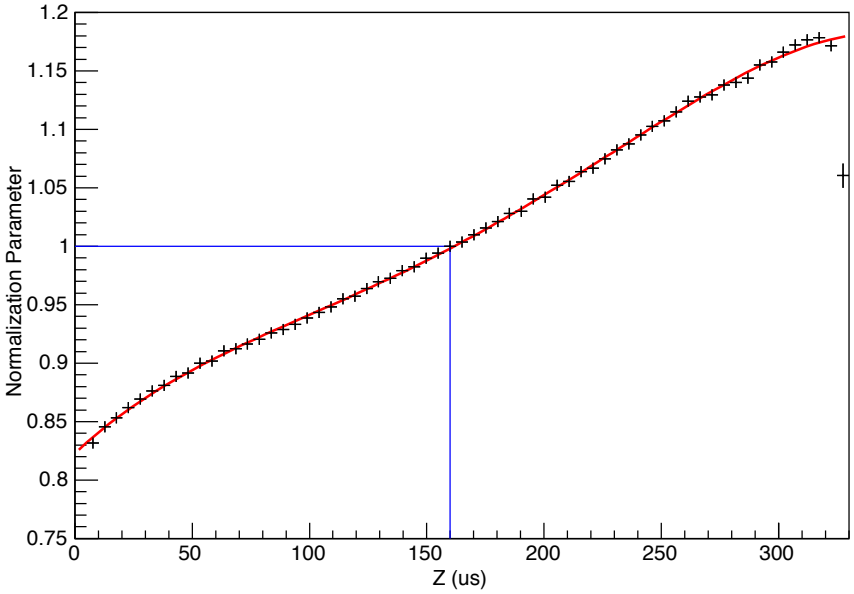

Figure 5.3. The S1 area Z-dependent correction function. S1 pulse areas are grouped into 65 slices in Z and normalized to the center of the detector at Z = 160 μs, shown in the blue lines.

The S2 areas were also corrected using the ^{83m}Kr calibration source. First, the S2 areas were corrected for the depth of the event in Z. Since the drift distance is fixed by the grids, all S2s should have the same response since each is being produced by the same energy (41.5 keV). However, non-noble element impurities in the liquid attract ionization electrons as they drift, reducing the overall size of the S2. The electron lifetime is an exponential metric used to describe the distance an electron will travel before it interacts with an impurity. The electron lifetime must be at least as long as the maximum drift in the detector. To measure the electron lifetime, the S2 pulse areas are plotted as a function of drift time, and an exponential is fit to the distribution, shown in Figure 5.4, *top*. The exponential fit parameter is the electron lifetime. Figure 5.4, *bottom* shows the electron lifetime as a function of day during the WIMP search. For the majority of the run, the electron lifetime was fairly constant with an average value of ∼800 μs, well above the minimum required. In fact, only when xenon circulation was stopped did the electron lifetime decrease, shown in two points on the plot. Therefore, a value of 800 μs was used to correct the Z dependence

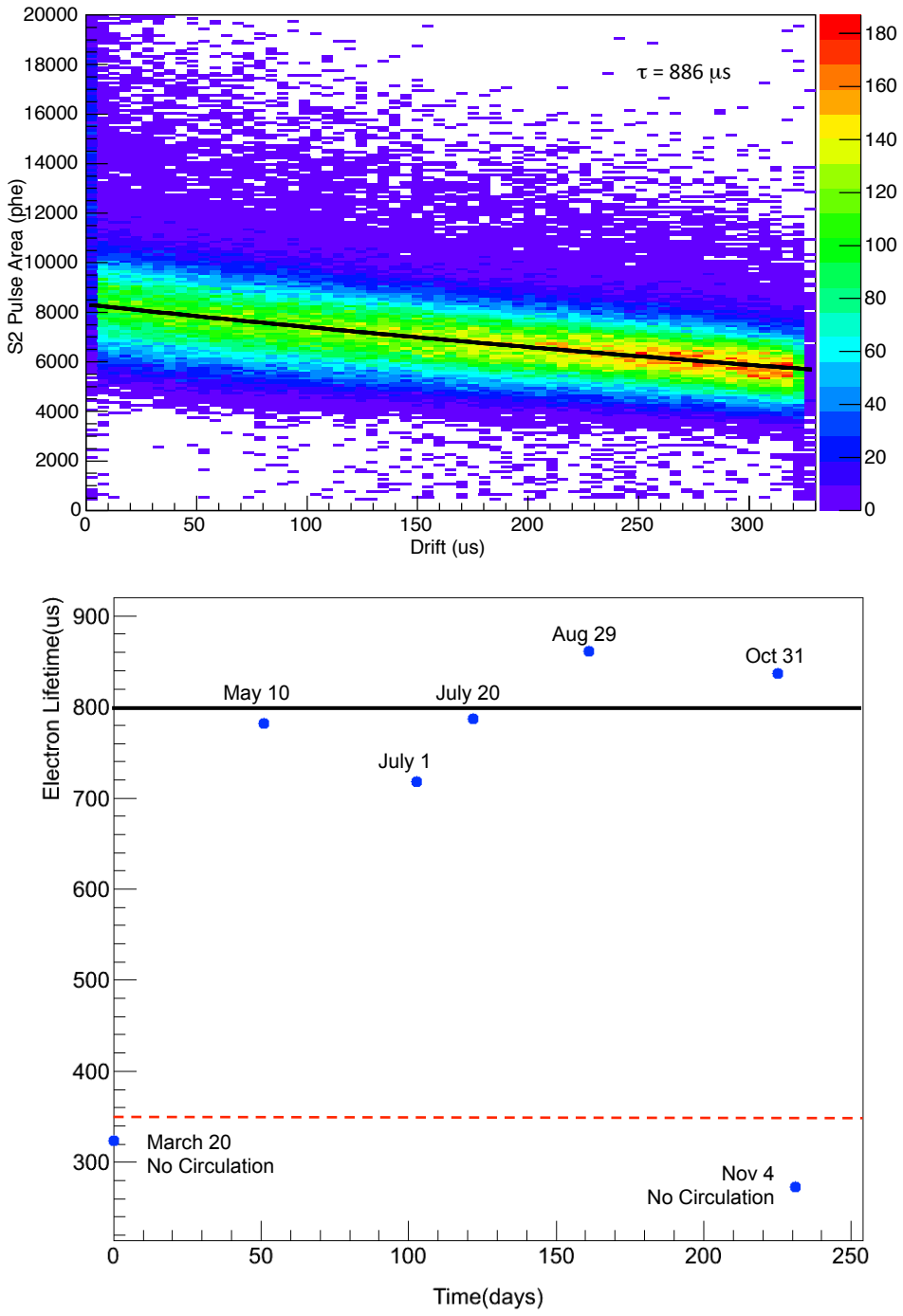

Figure 5.4. *top*: The procedure for determining the electron lifetime. The S2 area is plotted as a function of drift time, and an exponential function is fit to the distribution. The parameter in the exponential is the electron lifetime. *bottom*: The electron lifetime during the WIMP search. As long as xenon was being circulated, the electron lifetime remained roughly constant with average value of ∼800 μs. When circulation was stopped, the electron lifetime quickly fell. The red line represents a drift of 350 μs, the maximum time it could take an electron to drift in LUX.

of the S2 pulse areas.

Similar to the procedure for S1 areas, after the S2 areas were corrected to the top of the liquid by the electron lifetime, they were corrected in XY as well using the same grid structure and method described above. Also, as was the case for S1 XY correction factors, the S2 XY correction factors were found to be fairly consistent throughout the WIMP search, and a single value was used for each bin to correct all the data.

Applying these position-dependent corrections improved the energy resolution of the detector. In Figure 5.5, *top*, the S1 pulse area distribution is shown for the combined S1 pulse. The red distribution is uncorrected, and has a resolution of 0.13. The blue distribution is of corrected pulse areas, and the energy resolution improves by $\times 1.5$ to 0.089. Figure 5.5, *bottom*, shows the distribution of S2 pulse areas for uncorrected (red) and corrected (blue) pulses. Again, the energy resolution improves with the corrections applied, and the distribution becomes more Gaussian. It is unclear why the original distribution is not Gaussian, but one possible reason is statistical fluctuations in electron absorption. As ionization electrons are removed by impurities, making large pulses smaller, a "tail" is formed at large pulse areas. With the application of the electron lifetime correction, electrons are "put back" into pulses where they belong. This has the effect of shifting the mean of the S2 area distribution to a larger value, and increasing the energy resolution.

5.1.2 Multiple S1/S2 Pairs

For the corrections, a mono-energetic source was needed, and ^{83m}Kr does decay via emission of two gammas, and it is possible for the pulse finder and pulse classifier to resolve two S1s from an event. Now considering events with two S1s, the time between them is binned into a histogram, shown in Figure 5.6. An exponential fit applied to the distribution yields a measured time constant of 152.2±0.8 ns, which corresponds to the half-life of the 9.4 keV γ following the emission of the γ at 32.1 keV. According to the literature (see Figure 5.1), this time should be 154 ns. The measured time is in reasonable agreement with the expected time, indicating that both S1s were properly resolved. One possible explanation for the small discrepancy between the measured and expected times is that it is caused by the fact that some events contain multiple ^{83m}Kr decays. An improved event selection procedure can

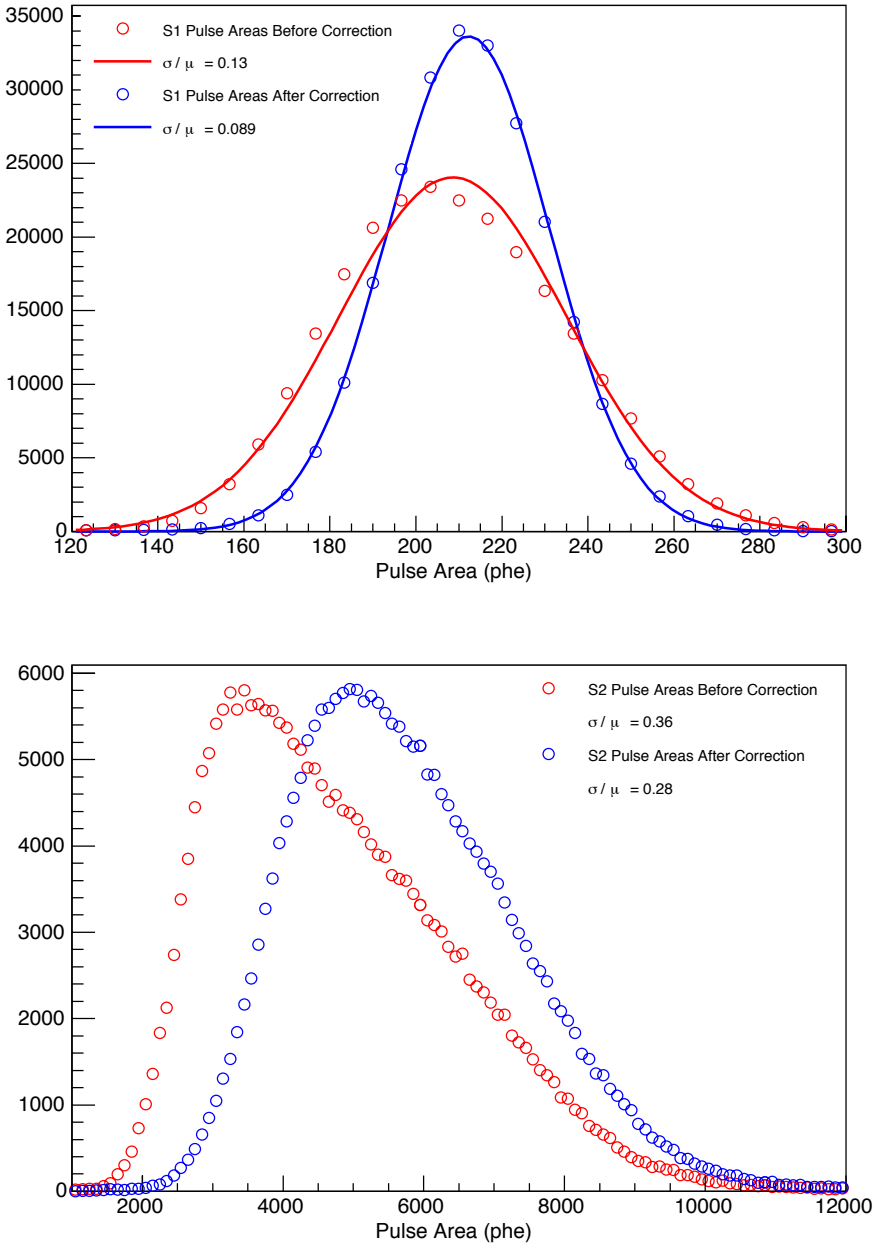

Figure 5.5. The S1 and S2 resolutions improve from the uncorrected (red) distribution to the corrected (blue) distribution. *top*: The width of the S1 distribution decreases by ×1.5. *bottom*: The S2 resolution improves, and the distribution becomes more Gaussian which is expected as the electron lifetime correction is applied.

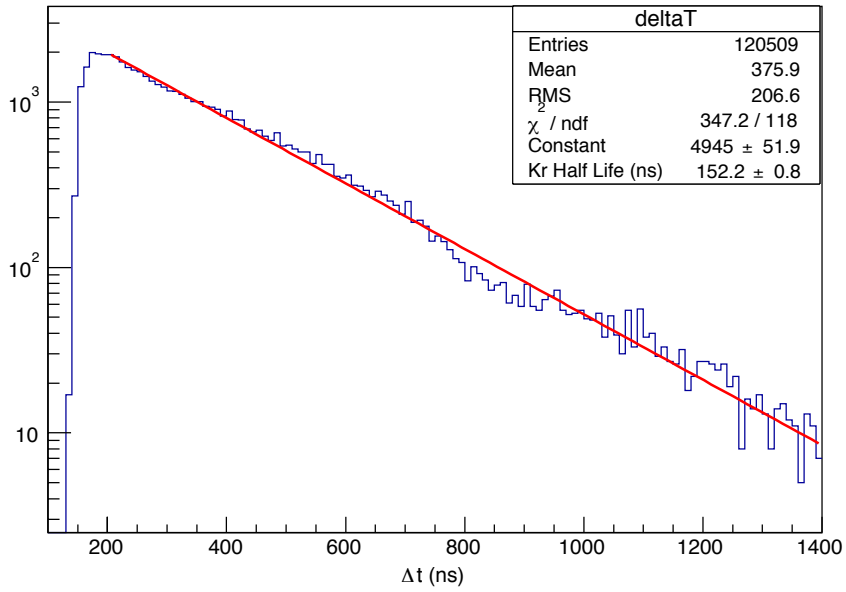

Figure 5.6. The measured time between multiple ^{83m}Kr S1s in an event. Each ^{83m}Kr decays via emission of two gammas, and each gamma can be resolved. The time between multiple S1s in an event window is binned into this histogram. An exponential fit to the distribution yields a separation time of 152.2±0.8 ns, agreeing well with the expected value of 154 ns. This demonstrates the ability of the pulse finder and pulse classifier to effectively resolve events with multiple S1s.

reduce the effect these overlapping events have on the spectrum.

As is evident in Figure 5.6, there is a large population of events with S1 separation larger than 1000 ns. Assuming the average width of an S2 to be ∼1 μs, it should be possible to resolve events with two well-separated S2s. Since ^{83m}Kr is relatively stationary during its decay, it is reasonable to assume that both gammas are emitted at the same location, within a few μm. Therefore, both interactions should take place in the same location, separated only in time. Using events with two S2s can then allow for a characterization of the position reconstruction software to be done by selecting events with 2 S1s separated by at least 1 μs. The result of this study is shown in Figure 5.7, which contains a spectrum of the difference in the reconstructed radial position between the two S2s assuming the event selection criteria described previously. There are two distributions apparent: a wide distribution and a narrow distribution. The wide distribution is possibly due to mismatches S1/S2 pairs and

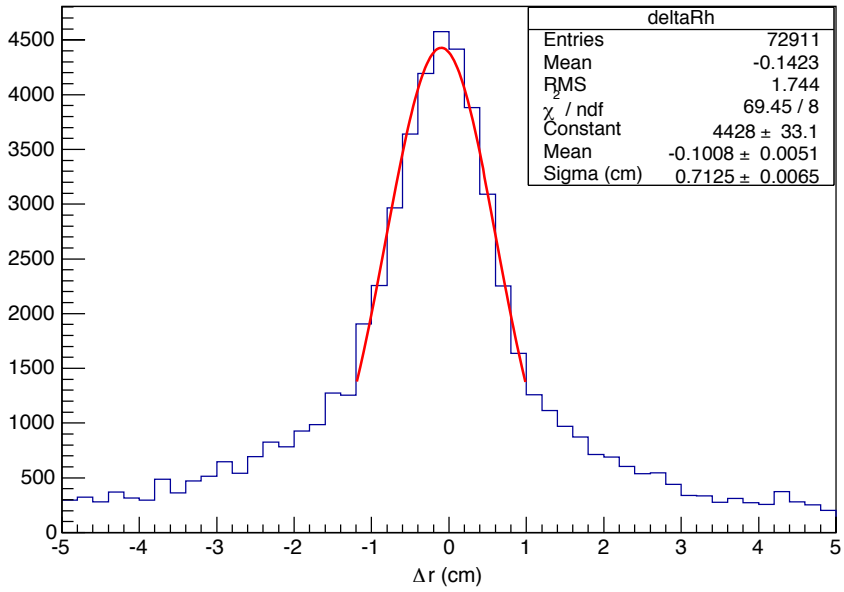

Figure 5.7. The resolution of the position reconstruction software measured with ^{83m}Kr decays. Events with 2 S1s separated by at least 1 μs with 2 S2s are selected. The emission of each gamma from the decay of ^{83m}Kr is assumed to occur at the same location in space. The difference between the reconstructed position of the first S2 compared with the reconstructed position of the second S2 gives the resolution. There are two distributions apparent. The wide distribution is the result of multiple ^{83m}Kr decays in the same event window, and the narrow distribution is the result of a single ^{83m}Kr in the event window. The resolution of the position reconstruction algorithm is 0.7 cm. Improved event selection criteria can be imposed to reduce the wide distribution and obtain a better measurement of the resolution.

also a result of multiple ^{83m}Kr decays in the same event, while the narrow distribution is the result of a single ^{83m}Kr decay. Considering only the narrow distribution, the resolution of the position reconstruction algorithm, in $r = \sqrt{x^2 + y^2}$, is measured to be 0.7 cm.

Since ^{83m}Kr decays in a well known way, the S1 scintillation yield can be extracted from the data. Since the 32.4 keV gamma and 41.5 keV combined energies are so close together, it is difficult to properly resolve those different S1 distributions. The S1 resulting from the 9.4 keV gamma, however, is well separated from the other two. Figure 5.8 shows the S1 distribution from the 9.4 keV gamma. The S1 pulses have a mean area of 57.9 ± 3.5 phe, resulting in a scintillation yield of 6.15 ± 0.40 phe/keV.

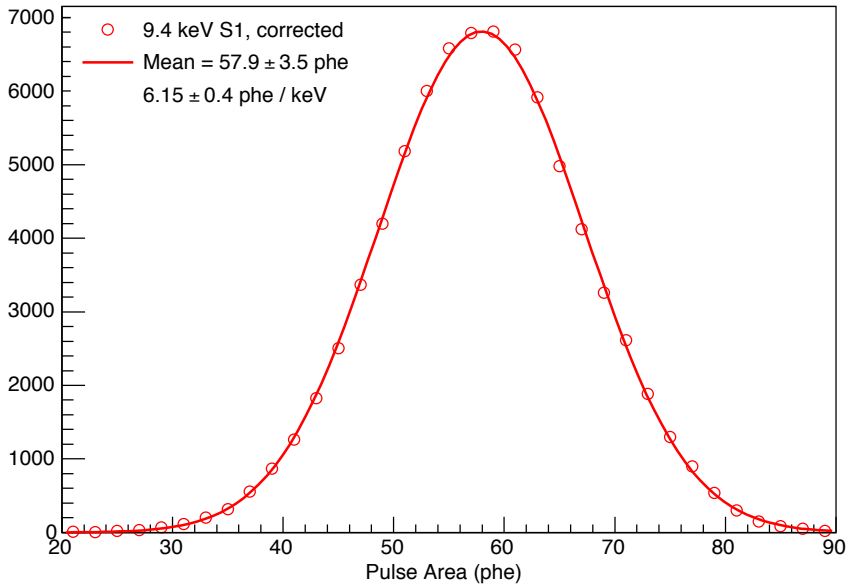

Figure 5.8. The S1 scintillation yield from the 9.4 keV gamma emitted in the ^{83m}Kr decay. The mean S1 area is 57.9±3.5 phe, resulting in a scintillation yield of 6.15±0.40 phe/keV.

5.2 ER and NR Calibration Sources

NR calibrations were conducted using a neutron generator as the source of neutrons. After the WIMP search had completed, an Adelphi DD108 deuterium-deuterium (DD) neutron generator was situated outside the LUX water shield. This generator emitted a maximum of 10^8 neutrons/s distributed isotropically at an energy of 2.45 MeV. To direct the neutrons into the LUX detector, a 3.8 m long plastic, air-filled tube was oriented in the water tank between the DD generator and LUX, providing a delivery system with no water. This allowed a large number of the neutrons to travel from the DD generator to the detector cryostat without suffering any collisions. Both the DD generator and the tube could be adjusted in Z, allowing for the calibration of the active volume in XYZ. 70.4 live-hours of neutron calibration data were recorded during the calibration.

ER calibrations were conducted by administering tritium into the active volume, in a fashion similar to the krypton calibration, providing an internal source. Tritiated methane (methane gas with a hydrogen atom replaced by tritium) is injected into the circulation path, enters the active volume, and quickly diffuses throughout. Tritium decays by β emission

with a 12.3 year half-life and end point energy 18.59 keV_{ee}. Because every decay results in an ER interaction and the β's are emitted in a spectrum, the tritium source was an excellent calibration source to use for ER calibrations.

5.3 Calibration of Detector Parameters

5.3.1 Energy Scale

When an interaction occurs, the models (2.6) and (2.7) predict the number of photons and electrons that will be produced at the interaction site. Due to interactions between the emitted photons and impurities in the detector or the surfaces within the detector, the number of observed photons at the PMTs is lower than the number that is emitted by the interaction. The relationship between observed photons (S1) and emitted photons (N_γ) is

$$S1 = g_1 N_\gamma. \tag{5.2}$$

In this relation, g_1 is referred to as the light collection efficiency. The LUXSim and NEST models were used to determine the value of g_1 in LUX.

Similarly, the number of ionization electrons, N_e, is reduced by absorption on impurities while drifting and further reduced by the extraction efficiency at the liquid surface. The amount of detected light generated during electroluminescence (S2) is given by

$$S2 = \epsilon g_2 N_e. \tag{5.3}$$

Here, ϵ is the extraction efficiency and g_2 is the number of photoelectrons detected per extracted electron. The value of g_2 can be measured directly from the single electron sample in the data, and in turn used to tune the LUXSim and NEST models to understand the electron extraction efficiency.

The values of g_1, g_2, and ϵ allow an estimation of the deposited energy in an event to be made, based on the observables S1 and S2. The formula

$$E = W L^{-1} \left(\frac{S1}{g_1} + \frac{S2}{\epsilon g_2} \right) \tag{5.4}$$

provides the link between the observed light and the deposited energy. Recall W is the average energy needed for the creation of electrons or γ,s (13.7 eV) and L is the Lindhard factor

which described the behavior of ER vs NR energy partitioning. With a proper understanding of the detector parameters, a reasonable estimation of the original energy deposition is possible.

The DD calibration data were used to measure these detector parameters. First, the size of a single-electron signal was directly measured. Figure 5.9, *top* shows the pulse area distribution in the range 0-35 phe. The first observed peak is the single photoelectron background, and the distribution is centered at an area of 1 phe, as expected. The second observed peak is the detector response to a single electron. Figure 5.9, *bottom*, shows only the single electron region. A Gaussian fit to the distribution yields a value of 19.6 ± 4.9 phe/e^-.

Using this value, a χ^2 minimization is performed by tuning the NEST model and comparing the output with the DD calibration data to find the best-fit values of the light collection efficiency and the extraction efficiency. The best fit values were $g_1 = 0.12 \pm 0.02$, $\epsilon = 0.51 \pm 0.09$, and $g_2 = 9.99$ phe/e^-.

5.3.2 Charge Yield

An important detector parameter that must be known is the charge yield, a measure of the number of extracted electrons produced as a function of deposited energy. The charge yield is vital for energy scale calibration, i.e., converting the measured pulse areas to individual recoil energies. To measure the charge yield, the DD neutron source was used [122]. Neutrons were incident upon the detector, and with some probability would scatter multiple times within the liquid. Rather than rejecting those multiple scatters as in the WIMP search, they were selected for this study. The scattering angle of the first vertex can be determined given the relative reconstructed positions of each vertex (assuming that the incidence angle was zero). The scattering angle can then be used to determine the actual recoil energy of the original energy deposition (assuming there was no earlier energy loss and the incident energy was 2.45 MeV). Given the single electron size determined above, the number of electrons per deposited energy is estimated. The charge yield for LUX, measured in this way, is shown in Figure 5.10. This direct, *in situ* measurement indicates continued, excellent sensitivity to energies as low as $\sim$1 keV_{nr}. The black line in the figure is the prediction of the NEST model which is in reasonable agreement with the data even at these low energies,

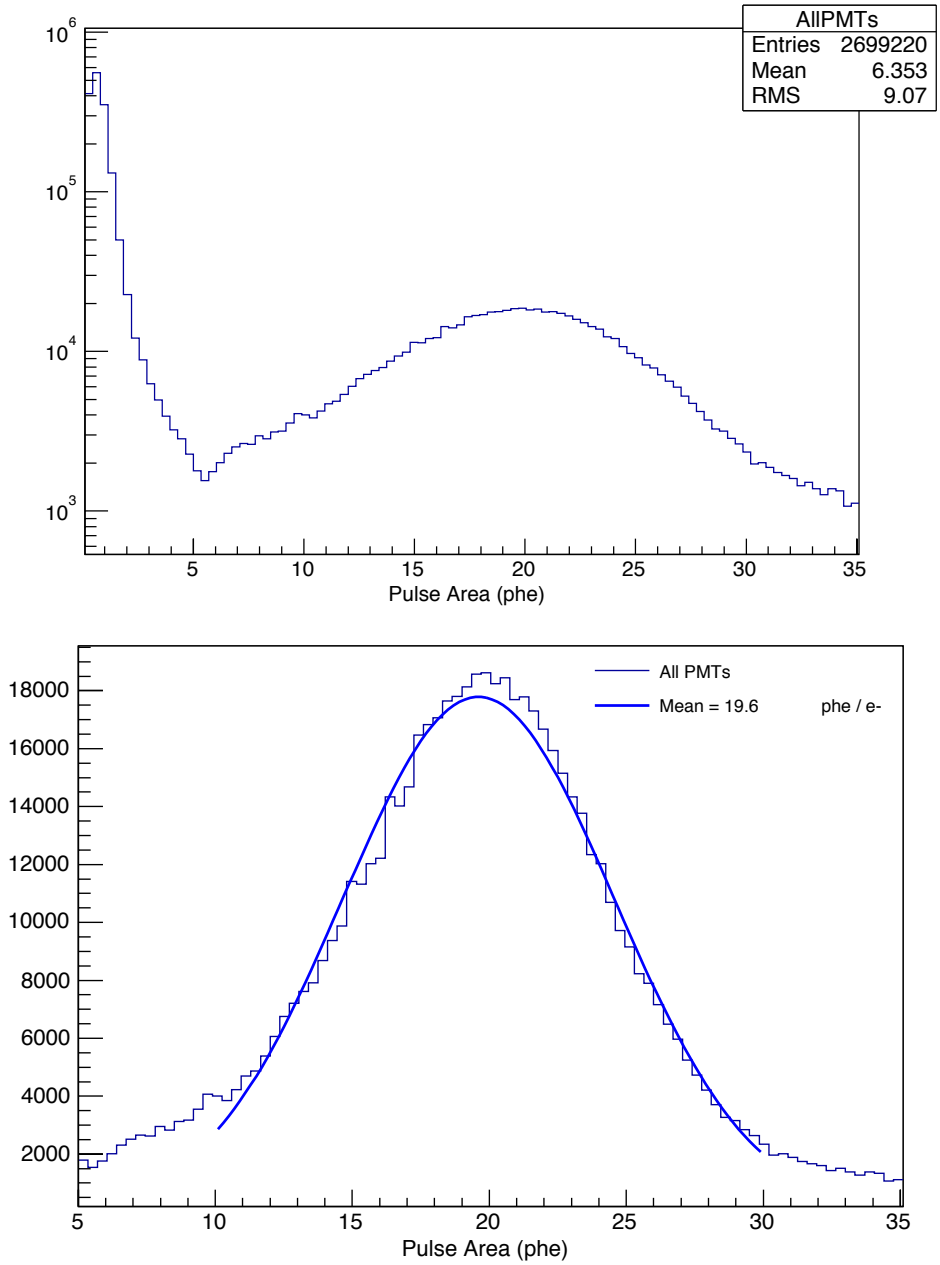

Figure 5.9. The response of the LUX detector to a single electron. *top*: An expanded view of the distribution. The first peak is the distribution of the response to the single photoelectron, centered at 1, as expected. The second peak is the response to the single electron. *bottom*: The response of the detector to a single electron. A Gaussian fit to the distribution yields a mean value of 19.6 ± 4.9 phe/e^-.

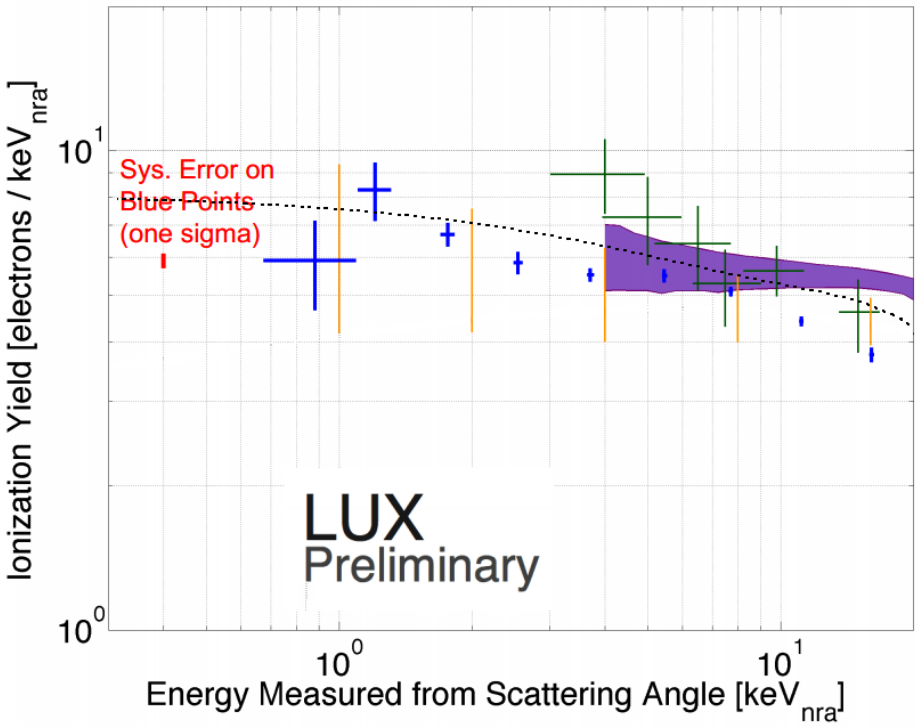

Figure 5.10. The charge yield calibration in LUX. An *in situ* measurement of the number of ionization electrons per incident recoil energy was conducted (blue crosses), indicating a continued excellent sensitivity to NR events at low recoil energies, leading to a higher sensitivity to low-mass WIMPs. The NEST model is shown as the dotted line, in general agreement with the data. This validates the model at low recoil energies. The green crosses are from an earlier measurement by [99]. The preliminary designation indicated that the result has been presented but has not to date been published. Figure from [122].

thus validating the model.

5.3.3 Relative Scintillation Efficiency

Using the determined charge yield and the measured relationship between ionization and scintillation, the relative scintillation efficiency, L_{eff} can be determined from the same data, though using single-scatter events in this case [122]. A NEST monte carlo simulation is used to simulate the expected S2 spectrum, normalized to the DD data. For each S2 bin, the S1 spectrum is simulated, varying the energy parameter by a sweep of scale factors in order to vary the light yield in the simulation. Next, for each bin in S2, a χ^2 minimization is performed to determine the optimal energy scale factor. Because the NEST prediction of the charge yield was verified by the measurement described above, the measured L_{eff} at

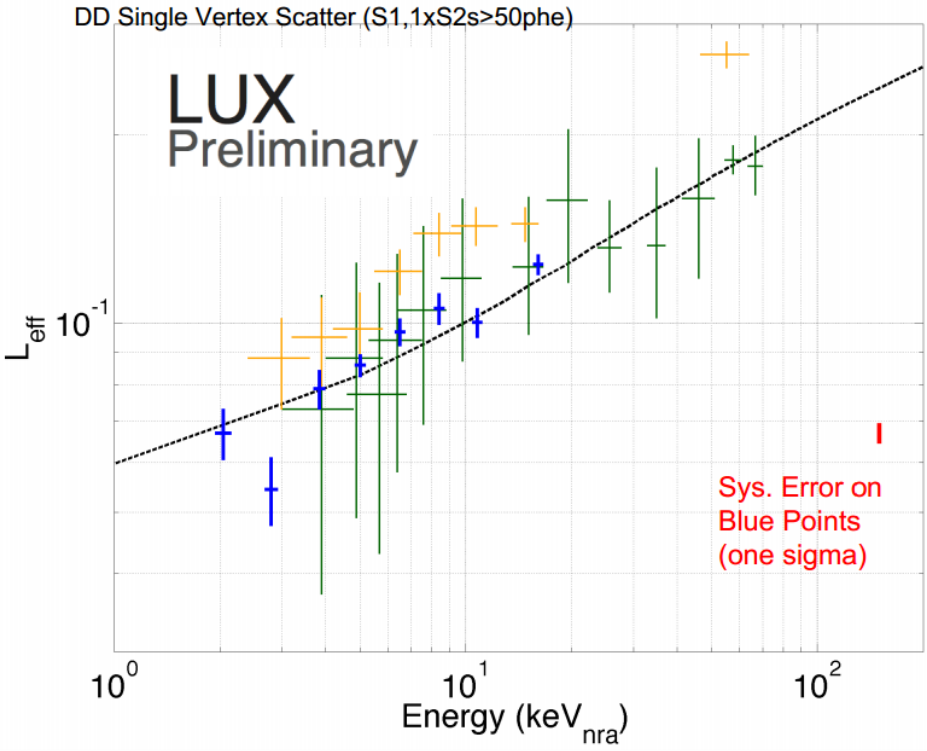

Figure 5.11. The relative scintillation efficiency, L_{eff}, measured in LUX (blue), with DD calibration data. This data extends the measured scintillation response down to 2 keV$_{nr}$. The NEST model, shown in black dashed line, matches well and indicates a continuing trend as energy decreases. The yellow crosses are from [98] and the green crosses are from [99]. The preliminary designation indicated that the result has been presented but has not to date been published. Figure from [122].

each energy will be the NEST modeled value of L_{eff}, scaled by that factor in each bin. The result is shown in Figure 5.11. The NEST prediction, shown in black dashed line, agrees very well with the LUX DD data (blue) at energies as low as 2 keV$_{nr}$, and it indicates a continuing trend as energy continues to decrease, further validating the model. From this calibration and the charge yield calibration, it is concluded that the NEST model is valid at recoil energies as low as 1 keV$_{nr}$.

5.4 Discrimination

The ability to discriminate between ER and NR events allows for the rejection of ER background events, resulting in a greater sensitivity. Discrimination in LUX is achieved using the $log_{10}(S2_b/S1_c)$ variable, where $S2_b$ is the S2 area (energy) as measured by the bot-

tom PMT array and $S1_c$ is the area (energy) of the S1 measured by both PMT arrays. Both areas are corrected to the center of the detector. The discriminating parameter is plotted as a function of energy, measured in units of $S1_c$. In this spectrum, the same cuts used in the WIMP search are applied, described in detail in Chapter 7. This procedure provides adequate discriminating power for separating NR and ER events.

5.4.1 NR Band Calibration

The natural calibration source to use to understand the response of the detector to NR events is the DD source. Unfortunately, due to the excellent self-shielding of liquid xenon and the difficulty in delivering a high number of neutrons to the active volume (given the fact that the neutron generator was located outside the water tank nearly 4 m away), achieving enough statistics to confidently build a response band proved difficult. Therefore, a simulation based on NEST was used to build the NR response bands and compared with the calibration data.

After tuning the model parameters with the DD data as described above, an NR spectrum was generated by simulating NR events with a flat energy spectrum from 0-50 keV_{nr} and plotted versus S1_c, binned in steps of 1 phe, as shown in Figure 5.12. A Gaussian was fit to the data in each bin in slices of S1, and a function of the form

$$f(S1) = \alpha S1^{\beta} \tag{5.5}$$

was fit to the mean and 1.32σ values of the fit. These functions, shown in red, represent the mean and extent of the NR band. The values of each parameter are shown in Table 5.1.

To ensure that these bands accurately describe the data, they are also plotted against the same spectrum, generated from DD data. This comparison is shown in Figure 5.13. Both panels show the same data, albeit in different forms. It is evident from the bottom panel that, at high S1, the statistics are not acceptable, hence justifying the need to use the simulated spectrum to generate the NR response bands. The dotted red vertical lines show the boundaries of the WIMP search box. It is clear from these plots that the simulated NR response bands can accurately describe the observed data.

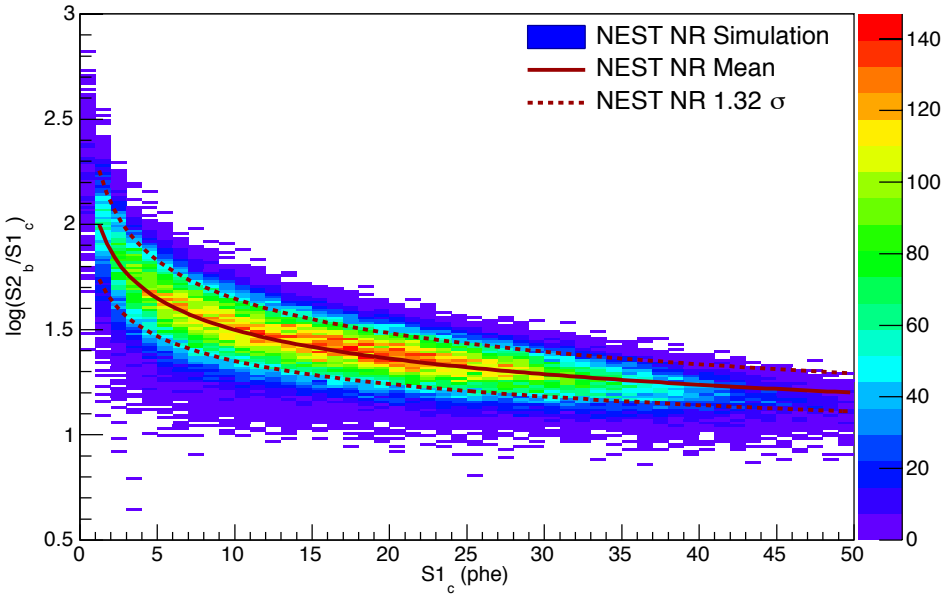

Figure 5.12. The NR band generated by simulation. The NEST models were tuned to account for the light collection measurements according to the DD data, and NR events flat in energy were simulated. Functions fit to the mean and 1.32σ deviation of Gaussian fits to the data in each S1 bin are shown in red.

		α	β
NR	Mean	2.05	-0.13
	$+1\sigma$	2.24	-0.14
	-1σ	1.85	-0.13
ER	Mean	2.57	-0.14
	$+1\sigma$	2.70	-0.13
	-1σ	2.43	-0.14

Table 5.1. The fit parameters for the NR and ER bands. The functions are of the form in (5.5).

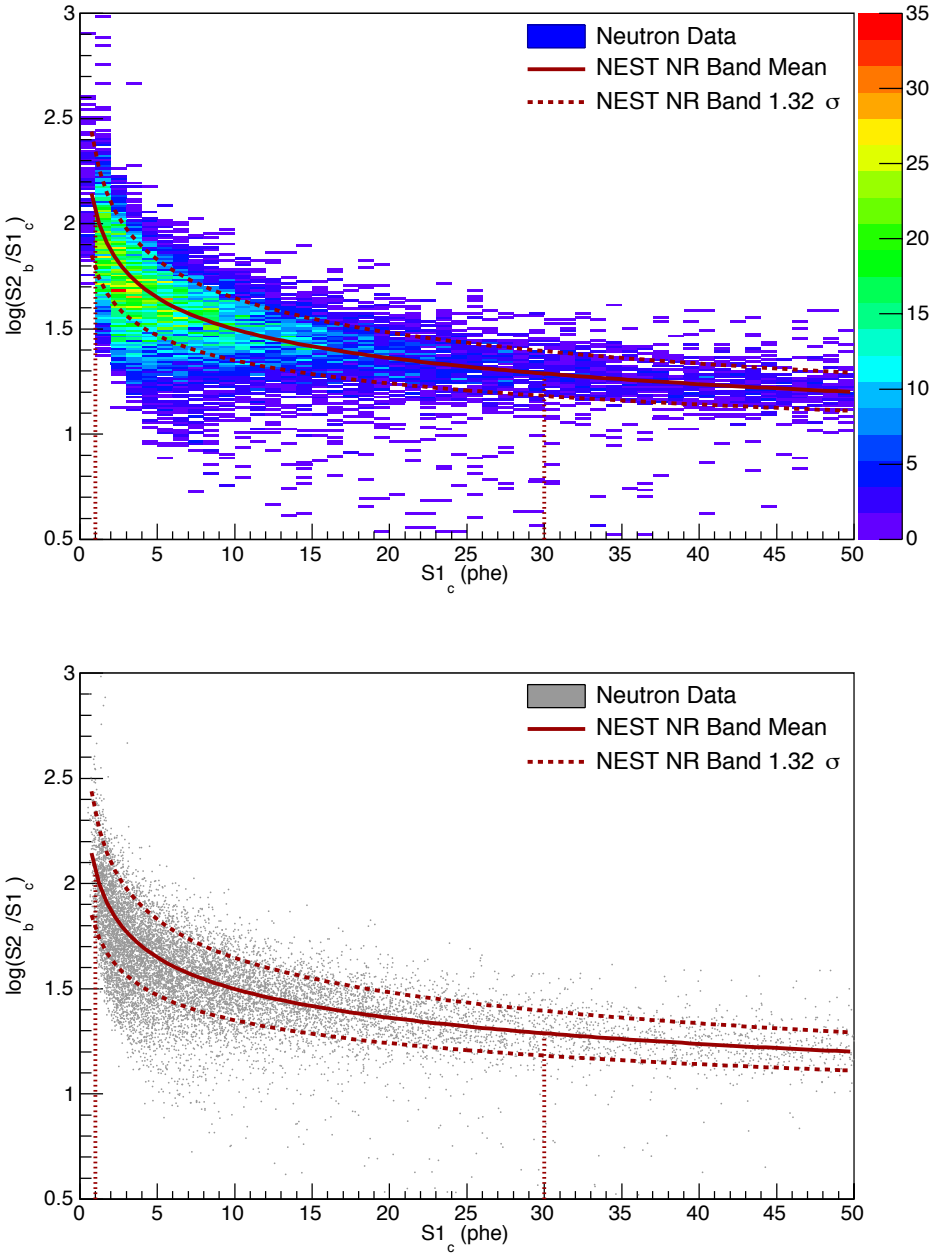

Figure 5.13. The NR bands, derived from simulation, applied to DD data. Both panels show the same data in different forms. From the bottom panel it is evident that, at high S1, the statistics are not acceptable, hence the use of the simulated spectrum to generate the NR response bands. The dotted red vertical lines show the extent of the WIMP search box.

5.4.2 ER Band Calibration

The ER band is measured with the tritium calibration data. Because this is an internal source, there is no issue with statistics, and the data were used directly. The discrimination parameter is plotted versus $S1_c$, in bins of 1 phe. A Gaussian is fit to the data in each bin, and a power law function of the form (5.5) is fit to the mean and 1σ deviation of fit from each bin. The resulting fit parameters are listed in Table 5.1. The ER response band is shown in Figure 5.14. It is evident in the figure that there is good discrimination between ER and NR events, as expected, and the level of discrimination is discussed in the next section.

5.4.3 Discrimination Power

The ability to discriminate between NR and ER events allows for a powerful measurement when searching for a particular type of event. From Figure 5.14, it is clear that some number of ER events lie within the NR band. Since a WIMP interaction will be of the NR type, the NR band must be clear of ER events. A WIMP search region, consisting of a subset of the NR band, is defined within the discrimination space to ensure a maximum power for discriminating ER events. The WIMP search region is defined as the space that lies below the NR band mean, assuring a 50% acceptance of NR (or WIMP) events. The discrimination power in LUX is shown as a function of S1 area in Figure 5.15. Because the acceptance region is defined as the area below the NR band mean, the ER rejection is calculated on a bin-by-bin basis by subtracting the NR band mean from the ER band mean and integrating

$$R = 1 - \left(\int_{-\infty}^{-\beta} \frac{1}{\sqrt{2\pi}\sigma_{er}} e^{\frac{-1}{2}\left(\frac{x-\mu_{er}}{\sigma_{er}}\right)^2} \mathrm{d}x \right) \tag{5.6}$$

$$\beta = \frac{\mu_{er} - \mu_{nr}}{\sigma_{er}}. \tag{5.7}$$

In this equation, μ_{er} and σ_{er} are the mean and width, respectively, of the Gaussian fit to the ER profile in a given S1 bin and μ_{nr} is the fitted mean of the NR band. The average ER rejection in the WIMP search range of S1 from 1-30 phe is calculated to be better than 99.95% with 50% acceptance for NR events. However, the ER band exhibits non-Gaussian behavior as S1 decreases, so the discrimination is instead calculated as the fractional number of ER calibration events that fall into the WIMP search region compared with the total number of events. With this method, the discrimination of ER events is $> 99.5\%$.

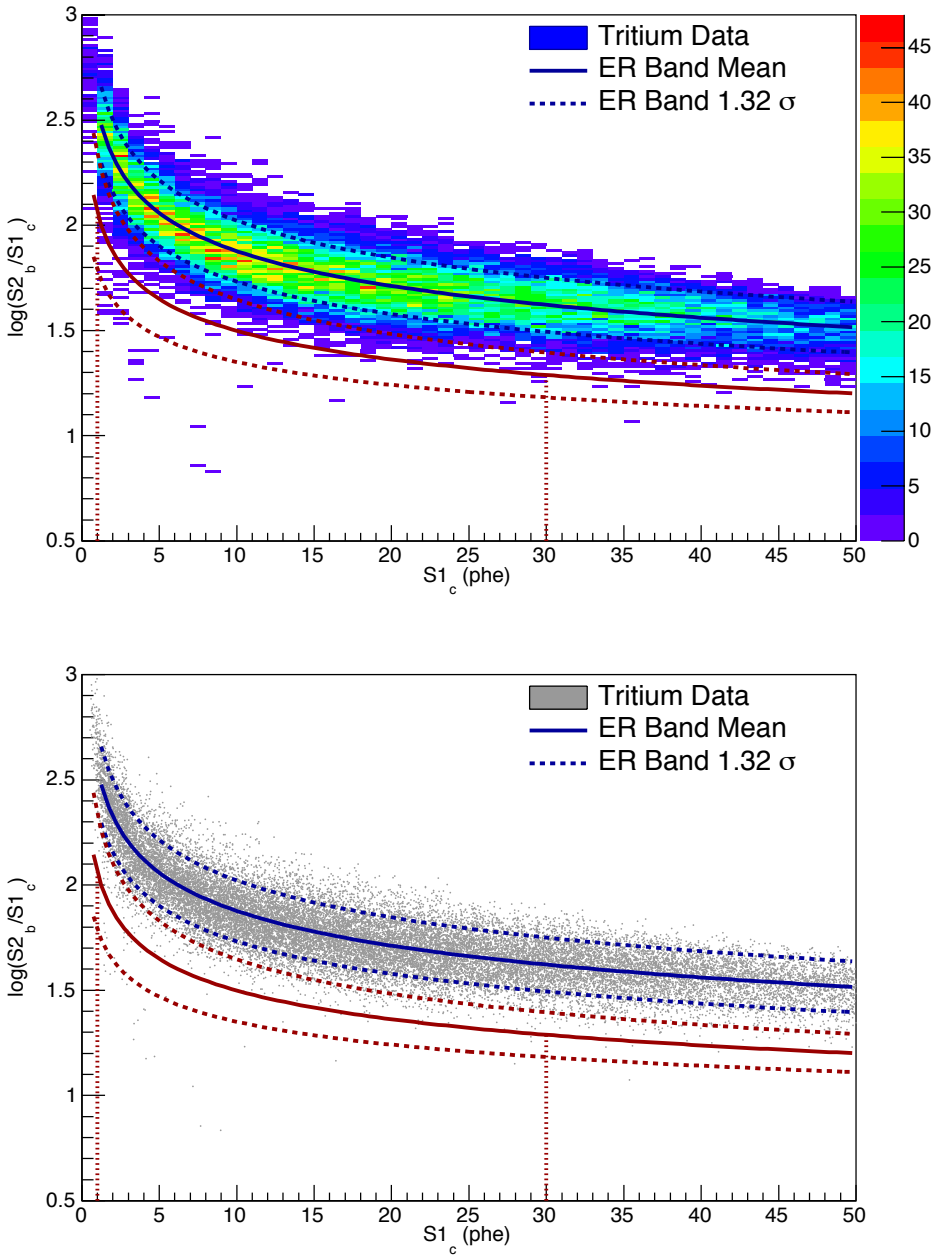

Figure 5.14. The ER response spectrum and resulting bands measured with tritium calibration data. The mean and 1.32σ bands are shown in blue, and the NR bands are shown for comparison in red. The dotted red lines represent the boundaries of the WIMP search region.

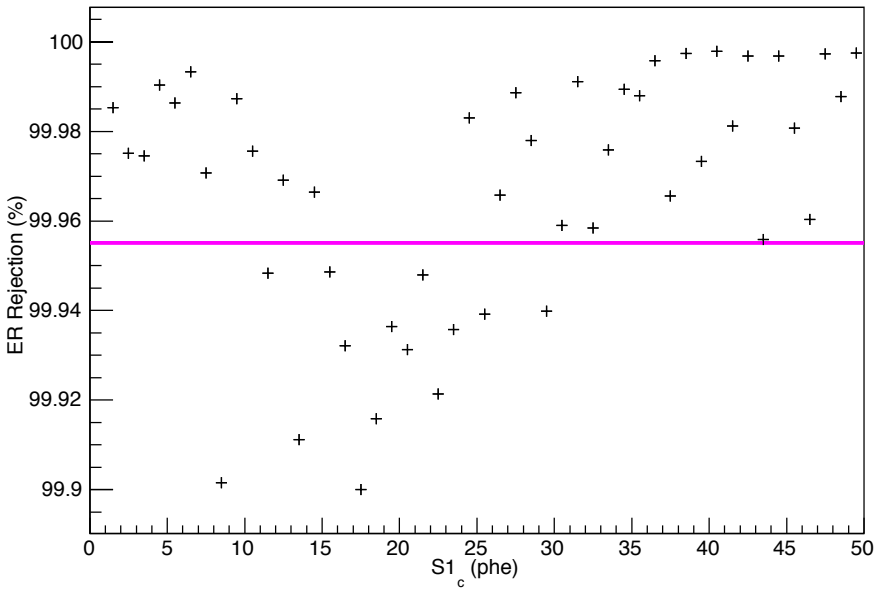

Figure 5.15. The ER rejection in the WIMP search region is shown as a function of S1. The average rejection, calculated from 1-30 phe in $S1_c$ and shown in magenta, is better than 99.95%, assuming a 50% acceptance of NR events in the WIMP search box.

Chapter 6

Detector Performance

As described in Chapter 2, the LUX detector was designed to record any signal that exceeded a digitization threshold, regardless of triggering decision. The trigger information is then used to group digitized waveforms into 1 ms event windows, but as will be described in this chapter, the detector did not perform as designed, and ignoring the trigger information and event structure completely allows for the use of an alternative data analysis method.

6.1 Delayed Electron Emissions

The electric fields posed problems in the LUX system during operation. The drift field was initially proposed to have been between 200 V/cm and 1000 V/cm which would require an applied voltage to the cathode of at least −10 kV. The cathode was reviewed and certified to operate correctly with an applied voltage up to −30 kV. However, during the dark matter search period, the voltage applied to the cathode was −10 kV, and could go no lower. Furthermore, unanticipated issues (described below) resulted in the gate voltage to be −1.5 kV, and could not be raised any higher. This caused the drift electric field to be 181 V/cm, lower than the design and possibly affecting detector performance. For instance, the electric field dependence of discrimination between NR and ER events is not very well understood [56, 123].

The limitations on the voltage applied to the gate grid were driven by the anode grid because the drift field is coupled to the extraction field by the gate grid. The anode grid could not be raised to a voltage higher than 3.5 kV without the generation of a spark. One

possible cause is the idea that some debris left from construction fused to the anode when voltage was first applied and provided sharp points for discharge to occur. The exact cause of the anode issue will not be known until such time that the detector is opened for visual inspection.

The electron extraction field, set by the potential difference between the gate and anode grids, in turn determines the electron extraction efficiency. This is a measure of how efficiently ionization electrons from the interaction can be extracted into the gaseous xenon to be accelerated and produce S2 light. Unlike discrimination, the electron extraction efficiency is highly dependent upon the extraction electric field between the gate grid and anode grid. Because of the limitations on the anode voltage, this necessitated lowering the gate grid to increase the extraction field, lowering the drift field in the process. The extraction efficiency during the dark matter search was determined by calibration data, as described in Chapter 5.

The extraction efficiency (55%) was lower than expected ($> 90\%$), resulting in a severe limitation observed in the data, namely that of delayed electron emission. This effect is similar to the electron trapping time discussed in Chapter 3, though that effect occurs on $\mathcal{O}(1\ \mu\text{s})$ timescale and provides the observed S2 pulse width. The delayed electron emissions cause longer periods of time to be dominated by large amounts of activity. Because the extraction efficiency is so low, single electrons tend to remain piled-up at the liquid-gas interface for long periods of time, eventually being extracted one-by-one into the gas to produce electroluminescence light.

The delayed electron emissions observed in data have a very long (or, "slow") component of $\mathcal{O}(10\ \text{ms})$. An example waveform that contains a resolved S2 followed by delayed electron emissions is shown in Figure 6.1. In this figure, each color represents a 1 ms, triggered, event window (see Chapter 2). The initial blue event window contains the "good" S2, and the subsequent events contain electron-like pulses, though there is no clear separation between one electron and the next. The software algorithms used to resolve and characterize individual pulses, known as the pulse finder and pulse classifier, tend to categorize these emissions as "electron-like" pulses if they can be resolved, but in other cases such resolution

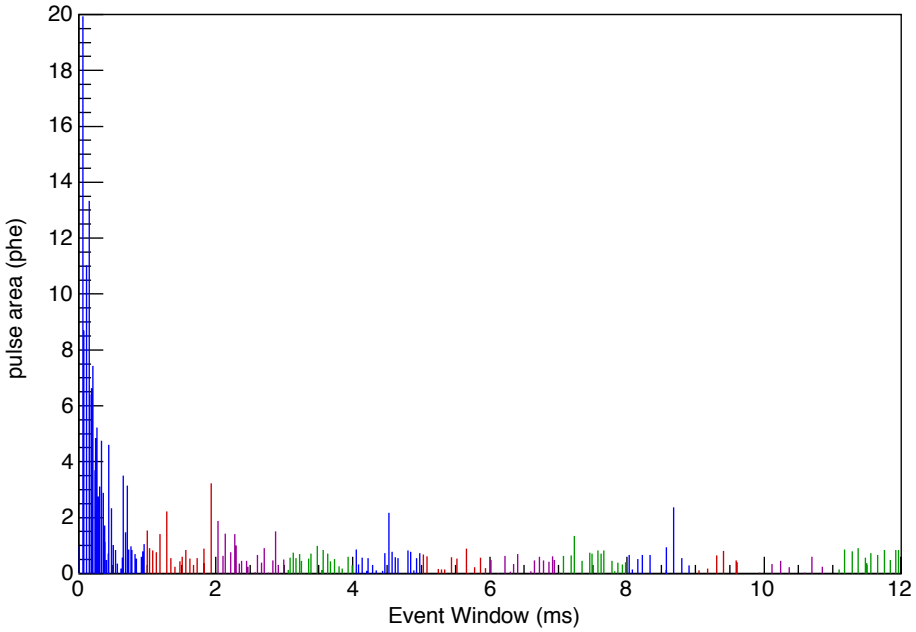

Figure 6.1. This shows the waveform of a resolved S2 (first blue section), followed by a delayed electron emission. Each color represents a 1 ms event window. It is evident that there is no clear break between the "good" S2 and the resulting electrons that are extracted after it. This causes problems as the pulse finder and pulse classifier attempt to differentiate between various pulses. Data like these must be rejected during the analysis.

is not attained, leading to unpredictable characterization. These delayed electron emissions cause serious problems in the data as they represent periods in the time stream that must be rejected. A method looking for regions of low detector activity was developed [124] and used to reject the time periods that contain delayed electron emissions.

6.1.1 Quiet Time

Recall that when LUX data is digitized, all pulses that rise above a certain threshold are recorded, regardless of the trigger information. Only the part of the pulse that is above threshold is digitized, along with 24 preceding clock cycles (or, samples) and 31 trailing ones. The baseline is computed as a rolling average of 128 samples and is also recorded. This method is referred to as Pulse Only Digitization (POD) [83]. The sampling clock is 100 MHz, the digitizer has 14-bit resolution, and the threshold is set at 13 counts. The resulting digitized waveforms in each PMT channel are referred to as PODs. A sum of all the PODs is

made off-line and is known as a SumPOD.

If the trigger information is ignored, the raw data can be studied directly. Periods in time that do not contain delayed electron emissions can be found, and these periods are referred to as "quiet time windows," or QTW. A histogram of SumPOD rate with 1 ms bins is created, as shown in Figure 6.2. As is evident in the figure, during quiet times, the SumPOD rate is ∼2-3 Hz. When the SumPOD rate rises above 10 Hz, the window is no longer quiet and will be removed from the time stream. This noisy time window (NTW) begins when the SumPOD rate rises above 10 Hz and ends when the phe rate falls back to its quiet rate. A correction is applied to the width of the NTW, dependent upon the integrated pulse area per bin, measured in units of photo-electrons per millisecond (phe/ms). One photo-electron of area is defined as the average response of the LUX electronics chain to a single photon detected by a PMT. If the phe rate is > 30 phe/ms, the width of the time window being removed is increased. The additional width is determined to be $\times 5$ the duration for which the sumPOD rate was above 10 Hz. In Figure 6.2, regions in the time stream shaded in purple are the noisy time windows. The noisy time windows are removed from the livetime, resulting in a quiet livetime that is $\sim 12-18\%$ less than the total livetime. While this cut removes a portion of the livetime, it has proven to be effective at removing the delayed electron emissions, thus providing a much cleaner data set.

The effectiveness of QTW is demonstrated in Figure 6.3. The pulse area and pulse width parameter space is described greater detail below, however, it is useful at this juncture to illustrate what is being removed by the quiet time algorithm. In total, 37.2 hours of WIMP search data are included in these plots. Each pulse is classified as per the various regions that are identified as S1, S2, SE, SPE, (defined below) and delayed electron emission, as indicated. Applying the quiet time algorithm removes 5.8 hours from the livetime, or ∼15%. Figure 6.3, *top*, shows the distribution of pulses in the noisy regions. Notice the large population of S2s and Delayed Electron Emissions. Figure 6.3, *bottom*, shows the distribution of pulses in the quiet windows. The S2 and delayed electron emission populations are drastically reduced, indicating that the S2s that were present were coupled with delayed electrons and would not have been usable in a WIMP search. These correspond to the waveform

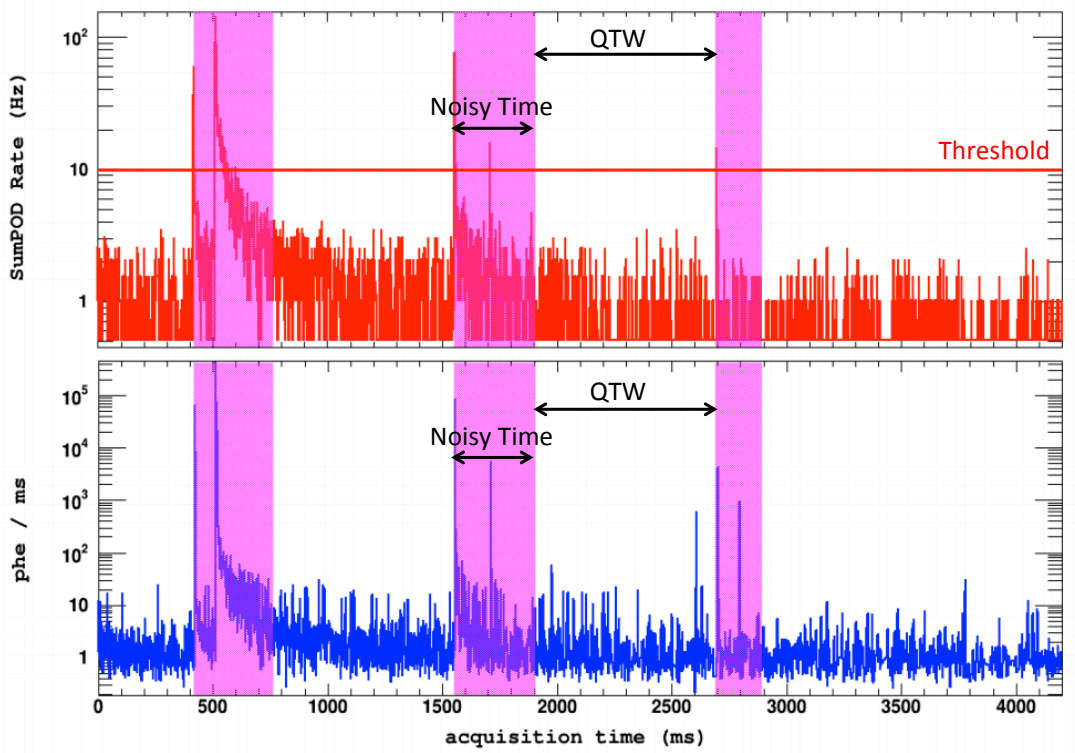

Figure 6.2. The quiet and noisy time windows in LUX data. The regions shaded purple represent time that is removed due to a high event rate (noisy time). See the text for a detailed description of how the width of the removed time is computed.

shown in Figure 6.1. This algorithm removes 99.5% of the delayed electron emissions while retaining ~85% of acceptable livetime.

6.2 Data Processing

After the quiet time windows have been found, the raw data must be processed into a form that can be analyzed. Because the quiet time algorithm operates on the un-triggered data, the trigger information is not used, and the data processing method used to reduce WIMP search data is different than described in Chapter 2. The method involves removing the noisy time windows, applying a pulse finder and pulse classifier to reduce the waveforms to pulses, building events based on the found pulses, and making analysis cuts to further reduce the data until a final result is obtained. The data processing chain, shown in Figure 6.4, will be described in detail in this section.

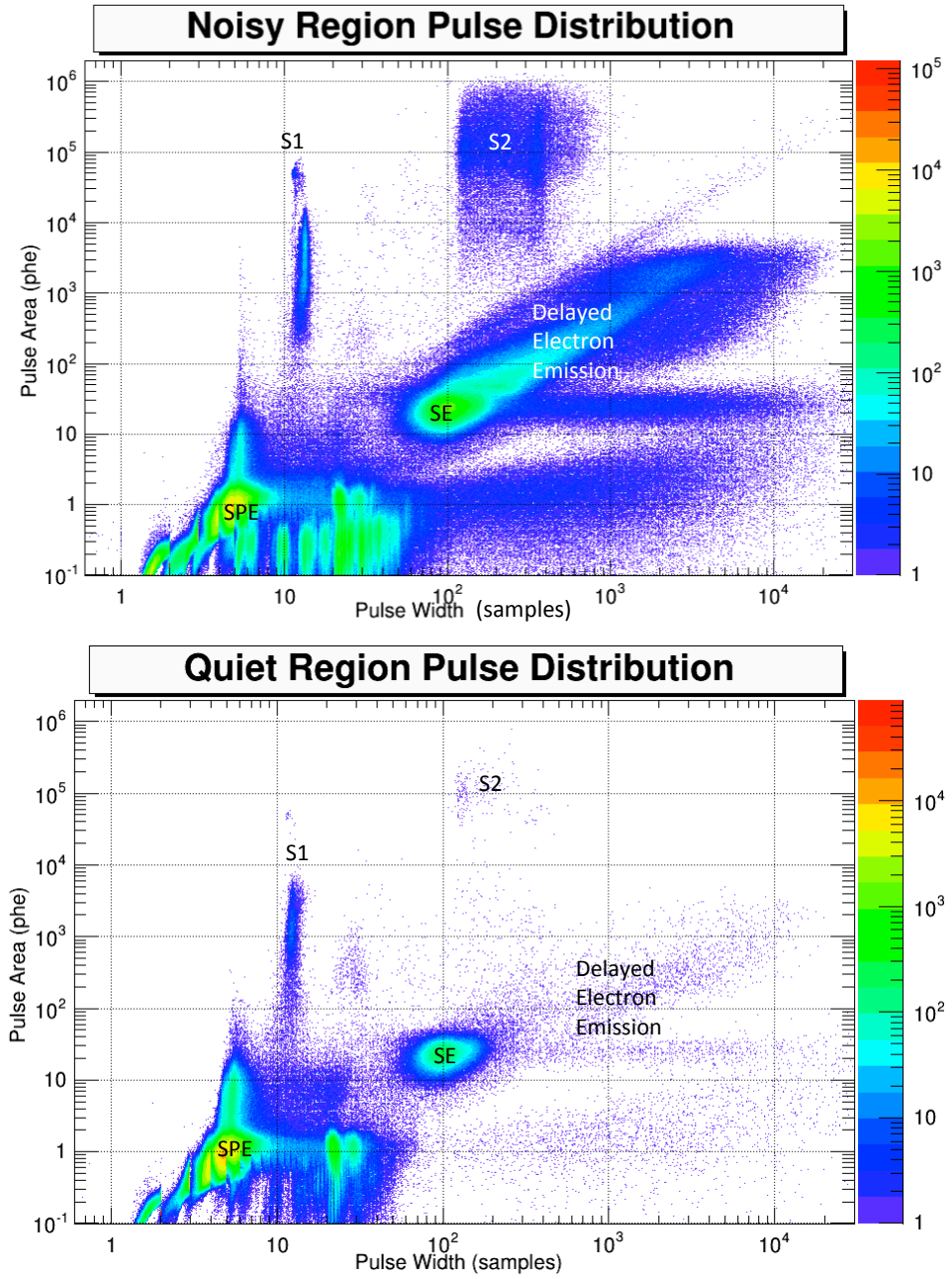

Figure 6.3. 37.2 hours of WIMP search data were studied, and the quiet time algorithm was applied. *top*: The pulse area vs. width distribution for pulses that reside in the noisy windows, accounting for 5.8 hours or 15%. There are large populations of both S2s and delayed electron emissions. *bottom*: The pulse area vs. width distribution for pulses that reside in the quiet time windows. The late populations of both S2s and delayed electron emissions are reduced, indicating the S2s in the noisy time are coupled to delayed electron emissions, so those pulses and events would be unusable. In fact, the quiet time algorithm removes 99.5% of the delayed electron emissions.

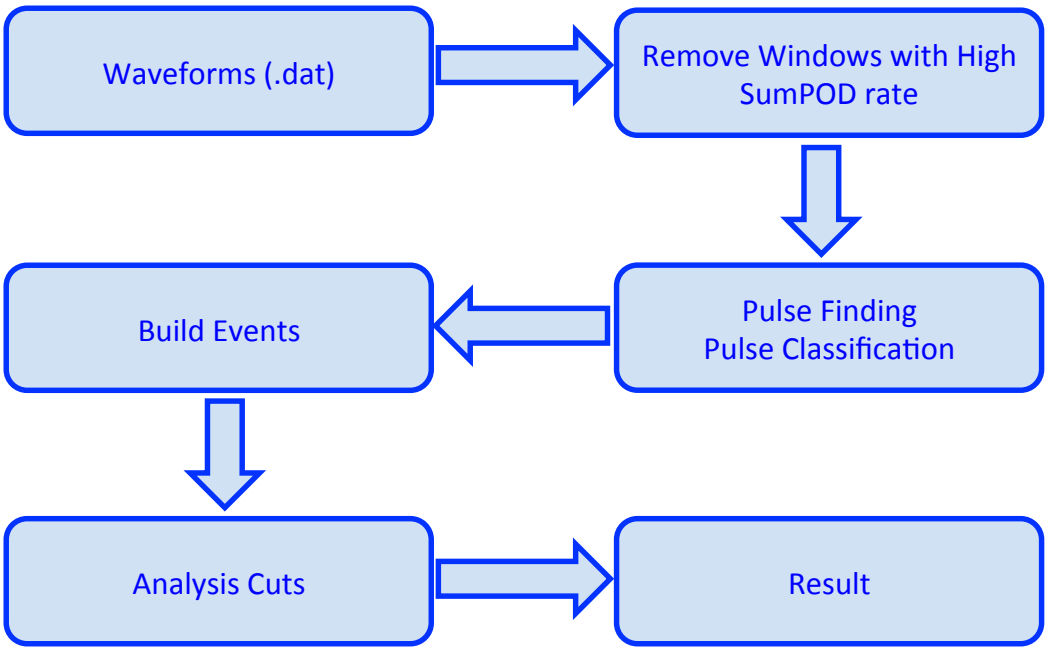

Figure 6.4. The flowchart describing the steps in the data processing chain used for WIMP search data. Raw waveforms first had noisy time windows removed. Then a pulse finder and pulse classifier were applied to reduce the remaining waveforms into pulses. The pulse classifier output was used to scan for S2 pulses, so events could be assembled around them. Finally, analysis cuts were applied to the events, leading to a final result

6.2.1 Pulse Finder and Pulse Classifier

After the noisy time windows have been removed, pulse finding and pulse classifying algorithms are applied to the data, described in detail in [124]. The pulse finder contains six steps: 1.) The waveform is smoothed, keeping the area constant; 2.) Edges of the pulse are located and pulse region defined; 3.) The waveform is further smoothed with a box filter; 4.) Local maxima and minima within the pulse region are found; 5.) Statistical tests are performed to determine whether the pulse region contains more than one pulse; 6.) The pulse borders are adjusted to correct for the distortion due to smoothing. The resolved pulses are then classified by type.

The pulse classifier categorizes the identified pulses based on their area and width (full width at 10% maximum). This parameter space, populated with resolved pulses, is shown in Figure 6.5 to demonstrate the categories. The pulse classification categories are:

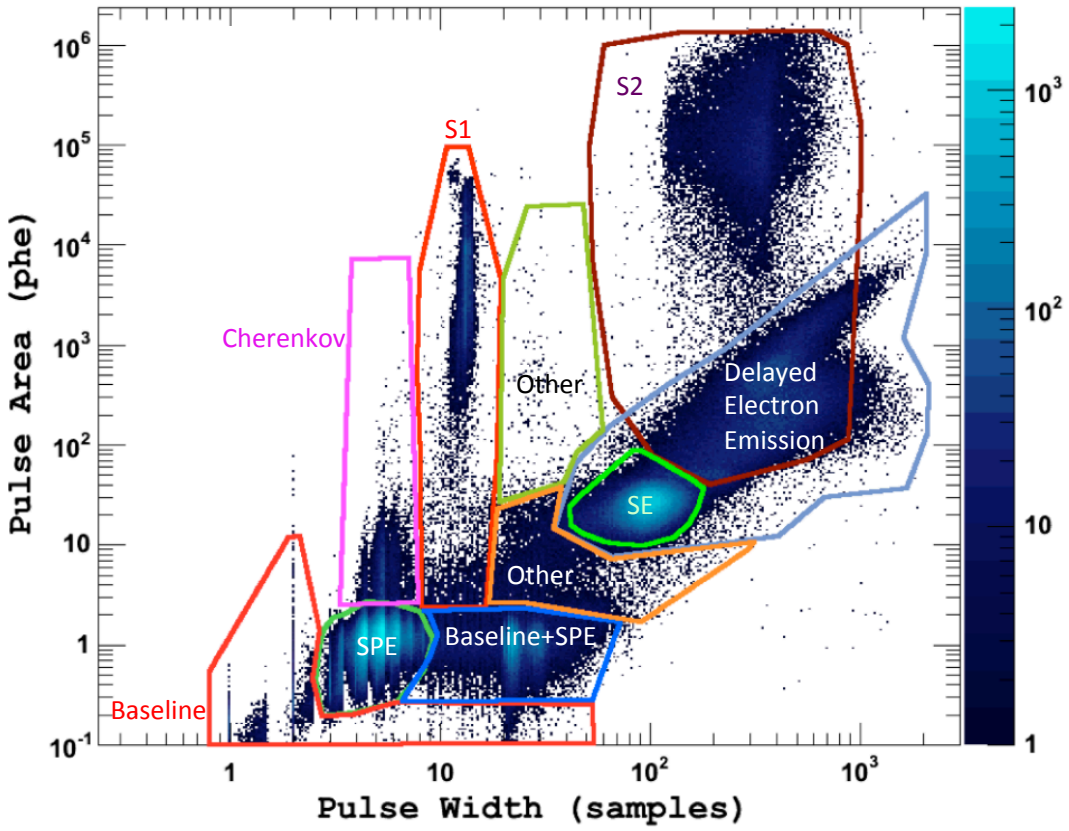

Figure 6.5. The pulse area and pulse width (full width at 10% maximum) parameter space used to classify the resolved pulses as the proper pulse type. Note that one sample is 10 ns.

- Baseline: The region enclosed with a red line contains pulses that have areas well below 1 phe and widths of only a few samples. These pulses are consistent with noise caused by baseline fluctuations.

- Single Photoelectrons (SPE): The SPE region contains pulses with area of ∼1 phe. The single photoelectron rate is ∼1.5 kHz.

- Cherenkov: These pulses are narrower than S1s but have large pulse areas, and nearly all the light is contained in one PMT. These are caused by stray electrons producing Cherenkov radiation in the PMT windows.

- Baseline+SPE: These pulses have areas consistent with SPE, but they have a much larger width. In these pulses, the SPE happened to coincide with a baseline fluctuation noise pulse. These pulses, for the purpose of analysis, are classified as SPE.

- Single Electrons (SE): These pulses are the result of the extraction of a single electron into the gas region to produce an S2-like pulse. They are not coincident necessarily with an interaction as electrons can be spontaneously emitted from the liquid surface [60].

- S1: These pulses are S1s. They are unambiguous and well separated from other categories. S1s with small areas (a few phe) can be resolved from SPE and Cherenkov pulses due to the fact that the classifier requires an S1 pulse to have light present in at least two PMTs.

- S2: The brown box encloses the domain of S2s. The signature is clear for pulses with area greater than 10^3 phe and widths about 1.5—4.5 μs. The pulses with smaller areas and larger widths within the brown box are likely the result of delayed electron emissions.

- Delayed Electron Emissions: These pulses are caused by electrons that are inconsistent with S2 or SE pulses. They can be vetoed using the quiet time algorithm described above.

- Other: Pulses marked as other do not fit into one of the expected categories. They are most likely caused by excessive splitting of pulses within the algorithm.

6.2.2 Gain Calibration

The pulse finder and classifier assumes that the PMTs have identical response to incident light. This is ensured in the data by calibrating the combination of PMTs and the subsequent electronics chain. Their response functions are normalized in terms of the measured pulse area of SPEs. This gain calibration was done for each data acquisition, which typically lasted for about 8 hours, thus providing a large enough independent statistical sample of SPEs. Figure 6.6 shows the relative variation of the gain of each PMT as a function of the day since the start of the WIMP search data. The gains are normalized to be unity on day 10, as shown by the uniform green across all channels. The three white streaks across the plot correspond to the three PMTs in LUX that were deactivated. As is visible, the worse

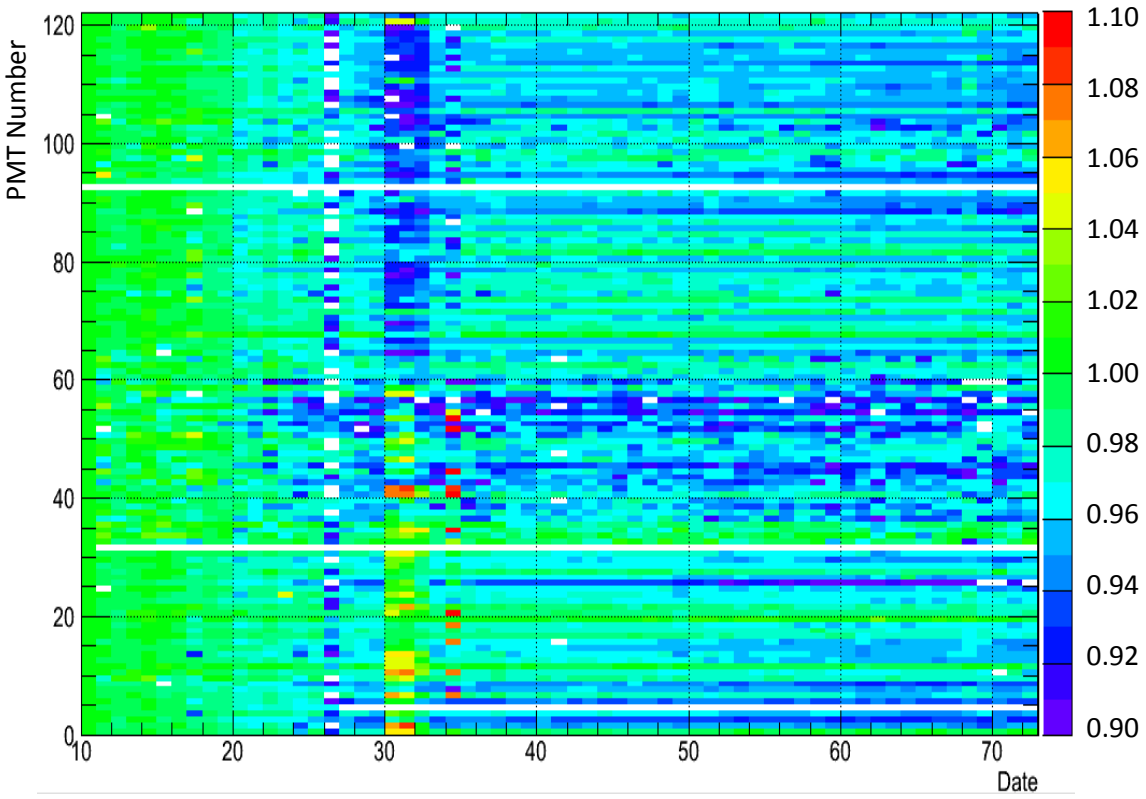

Figure 6.6. A graphical representation of relative PMT gains as a function of time.

excursion from unity is no more than 10% in either direction, while most of the PMTs show much lower variation.

The gains were also measured using light-emitting diodes (LEDs) that were embedded in the detector volume and could be pulsed using external stimuli. This method was employed sporadically through the run, and provided for periodic comparisons to be made with the in-situ method. Figure 6.7 shows the absolute SPE area gains for each PMT, in units of mV-sample, where one sample is 10 ns. The LED method (red) is compared to the in-situ (blue) gains. As can be seen the LED gains have a somewhat larger spread, and there is some disagreement between the two methods as illustrated by the red and blue dashed lines. This difference is used to estimate a systematic error of $\mathcal{O}(6\%)$ in the overall energy scale of LUX. This is treated further in Chapter 7.

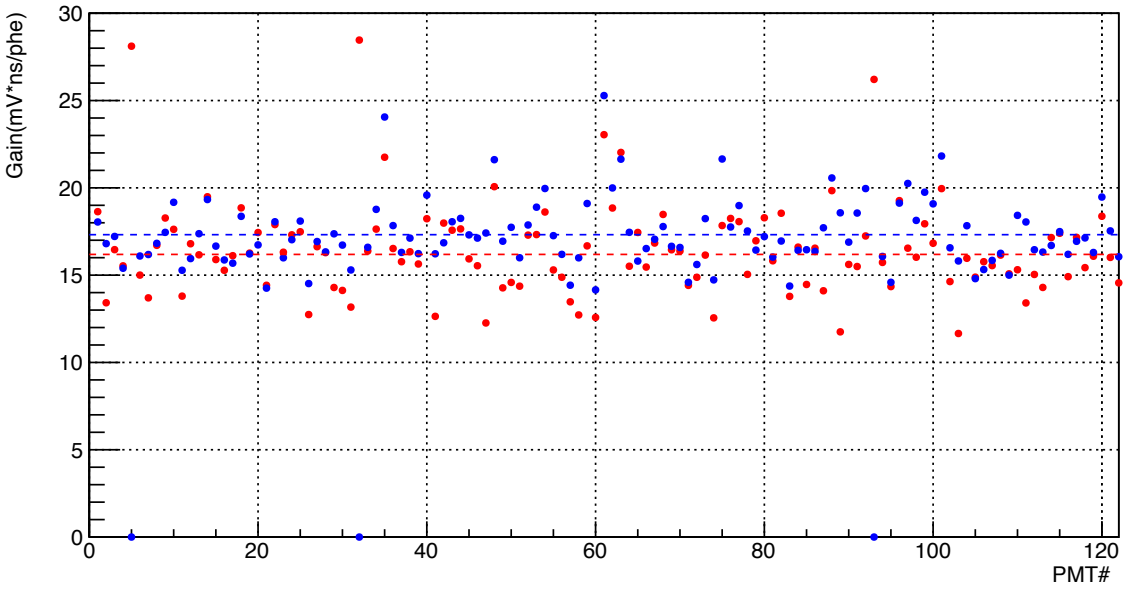

Figure 6.7. Absolute PMT gain in units of mV-sample as a function of PMT number. Two methods were employed for this: in-situ (blue) and LED (red) as explained in the text.

6.2.3 Event Selection

An event consists of pulses that occur within a certain time window, centered around a trigger. Pulses must be grouped into an event-like structure because a "good" event will contain one S1 pulse followed by one S2 pulse. A class of events that could stem from a good interaction will contain events with exactly one S2 preceded by one S1, and events within this class are defined as golden events. Golden events can have additional S1 pulses after the S2 pulse, and they can contain pulses between the S1 and S2, as long as none of those are classified as S1 or S2 pulses.

Because the standard trigger information is ignored for the purpose of applying the quiet time algorithm, a different triggering mechanism was needed to group the pulses of the WIMP search data. Since all golden events must contain an S2, it was decided to use pulses identified as S2s as the trigger. All pulses that occur 350 μs before and after the trigger S2 are grouped into one event, illustrated in Figure 6.8. The time window was chosen because 350 μs is the maximum time an ionization electron can drift in LUX without being extracted into the gas and producing an S2. Looking back 350 μs ensures that an S1 leading to the trigger S2 will be found, and looking forward 350 μs ensures that events which interact in

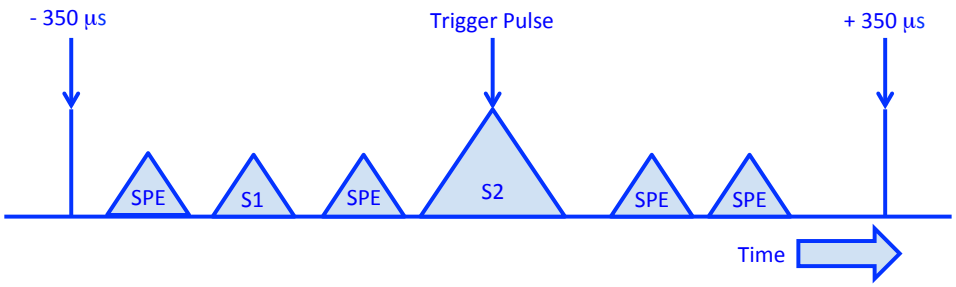

Figure 6.8. An illustration of an event with WIMP search data. An S2 is the trigger. All pulses that occur 350 μs before and after the trigger S2 are grouped into one event. This time is chosen as it is the maximum time electrons can drift in the detector before producing an S2, so events with more than one energy deposition can be identified.

the target more than once, producing multiple S1/S2 pairs will be found as well.

After events are constructed, the data are further reduced with analysis cuts, leading to a result. These cuts and the result are described in Chapter 7.

Chapter 7

Analysis and Results

A scattering of a WIMP off a xenon nucleus is a rare process and represents new physics that has not yet been observed. In order to ensure that the observation of a WIMP interaction has been made, the criteria for WIMP detection must be defined. This is done by establishing a "search region", where the detector performance, calibrations, and background signals are well understood. Any additional signal, significantly beyond what is predicted, then constitutes the discovery of new physics. At the same time, a simple WIMP interaction model is needed in this region to help understand any new physics that might be observed. If no WIMP interaction is observed, the sensitivity of LUX to a potential WIMP interaction of this type can be quantified as a confidence limit on the null result, and then translated into an upper limit on the cross section for such an interaction. Traditionally, this is done as a function of the WIMP mass, because that is the only unknown parameter in an elastic scattering model. In this chapter, the analysis and results of the WIMP search with LUX are presented.

7.1 WIMP Search Region

To observe a WIMP interaction, a well-understood search region must be defined. The WIMP search region used in this analysis is shown in Figure 7.1. The ER and NR discrimination bands in the log(S2/S1) versus S1 plane are shown in blue and red, respectively. Contours of constant energy, as defined by 5.4, are shown in magenta, with the solid curve indicating the 1 keV$_{nr}$ lower bound. The solid black lines encase the region where this analysis will

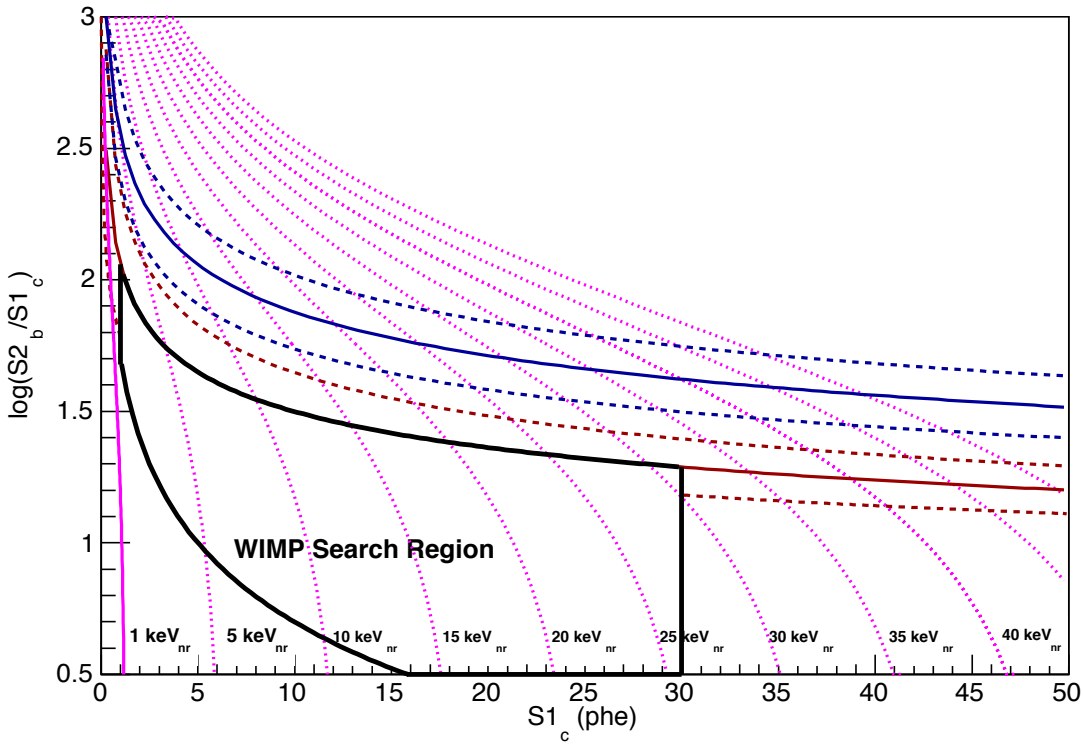

Figure 7.1. The WIMP search region used in this analysis. The blue and red lines indicate the ER and NR bands, respectively, defined by detector calibrations. The magenta lines show lines of constant energy. The WIMP search region is bounded by the solid black lines. To ensure 50% acceptance the NR band mean is the upper bound of the region. This choice results in a 99.95% ER background rejection. The analysis threshold imposed on the size of the S2 defines the lower bound. The left and right bounds are defined by the expected WIMP interaction spectrum.

look for WIMP interactions. WIMPs will scatter off the xenon nucleus, so the search region must accept NR events while rejecting ER backgrounds. The region is bounded from above by the NR band mean, providing an acceptance of 50%, and from below by the analysis threshold imposed on the size of the S2, which will be discussed below.

The search region is bounded on the left and right in terms of $S1_c$. At the low edge, the smallest value of S1 considered is 1 phe. This choice is made in order to have nearly 100% efficiency for the smallest possible detectable S1 pulse, as discussed below. This search region provides an average rejection of ER background events of 99.95%, as was shown in Figure 5.15.

The low-energy neutron calibrations indicate that LUX is sensitive to NR events at energies as low as 1 keV_{nr}, as shown in Figures 5.10 and 5.11. Coincidentally, the chosen lower S1 bound is approximately overlapping with the 1 keV_{nr} contour in Figure 7.1. The upper bound of the WIMP search region is selected to have a value of $S1_c < 30$ phe, which will be motivated in the following section.

7.2 WIMP Signal Generator

To perform a WIMP search, an expected spectrum must be generated for a given WIMP mass. Such a spectrum will be dependent upon the galactic WIMP model chosen, and in this analysis the Standard Halo Model (See Table 1.2) is used. From these assumptions, a WIMP interaction spectrum for the discrimination variable $\log(S2_b/S1_c)$ versus $S1_c$ is straightforward to construct as a function of WIMP mass. Because WIMP interactions result in NR energy depositions, the WIMP spectrum is generated using simulations of NR events. First, a flat spectrum in the recoil energy range of 1—50 keV_{nr} is generated. Next, the WIMP mass-dependent rate, given by (1.13), is used to sample the simulated events and produce the correct signal spectrum. To ensure an adequate population of signal events in the spectrum, a WIMP-nucleon cross-section of 1 pb (10^{-36} cm^2) is assumed. Of course, the WIMP-nucleon cross-section is expected to be much lower than this as current experiments [35] are already sensitive to WIMPs at this level. Figure 7.2, *top*, shows a WIMP spectrum for a 50 GeV WIMP interacting in the LUX detector. As the density of points indicates, a majority (∼85%) of the modeled events are concentrated in the region within $1<S1_c<30$ phe (encased in solid black lines).

The expected signal is highly dependent on the WIMP mass, as demonstrated in Figure 7.2, *bottom*. The expected signal model spectrum is shown for various choices of WIMP mass for illustration. As the mass increases, the number of events with an $S1_c$s larger than 30 phe increases. This is because the area of $S1_c$ is directly related to the energy deposited at the interaction site. This figure also illustrates the overall acceptance for the search region, including the cuts placed on the S2 area. Blue points lie within the search region, and red points lie outside it. The harsh divide at $S1_c = 30$ phe is expected based on the discussion

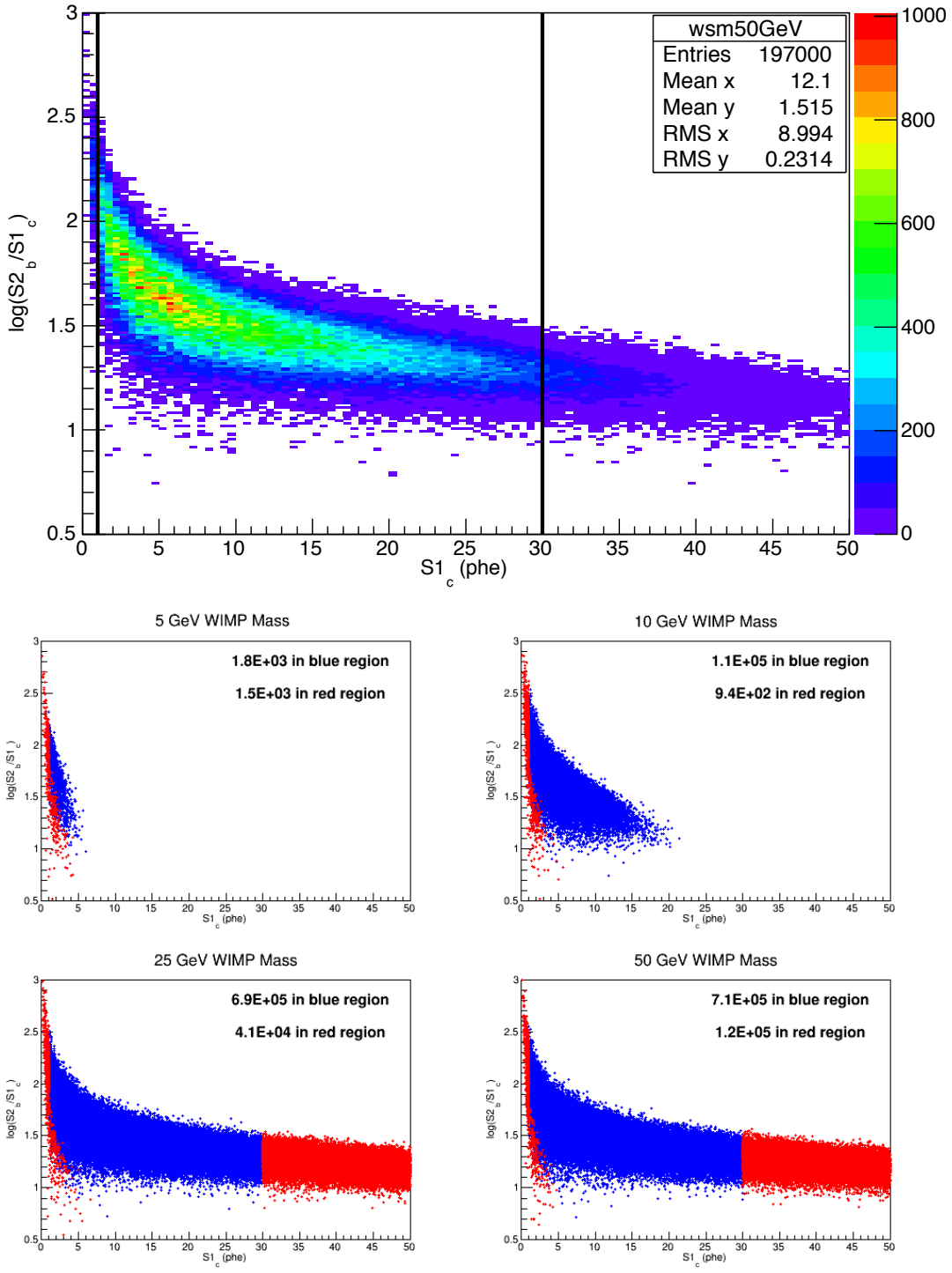

Figure 7.2. *Top*: The signal model for a 50 GeV WIMP interacting in the LUX detector. The procedure for generating this spectrum is described in the text. Approximately >85% of simulated events lie in the region $1<S1_c<30$ phe which is encased in solid black lines. *Bottom*: The generated signal models are shown for several WIMP masses. Blue points indicate those interactions that are within the S1 and S2 area windows defined in the text, and the red points indicate those outside.

above, but the division at ∼1 phe is smeared due to the restrictions imposed on the S2 size, which will be discussed below. These images demonstrate how the WIMP spectrum will change as the mass changes.

7.3 Definitions of WIMP Search Cuts

From April, 2013 until August, 2013, the LUX detector was actively searching for WIMP interactions. The total WIMP search live time during this period was 89.1 days, which excludes any time that a ^{83m}Kr calibration was being conducted. The quiet time algorithm, described in Chapter 6, was applied to the search data to remove periods of high detector activity and the delayed electron emissions. The remaining live time, totaling 77.5 days, was processed according to the procedure in Figure 6.4, and further reduced according to the methods and procedures described in this section.

7.3.1 Multiple Scatter Cut

To completely understand the kinematical behavior and energy deposition of a possible WIMP interaction in the event of a discovery, it is important to reject events that are not well understood. Events that contain more than one S2, referred to as multiple scatter events, can either occur if an incident particle actually scatters more than once in the target, or if two single scatter events overlap in time. Because it is not clear what might have happened in such a case, these events are rejected. Only golden events, those with a single S1 followed by a single S2, (see Figure 6.8) are considered in the WIMP search.

7.3.2 S1 Area Cut

Events with $S1_c$ that fell outside the WIMP search window were also rejected. As described above, the $S1_c$ range was $1<S1_c<30$ phe. The lower threshold is determined to be 1 phe because of the definition of an S1, which must contain light in at least 2 PMTs. However, given the SPE width in LUX is ∼40%, it is possible to have S1s that have smaller areas due to downward fluctuations in the PMT response. For example, consider an S1 made of two SPEs coincident in time in two different PMTs. A modeled distribution of the areas of such S1s is shown in Figure 7.3. As illustrated, a threshold of 1 phe allows 93% of the 2 photon S1s to be detected. The higher threshold of 30 phe is determined by the WIMP spectrum

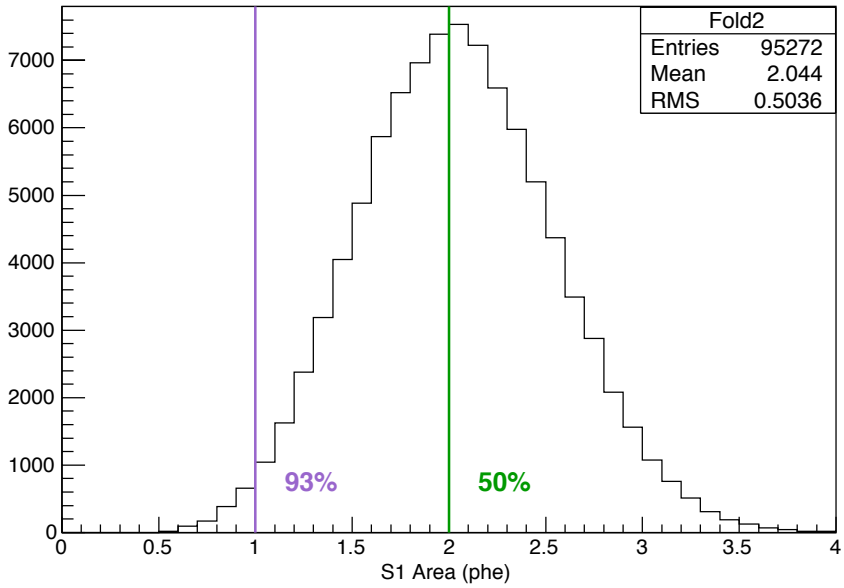

Figure 7.3. A modeled S1 distribution consisting of S1 pulses that are made of 2 SPEs. Because the SPE width is ∼40%, the area of each can fluctuate down such that only half of the 2 photon S1s have an area of at least 2 phe. Reducing the threshold to 1 phe allows for the acceptance of 93% of these S1s.

model. As was discussed above, >85% of the expected events for the 50 GeV WIMP will occur with $1<S1_c<30$ phe.

7.3.3 S2 Area Cut

As was the case with the S1 area, a range was placed on the size of the S2. The S2 area was required to be in the range 100<S2<3300 phe. The lower threshold was motivated by the single electron size. Single electrons can be emitted at the liquid-gas interface, and these pulses could be improperly paired with a random S1 to create a golden event. In order to fully ensure that no accidental pairings from single electrons were admitted into the WIMP search region, a conservative requirement was imposed for all S2s to contain at least 5 electrons, or ∼100 phe. Additionally, a "good" S2 pulse will have a shape similar to the blue curve in Figure 3.8, and certain small S2s do not have that characteristic shape. Further, an upper threshold was imposed to ensure the S2 pulses were physical. The liberal choice of 3300 phe has no impact on the acceptance, while the lower cut of 100 phe removes

a small fraction of WIMP events. These events have an S1 in the range of 1-30 phe but are removed because they have S2s smaller than 100 phe. These are visible in Figure 7.2 as the red points with S1 pulses in the acceptable range.

7.3.4 Fiducial Volume Cut

The ability of LUX to reconstruct events in three dimensions allows for the definition of a fiducial volume, selecting only those events that are away from detector edges or the PMT arrays. Figure 4.7, *bottom*, demonstrates the effectiveness of defining a fiducial volume, wherein the center of the detector has an exponentially suppressed ER background event rate. Establishing a fiducial mass, however, reduces the total target mass of xenon that is considered when searching for WIMPS. The fiducial volume was defined to be cylindrical in shape by considering the drift time (z) and XY position of events.

7.3.4.1 Drift Cut

Aside from isotropic sources of background, the PMT arrays are the largest sources of ER background in the detector. Figure 7.4, which is a histogram of drift time for golden events, is used to determine where the fiducial region in z should be defined. The large clusters of events near drift times of 0 μs and 330 μs are background events and are rejected. In order to ensure that these background events do not leak into the WIMP search region, 24 μs of drift time is removed from the top and bottom of the liquid xenon, as shown by magenta vertical lines in the figure. This corresponds to the range 6.8$< z <$49.7 cm, where $z = 0$ is defined as the top face of the bottom PMT array.

7.3.4.2 Radial Cut

The distribution of the S2 light in the PMTs of the top array allow for the XY position reconstruction of events. The position reconstruction algorithm compares the distribution of light in the PMTs with a library of distributions computed from simulations to best determine the location of the event. Background ER events are more likely to occur near the edges of the detector, thus, a restriction in the radius of an event is necessary to ensure these wall events do not leak in to the WIMP search.

To determine the radius of the cylindrical fiducial volume, the position reconstruction algorithm was applied to simulated events where the actual location of the event is known.

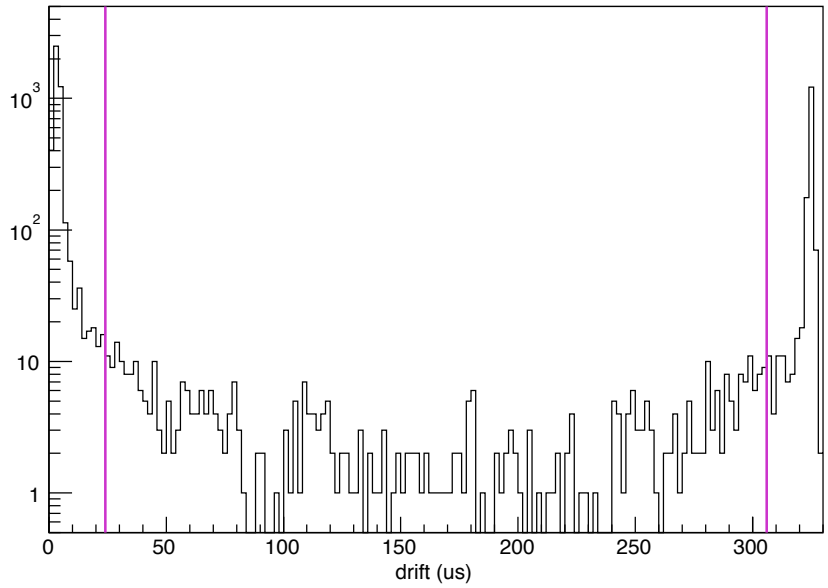

Figure 7.4. A histogram of drift times for golden events. The magenta lines indicate the drift time cut imposed — only events with 24<drift<306 μs are considered in the WIMP search.

The reconstructed radius was compared with the true radius, and a pseudo-efficiency was determined for each r. Figure 7.5 shows the result of this comparison. The number of events reconstructed at each radius was divided by the number of events generated at that radius. The purple vertical lines are located at radii of 15, 16, 17, and 18 cm as a guide. As is evident in the figure, at $r >$18 cm, there is a sharp decline in the efficiency of reconstructed events because the position reconstruction algorithm tends to push these events to the edge of the detector. A fiducial radius should be defined such that the reconstructed vertex position for these events, $r <$ 18 cm. The resolution of the position reconstruction algorithm was computed with the ^{83m}Kr calibration data (see Figure 5.7), and it was found to be 0.7 cm. Moving inward from the sharp decline by $\sim 2\sigma$ would suggest the fiducial radius should be $\sim$16.5 cm, but in order to maximize the fiducial volume, the fiducial radius was chosen to be $r = 17$ cm.

The fiducial volume is thus defined to be a cylinder with radius $r = 17$ cm and a height of 42.9 cm, corresponding to a volume of 3.9×10^4 cm^3. Given that liquid xenon has a density

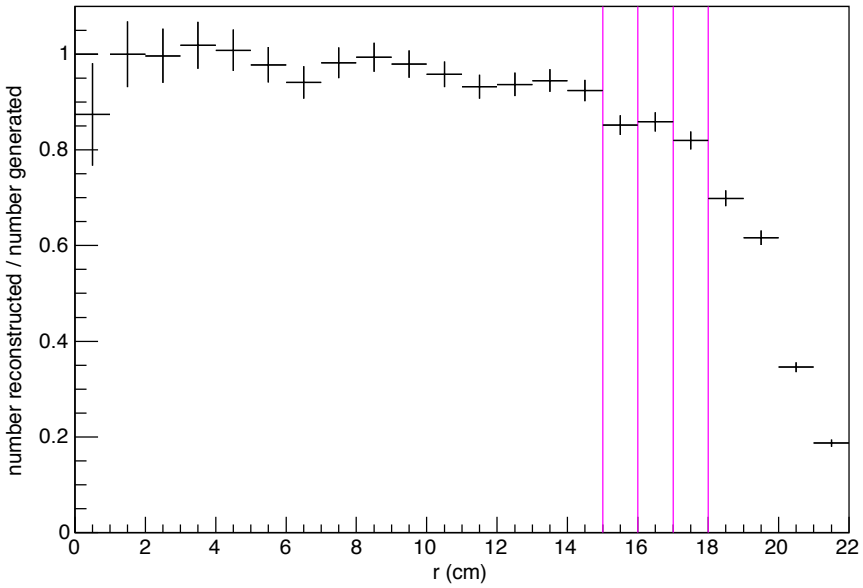

Figure 7.5. The ability of the position reconstruction algorithm was computed by applying the algorithm to simulated events, and comparing the reconstructed location to the generated location. This was done for many events over a range of generated locations. The sharp decline in reconstruction efficiency at r >18 cm suggests that the fiducial radius should be less than 18 cm to avoid adverse effects from the reconstruction algorithm. The fiducial radius was therefore chosen to be r <17 cm to maximize the fiducial volume and avoid this decline.

of 2.888 g/cm^3, the mass of xenon contained within the fiducial volume is 112 kg.

7.3.5 S2 Pulse Shape Cut

In order to suppress any background due to rare errors in the reconstruction and pulse classification software, only events in which the S2 pulse has the expected time profile are retained. As defined below, a further cut is applied for this purpose. The top-bottom asymmetry (TBA) is defined as,

$$TBA = \frac{S2_{top} - S2_{bottom}}{S2_{top} + S2_{bottom}}. \tag{7.1}$$

where $S2_{top}$ refers to the light from the S2 in the top PMT array, and $S2_{bottom}$ is the light in the bottom PMT array. The S2 Area Fraction (AF) is defined as the amount of light in the PMT with the highest light divided by the total area of the pulse. A higher value of AF implies a pulse with very localized light, and a lower value implies a pulse with more

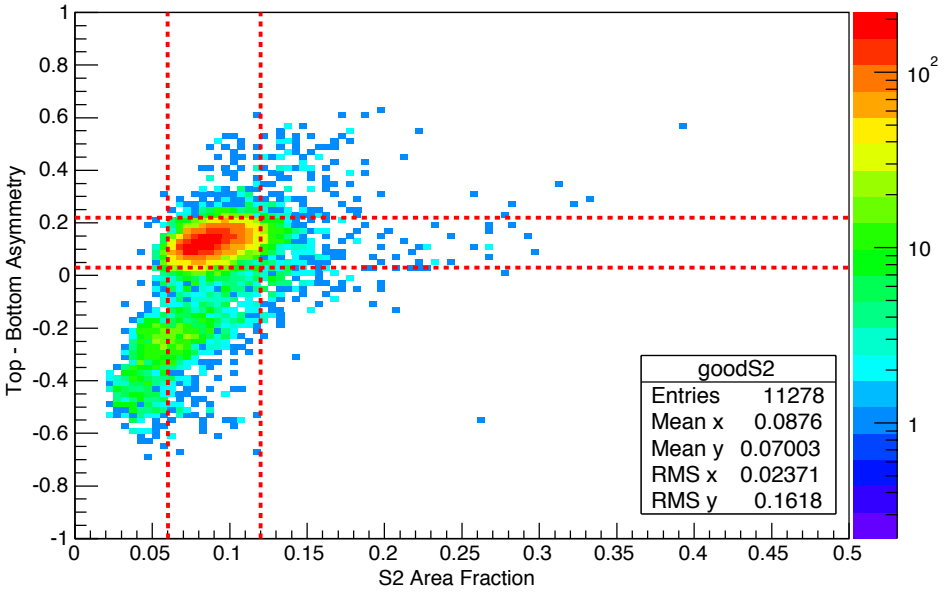

Figure 7.6. The TBA is plotted as a function of S2 area fraction for golden events in tritium calibration data, and a strong population emerges. S2s are considered good if their properties fall within the red box. S2s with properties outside this box are rejected.

distributed light. When TBA in golden events from tritium calibration data are plotted as a function of AF, a striking population emerges, as shown in Figure 7.6.

The high density population from calibration data is used to define a good S2, located within the red box. The TBA must have a value in the range $0.06 < TBA < 0.22$. Events with pulses outside this range include S2s that are either misclassified or are in events that originate in the gas region of the detector [124]. The range of S2 area fraction allowed is $0.06 < AF < 0.12$. S2s with AF values outside this range have very localized light, indicating they occur in the gas, or perhaps as an after pulse in a given PMT.

7.4 Efficiency of WIMP Search Event Selection

Simulated data were used to calculate the efficiency of the cuts applied to the WIMP search data. Simulated events were generated such that each event had exactly one S1 pulse followed by an S2 pulse (golden event). These events were simulated as a function of recoil energy, in the range $0 < E_r < 40$ keV$_{nr}$ with the same number of events generated at each

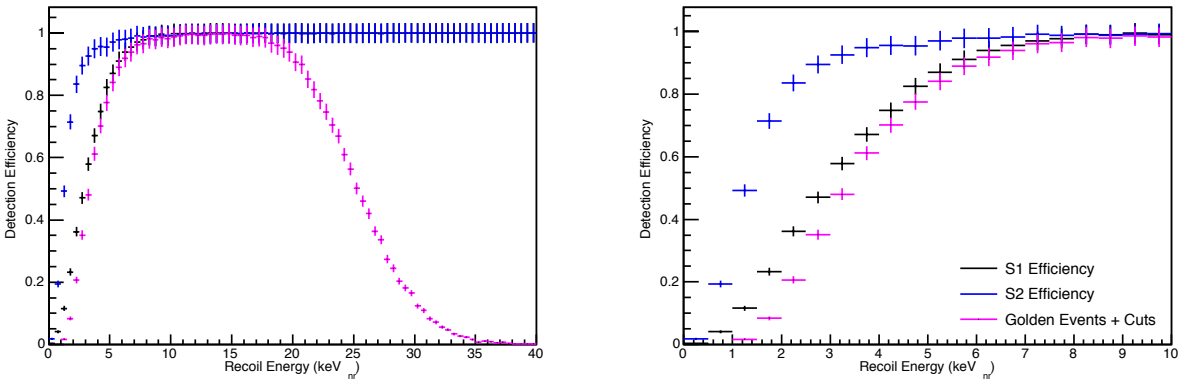

Figure 7.7. *left*: The efficiencies of the pulse finder and pulse classifier to find and resolve S1 and S2 pulses are shown in black and blue, respectively. The magenta curve shows the efficiency×acceptance of all the analysis cuts imposed on the data. These efficiencies were calculated with NR simulation data containing a flat distribution in energy of events with one S1 followed by one S2. The fall-off above 20 keV$_{nr}$ is due to the upper bounds on S1 and S2 areas. *right*: The same efficiency curves are shown for energies in the range 0-10 keV$_{nr}$.

energy. The simulated events were then processed through the same analysis framework to determine the number of golden events found, which could then be directly compared with the number generated. This results in an efficiency as a function of energy.

Three efficiencies were computed: 1.) The S1-only finding efficiency; 2.) The S2-only finding efficiency; 3.) The complete analysis efficiency×acceptance, as shown in Figure 7.7. The left panel shows the entire energy range that was simulated, while the right panel zooms in on the low energy region. The S1-only finding efficiency is defined as the number of events where the pulse finder and pulse classifier resolve one S1 divided by the number of events that contain one S1, as a function of energy. The S2-only finding efficiency is defined in the same way, except the finder/classifier was counting the number of resolved S2s. For the efficiency×acceptance of golden event finding and analysis cuts, the data were processed though the complete analysis chain, and the number of surviving events was compared with the number generated.

The S2-finding efficiency, shown in blue, quickly ascends to unity as S2 pulses are large and distinctive. The S1-finding efficiency, shown in black, rises slowly and around ∼9 keV$_{nr}$ it is nearly 100%. The analysis efficiency, shown in magenta, tracks the S1 efficiency at low

Cut	Events Remaining
Total Events	973,438
Golden Events	698,291
S1 Area (1—30 phe)	30,818
S2 Area (100—3300 phe)	21,914
Drift (24—306 μs)	5,373
Radius ($r < 17$ cm)	108
Good S2	105

Table 7.1. The tabulated results of the analysis cuts applied to the 77.5 live-days of LUX WIMP search data. The list is not commutative, with the order that the cuts are listed in being the order in which they are applied in the analysis.

energies and falls back to zero above ∼20 keV$_{nr}$ when the upper bounds in S1 and S2 areas are reached. It is clear that the efficiency×acceptance achieves 50% at ∼3.5 keV$_{nr}$ and by ∼9 keV$_{nr}$ it reaches its maximum efficiency.

7.5 WIMP Search Data Reduction

The analysis cuts described above were applied to the 77.5 live-days of WIMP search data from LUX, and the results are tabulated in Table 7.1. After applying all cuts, 105 events remain. The final background model from LUXSim presented in Table 4.5 predicted a background rate of $(2.6 \pm 0.2) \times 10^{-3}$ events/kg/keV$_{ee}$/day for ER events. The efficiency for ER is dominated by S1 finding, thus the range 1-30 phe can be converted to an energy range of 0.16-4.87 keV$_{ee}$ using the mean value of the calibration yield of 6.15 phe/keV$_{ee}$ from Figure 5.8. Hence, for a fiducial mass of 112 kg, the predicted ER background is 106 ± 8 events in 77.5 days. This is consistent with the observed number. The ER energy range stated above is clearly an approximation because all the efficiency×acceptance factors have not been applied. However, this exercise is aimed at demonstrating that the observed background is at the level of expectations.

Figure 7.8 shows the distribution of the discrimination variable as a function of $S1_c$ for the remaining 105 events. As can be seen, they appear consistent with the ER band,

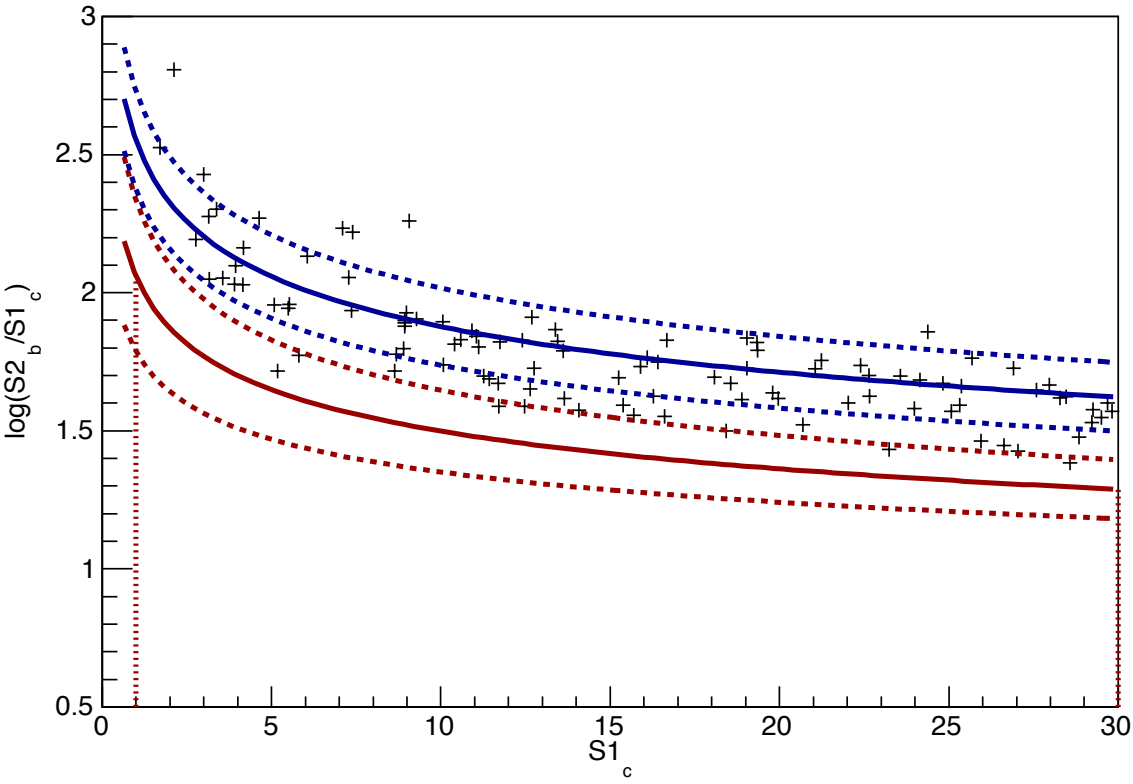

Figure 7.8. Events in the 112 kg fiducial volume during the 77.5 day WIMP search are shown. There are 105 events that remain after the analysis cuts are applied, consistent with the background model prediction of 97 ± 8 events. Each remaining event appears to be consistent with the ER band. There are no events in the WIMP search region, consistent with a null result.

indicating that they are most likely to be ER background events. Clearly, they lie above the WIMP search region which is bounded by the mean of the NR band. Thus, this search yields no WIMP candidate events, and this null result can be converted into an upper limit on the WIMP-nucleon cross section.

Figure 7.9, *top*, shows the interaction site for the remaining 105 events, in terms of the reconstructed drift time and radius squared (r^2). It is evident that the density of remaining events increases as the radius increases, consistent with the increase in target mass which depends on r^2. Figure 7.9, *bottom*, shows the XY spatial distribution for the same events. In both panels, the magenta line represents the boundary of the fiducial volume. The light grey points are events that lie outside the fiducial volume, shown for illustrative purposes.

The high density of events at the detector edges is clearly visible.

7.6 Sensitivity Limit

Since no WIMP signals were observed in the search region, a 90% confidence level upper limit on the sensitivity of LUX to WIMP interactions is instead computed. Two methods are used to compute the sensitivity limit, and because of the absence of signal events, both are expected to produce equivalent results.

7.6.1 Cut and Count

The first procedure considered for quantifying the sensitivity is the so-called cut and count method. In this approach, the data are reduced by the cuts described above, and the number of signal events observed in the WIMP search region is compared with the number of signal events expected, should a WIMP interaction occur. Because a small number of events was expected to be observed, the probability of observation is modeled by a Poisson distribution

$$P(k;\lambda) = \frac{\lambda^k e^{-\lambda}}{k!} \tag{7.2}$$

where k is the number of observed events ($k = 0$) and λ is the number of expected events. Since no events were observed, we compute the value of λ that could have fluctuated to zero with a 10% probability.

$$0.1 = e^{-\lambda} \tag{7.3}$$

$$\lambda = 2.3, \tag{7.4}$$

This interpreted to imply that a maximum of 2.3 events could have occurred but not been detected, with 90% confidence. This can be converted to a sensitivity of the WIMP-nucleon cross section σ_n as follows,

$$\sigma_n = \frac{2.3}{n_e T M_f}. \tag{7.5}$$

where n_e is the expected number of signal events, from the WIMP signal model, T is the live time of the WIMP search, and M_f is the fiducial mass of the detector. The resulting sensitivity of this search is shown in Figure 7.10 as the green curve.

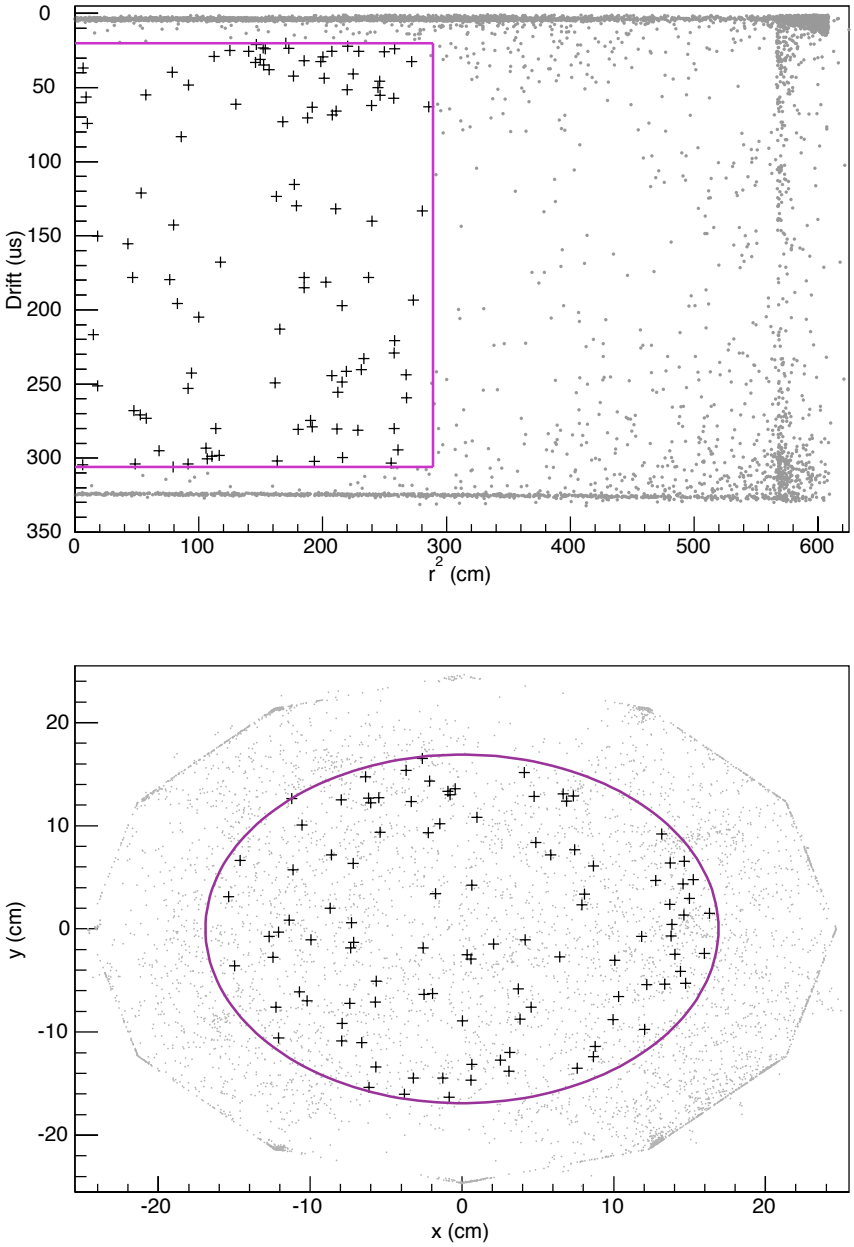

Figure 7.9. The spatial distributions of the remaining events from the 77.5 day WIMP search in the 112 kg fiducial volume. The magenta lines indicate the fiducial volume. The black crosses are the remaining WIMP search ER events, and the grey points are outside the fiducial volume, shown for illustrative purposes. *top*: The distribution of events in r^2 and drift time. It is clear that the remaining events are clustered closer to the edge of the fiducial volume, consistent with the expectation that they are background events leaking in from the detector walls. *bottom*: The XY distribution of events. The remaining events appear to be isotropically distributed in the XY space. The apparent "holes" at $x \sim 0$ and $y \sim \pm 23$ are artifacts of the position reconstruction algorithm.

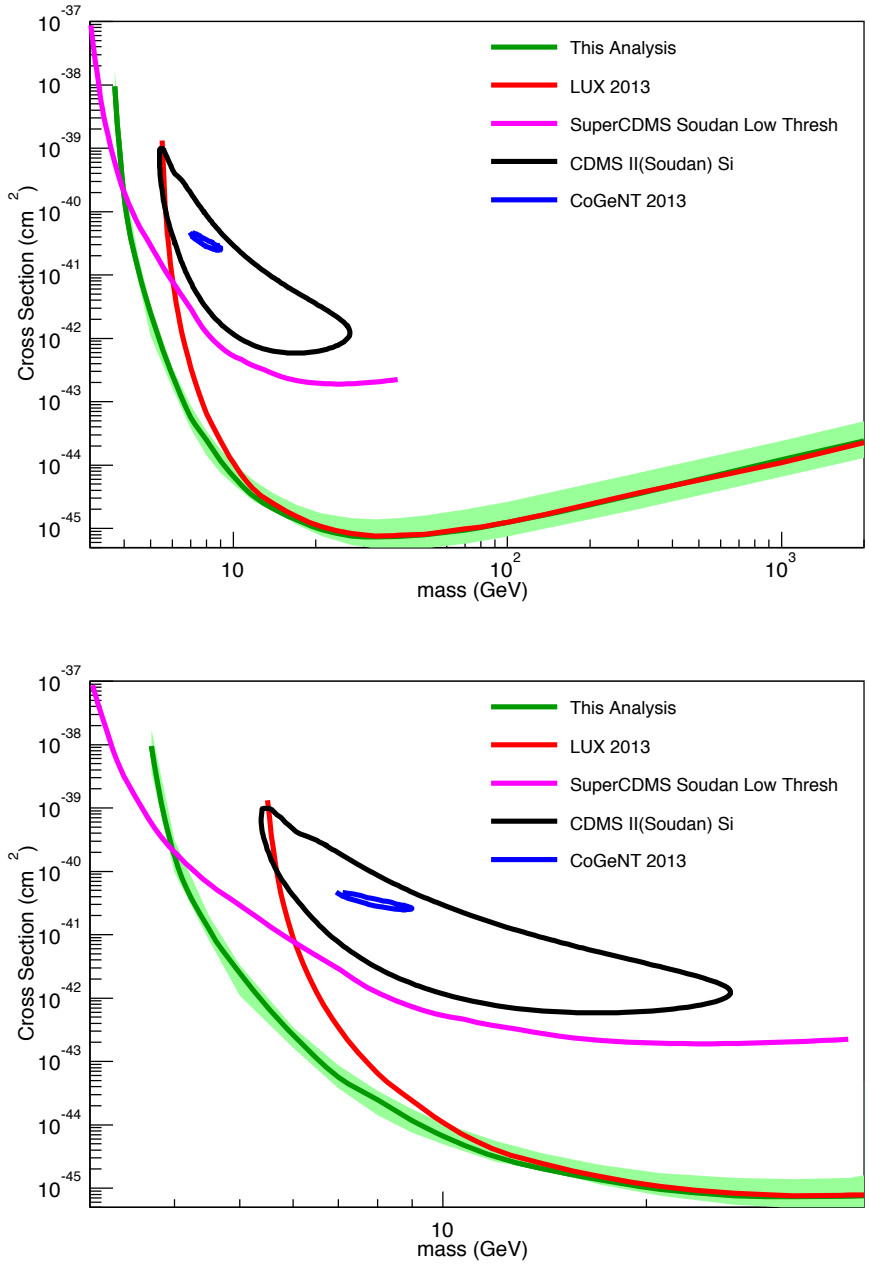

Figure 7.10. *top*: The final limits from this analysis. The results from both the cut and count method and profile likelihood method produce nearly identical results and are shown collectively as the green curve. The LUX 2013 result is shown in red, and other experiments are shown for comparison as well. This analysis extends the sensitivity of the detector to low-mass WIMPs due to the reduction of imposed analysis thresholds and physics model thresholds. These differences are listed in Table 7.2. The green band represents the extent of the limits due to the systematic uncertainties that were considered. *bottom*: The same limits are shown as in the top panel, but zoomed in on the region of low WIMP masses. In this region, this analysis has a greater sensitivity than the LUX 2013 result due to the reduction of the thresholds and physics model, as discussed in the text.

7.6.2 Profile Likelihood Ratio

The 90% confidence level upper limit was also calculated using a frequentist hypothesis test inversion, employing a profile likelihood ratio (PLR) as the test statistic [125, 126]. The unbinned maximum likelihood technique compares the experimental data with a given model on an event-by-event basis. Because this technique allows discrimination utilizing a number of variables that may individually have limited discrimination power, it should be at least as strong as the traditional cut and count approach. The data are the remaining events in LUX, parameterized by the observed quantities $\overrightarrow{x} = (S1, log(S2/S1), r, z)$ (z is simply a recast of the drift).

The signal and background models (M_s and M_b) must be computed in this set of observables. The signal is modeled as described above by the WIMP signal generator and additionally weighted by the detection efficiency (magenta curve in Figure 7.7). The interactions are assumed to be uniformly distributed in r and z. The background model consists of ER events due to Compton scatters arising from radioactive materials in the detector, ^{127}Xe decays, and ^{222}Rn. The model parameters are $\overrightarrow{\theta} = (n_{sig}, n_{Rn}, n_C, n_A)$ where n_{sig} is the number of signal events, n_{Rn} is the number of events from ^{222}Rn, n_C is the number due to Compton scatters, and n_A is the number due to ^{127}Xe decays.

A likelihood function is constructed for the purpose of a likelihood analysis.

$$\mathscr{L}(\overrightarrow{x}) = \left(\prod_i^n p\left(\overrightarrow{x_i} | \overrightarrow{\Theta}\right) \right) \times p\left(n | N_{model}\right) \times p_{constraint}\left(\overrightarrow{\theta} | \overrightarrow{\mu}, \overrightarrow{\sigma}\right). \tag{7.6}$$

As expected, the number of events is Poisson distributed and the constraints are Gaussian in nature.

$$p\left(n | N_{model}\right) = \frac{N^n e^{-N}}{n!} \tag{7.7}$$

$$p_{constraint}\left(\overrightarrow{\theta} | \overrightarrow{\mu}, \overrightarrow{\sigma}\right) = exp\left(\frac{(\sigma - \mu)^2}{2\sigma^2}\right) \tag{7.8}$$

The final component $p(\overrightarrow{x_i} | \overrightarrow{\theta})$ can be defined as

$$p(\overrightarrow{x_i} | \overrightarrow{\theta}) = n_{sig} \times M_s + n_{Rn} \times M_{Rn} + n_C \times M_C + n_A \times M_A \tag{7.9}$$

The background models are fixed according to the LUXSim predictions. n_{sig} is free to float, and n_{Rn}, n_C, and n_A are constrained by the LUXSim model.

A typical test statistic for model like (7.8) with a signal strength parameter of interest σ is the PLR [126]:

$$\lambda(\sigma) = \frac{\mathscr{L}\left(\sigma_{test}, \hat{\hat{\theta}}\right)}{\mathscr{L}\left(\hat{\sigma}, \hat{\theta}\right)} \tag{7.10}$$

where (single) double hats denote (un)constrained maximum likelihood estimators. The numerator is the maximum likelihood given the test cross-section, and the denominator is the global maximum likelihood.

The 90% confidence level is obtained by inverting a series of frequentist hypothesis tests. This procedure is very conveniently facilitated by the RooStats package developed at CERN [127]. A pre-determined number of signal plus background and background only pseudo-experiments were undertaken at test values of N. The PLR is calculated for the data and all the pseudo-experiments. RooStats is used to compare these three PLR distributions and determine the p-value for each assumed mass point. The p-values, in turn, yield the confidence level on the expected value of σ_n. The resulting sensitivity of the PLR analysis is shown in Figure 7.10 as the green curve. It is indistinguishable from the limits arrived at via the cut and count technique, hence the green curve represents the results from both methods.

7.7 Systematic Uncertainty

An estimate was made of the combined effects stemming from several systematic uncertainties. The limits presented in Figure 7.10 can be calculated following the procedure defined by (7.5). In this equation, there can be an error in each of the three quantities in the denominator: the fiducial mass, the total live time, and the number of expected signal events from the WIMP model. The sources of systematic uncertainty in each of the three were considered in this analysis.

First, uncertainty in the total live time, T, can introduce a systematic uncertainty. The total live time is calculated by summing the timing intervals directly from the data acquisition

system. Because the data acquisition system is carefully calibrated and well understood, the errors that arise from summing the individual live time windows to compute the total live time are expected to be negligible.

Next, uncertainty can arise in the calculation of the fiducial mass. The fiducial mass is determined by calculating the amount of liquid xenon contained within a cylinder defined by software algorithms within the bulk liquid xenon. Because the timing resolution of the digitizers is $\mathcal{O}(10)$ ns and the the drift times of ionization electrons are $\mathcal{O}$(10-100) μs, an uncertainty in the fiducial mass from the drift time is again negligible. However, a position reconstruction algorithm is used to determine the location of the event in (r, ϕ), and as is shown in Figure 5.7, the resolution of this algorithm in r is $\pm$0.7 cm. Assuming a variation of that amount, the fiducial mass is 112 ± 10 kg. A larger fiducial mass increases the sensitivity.

Finally, a systematic uncertainty in the number of expected signal events from the WIMP signal model can be introduced. The signal model generator operates by modeling the expected response of LUX to a nuclear recoil event as a function of recoil energy, but the detector observables are in terms of pulse areas. Based on the discussion in Chapter 6, the PMT gain differences are used to estimate a systematic error of 6% in the overall energy scale of LUX. Uncertainty in the energy scale can enter from the S1 size, the S2 size, and the pulse properties derived from these pulse areas, such as the top-bottom asymmetry. The estimated 6% uncertainty accounts for possible systematic errors stemming from any of these sources. To quantify this effect, the pulse areas in the WIMP signal model (e.g. the x-axis in Figure 7.2) are shifted by this amount in both directions, and the number of expected signal events in the WIMP search region is recomputed, as a function of WIMP mass.

Different combinations of these errors were considered in order to maximize the systematic excursions, thereby quantifying the worst-case scenarios. The extent of the errors on the limits are shown in the solid green band in Figure 7.10. The upper bound occurs when the S1 energy scale conversion shifts the simulated S1 areas to larger values and the fiducial volume is lowered to 102 kg. The lower bound occurs when the energy scale conversion shifts the simulated S1 areas to smaller values and the fiducial mass is raised to 120 kg.

	This Analysis	LUX 2013
S1 Area	1-30 phe	2-30 phe
S2 Area	100-3300 phe	200-3300 phe
Drift	24—306 μs	38—304.5 μs
Radius	r < 17 cm	r <18 cm
Fiducial Mass	112 kg	118 kg
Live time	77.5 days	85.3 days

Table 7.2. A comparison between the analysis parameters used in this analysis and those used in LUX 2013.

7.8 Conclusions

As explained above, an upper limit on WIMP-nucleon scattering cross section, σ_n, was obtained as a function of WIMP mass using two techniques that yielded nearly identical results, as shown by the green curve in Figure 7.10. For comparison, the initial LUX result [35] is shown in red and the limits from the low-threshold analysis of SuperCDMS [34] are shown in magenta. The positive claims are shown in black for CDMS II final exposure region [128] and in blue for CoGeNT region [42].

This analysis reports the smallest upper limit on σ_n of 7.43×10^{-46} cm^2 for a WIMP with mass 33 GeV. This is comparable to the LUX 2013 result, however, it still represents the most stringent spin-independent limit to date. There is a sharp decline in sensitivity to lower mass WIMPs due to the recoil energy threshold of the detector. The limits derived in this analysis at low WIMP masses ($\lesssim$10 GeV) are greatly improved compared to the LUX 2013 result because of the extension of the physics models to energies as low as 1 keV$_{nr}$ and the reduction of the analysis thresholds for both S1 and S2 pulses. Further, the limits in the low mass region once again are in contradiction to the CDMS II and CoGeNT claims of positive detection. At the center point ($\sim$8 GeV) of the CoGeNT contour the reported cross section is 3×10^{-41} cm^2, while the LUX 2013 limit is 500× lower. This analysis has increased this disagreement — the limit reported here is 1,500× lower, thus making it even more difficult to reconcile the limits from xenon experiments with detection claims from

cryogenic crystal experiments.

The differences between this analysis and LUX 2013 result are tabulated in Table 7.2. Based on these values, it is expected that, for WIMP masses >50 GeV, the differences in the limits achieved by this analysis compared with the LUX 2013 result should be <5%, which is what is observed, as shown in Figure 7.10. The observed gradual decline in sensitivity to higher mass WIMPs is caused by the SHM WIMP model. Recall that in the model, the WIMP energy density is constant. As the modeled mass of the WIMP increases, the number density will therefore decrease. Fewer expected interactions means a higher limit.

This analysis demonstrates the sensitivity achievable to low-mass dark matter with this type of detector. As a group of more massive (sensitive) similar experiments comes online in the next decade, the WIMP sensitivity should only increase. However, larger experiments will have poorer light collection efficiency and will deploy more PMTs. Having additional PMTs increases the probability of random SPEs coinciding in time to form a fake S1-like pulse. This coupled with the poorer light collection efficiency might require an S1 threshold much higher than what was achieved here. Hence, such low-mass WIMP sensitivity might not be possible with the next generation of noble liquid experiments. A suite of new experiments utilizing various target masses, however, working together can achieve WIMP sensitivities far greater, and such experiments will become operational within the decade. The future of dark matter search experiments seems promising.

REFERENCES

[1] F. Zwicky. On the masses of nebulae and of clusters of nebulae. *The Astrophysical Journal*, 86(3):pages 217–246, October 1937.

[2] K. G. Begeman, A. H. Broeils, and R. H. Sanders. Extended rotation curves of spiral galaxies - Dark haloes and modified dynamics. *MNRAS*, 249:pages 523–537, April 1991.

[3] V. Rubin. Dark matter in spiral galaxies. *Scientific American*, 248(108):pages 96–106, June 1983.

[4] P. Kroupa, M. Pawlowski, and M. Milgrom. The failures of the standard model of cosmology require a new paradigm. *Int.J.Mod.Phys.*, D21:page 1230003, 2012. e-Print: 1301.3907.

[5] D. Clowe, M. Bradač, *et al.* A Direct Empirical Proof of the Existence of Dark Matter. *The Astrophysical Journal*, 648:pages L109–L113, September 2006. e-Print: astro-ph/0608407.

[6] L. Bergstrom. Nonbaryonic dark matter: Observational evidence and detection methods. *Rept.Prog.Phys.*, 63:page 793, 2000. e-Print: hep-ph/0002126.

[7] B. Ryden. *Introduction to Cosmology*. Addison Wesley, 2003.

[8] A. A. Penzias and R. W. Wilson. A Measurement of Excess Antenna Temperature at 4080 Mc/s. *ApJ*, 142:pages 419–421, July 1965.

[9] P. Ade *et al.* Planck 2013 results. XVI. Cosmological parameters. 2013. e-Print: 1303.5076.

[10] A. Liddle. *An Introduction to Modern Cosmology (2nd ed.)*. Wiley, 2003.

[11] J. R. Primack. Dark Matter and Galaxy Formation. In F. Roig, D. Lopes, *et al.*, editors, *American Institute of Physics Conference Series*, volume 1192 of *American Institute of Physics Conference Series*, pages 101–137. December 2009. e-Print: 0909.2021.

[12] J. Beringer *et al.* Review of Particle Physics (RPP). *Phys.Rev.*, D86:page 010001, 2012.

[13] S. Tremaine and J. E. Gunn. Dynamical role of light neutral leptons in cosmology. *Phys. Rev. Lett.*, 42:pages 407–410, Feb 1979. URL: http://link.aps.org/doi/10.1103/PhysRevLett.42.407.

[14] K. Carignan, C. Freeman. Ddo 154 - a 'dark' galaxy? *The Astrophysical Journal*, 332:page L33, 1988.

[15] O. Gerhard and D. Spergel. Dwarf spheroidal galaxies and the mass of the neutrino. *Astrophysical Journal Letters*, 389(1 PART 2):pages L9–L11, 1993. URL: http://www.scopus.com/inward/record.url?eid=2-s2.0-4244069431&partnerID=40&md5=76ab839a8b1c8f9c7b82c1d750064560. Cited By (since 1996)20.

[16] A. Kusenko. Sterile neutrinos: The Dark side of the light fermions. *Phys.Rept.*, 481:pages 1–28, 2009. e-Print: 0906.2968.

[17] S. Dodelson and L. M. Widrow. Sterile-neutrinos as dark matter. *Phys.Rev.Lett.*, 72:pages 17–20, 1994. e-Print: hep-ph/9303287.

[18] T. Asaka, M. Laine, and M. Shaposhnikov. On the hadronic contribution to sterile neutrino production. *JHEP*, 0606:page 053, 2006. e-Print: hep-ph/0605209.

[19] A. Kusenko. Sterile neutrinos, dark matter, and the pulsar velocities in models with a Higgs singlet. *Phys.Rev.Lett.*, 97:page 241301, 2006. e-Print: hep-ph/0609081.

[20] A. Carbone. A search for time-integrated CP violation in $D^{0} \rightarrow h^{-}h^{+}$ decays. *ArXiv e-prints*, October 2012. e-Print: 1210.8257.

[21] B. Aubert, D. Boutigny, *et al.* Measurement of *CP*-violating asymmetries in b^0 decays to *CP* eigenstates. *Phys. Rev. Lett.*, 86:pages 2515–2522, Mar 2001. URL: http://link.aps.org/doi/10.1103/PhysRevLett.86.2515.

[22] H. Murayama, G. Raffelt, *et al.* Axions and other very light bosons: in Review of Particle Physics (RPP 1998). *Eur.Phys.J.*, C3:pages 264–271, 1998.

[23] C. Hagmann, D. Kinion, *et al.* Results from a high-sensitivity search for cosmic axions. *Phys. Rev. Lett.*, 80:pages 2043–2046, Mar 1998. URL: http://link.aps.org/doi/10.1103/PhysRevLett.80.2043.

[24] I. Ogawa, S. Matsuki, and K. Yamamoto. Interactions of cosmic axions with Rydberg atoms in resonant cavities via the Primakoff process. *Phys.Rev.*, D53:pages 1740–1744, 1996.

[25] R. J. Scherrer and M. S. Turner. On the Relic, Cosmic Abundance of Stable Weakly Interacting Massive Particles. *Phys.Rev.*, D33:page 1585, 1986.

[26] G. Jungman, M. Kamionkowski, and K. Griest. Supersymmetric dark matter. *Phys.Rept.*, 267:pages 195–373, 1996. e-Print: hep-ph/9506380.

[27] J. F. Navarro, C. S. Frenk, and S. D. M. White. The Structure of Cold Dark Matter Halos. *ApJ*, 462:page 563, May 1996. e-Print: astro-ph/9508025.

[28] C. McCabe. Astrophysical uncertainties of dark matter direct detection experiments. *Phys. Rev. D*, 82:page 023530, Jul 2010. URL: http://link.aps.org/doi/10.1103/PhysRevD.82.023530.

[29] D. Bauer, J. Buckley, *et al.* Dark Matter in the Coming Decade: Complementary Paths to Discovery and Beyond. 2013. e-Print: 1305.1605.

[30] M. Aguilar *et al.* First Result from the Alpha Magnetic Spectrometer on the International Space Station: Precision Measurement of the Positron Fraction in Primary Cosmic Rays of 0.5–350 GeV. *Phys.Rev.Lett.*, 110:page 141102, 2013.

[31] IceCube Collaboration, M. G. Aartsen, *et al.* Multipole analysis of IceCube data to search for dark matter accumulated in the Galactic halo. *ArXiv e-prints*, June 2014. e-Print: 1406.6868.

[32] A. Askew, S. Chauhan, *et al.* Searching for Dark Matter at Hadron Colliders. 2014. e-Print: 1406.5662.

[33] R. Gaitskell. Direct detection of dark matter. *Ann.Rev.Nucl.Part.Sci.*, 54:pages 315–359, 2004.

[34] R. Agnese, A. J. Anderson, *et al.* Search for Low-Mass Weakly Interacting Massive Particles with SuperCDMS. *Physical Review Letters*, 112(24):241302, June 2014. e-Print: 1402.7137.

[35] D. Akerib *et al.* First results from the LUX dark matter experiment at the Sanford Underground Research Facility. *Phys.Rev.Lett.*, 112:page 091303, 2014. e-Print: 1310.8214.

[36] R. Schnee. Introduction to dark matter experiments. *Nucl. Instrum. Meth.*, 2011. e-Print: 1101.5205.

[37] S. Archambault, F. Aubin, *et al.* Dark Matter Spin-Dependent Limits for WIMP Interactions on F-19 by PICASSO. *Phys.Lett.*, B682:pages 185–192, 2009. e-Print: 0907.0307.

[38] R. Bernabei *et al.* First results from DAMA/LIBRA and the combined results with DAMA/NaI. *Eur.Phys.J.*, C56:pages 333–355, 2008. e-Print: 0804.2741.

[39] C. Savage, G. Gelmini, *et al.* Compatibility of DAMA/LIBRA dark matter detection with other searches. *JCAP*, 0904:page 010, 2009. e-Print: 0808.3607.

[40] G. Angloher, M. Bauer, *et al.* Results from 730 kg days of the CRESST-II Dark Matter search. *European Physical Journal C*, 72:1971, April 2012. e-Print: 1109.0702.

[41] R. Agnese *et al.* Silicon Detector Dark Matter Results from the Final Exposure of CDMS II. *Phys.Rev.Lett.*, 111:page 251301, 2013. e-Print: 1304.4279.

[42] C. E. Aalseth, P. S. Barbeau, *et al.* CoGeNT: A search for low-mass dark matter using p-type point contact germanium detectors. *Phys. Rev. D*, 88(1):012002, July 2013. e-Print: 1208.5737.

[43] V. Chepel and H. Araújo. Liquid noble gas detectors for low energy particle physics. *Journal of Instrumentation*, 8:R04001, April 2013. e-Print: 1207.2292.

[44] J. Lewin and P. Smith. Review of mathematics, numerical factors, and corrections for dark matter experiments based on elastic nuclear recoil. *Astropart.Phys.*, 6:pages 87–112, 1996.

[45] G. Hutchinson. Ionization in liquid and solid argon. *Nature*, 162:pages 610–611, 1948.

[46] J. H. Marshall. A liquid argon ionization chamber measurement of the shape of the beta-ray spectrum of k^{40}. *Phys. Rev.*, 91:pages 905–909, Aug 1953. URL: http://link.aps.org/doi/10.1103/PhysRev.91.905.

[47] J. A. Northrop and R. Nobles. Some aspects of gas scintillation counters. *Nuclear Science, IRE Transactions on*, 3(4):pages 59–61, Nov 1956. ISSN 0096-2015.

[48] J. A. Northrop, J. M. Gursky, and A. E. Johnsrud. Further work with noble element scintillators. *Nuclear Science, IRE Transactions on*, 5(3):pages 81–87, Dec 1958. ISSN 0096-2015.

[49] E. Aprile and T. Doke. Liquid xenon detectors for particle physics and astrophysics. *Rev. Mod. Phys.*, 82:pages 2053–2097, Jul 2010. URL: http://link.aps.org/doi/10.1103/RevModPhys.82.2053.

[50] M. Chadwick, P. Obložinský, *et al.* Endf/b-vii.0: Next generation evaluated nuclear data library for nuclear science and technology. *Nuclear Data Sheets*, 107(12):pages 2931 – 3060, 2006. ISSN 0090-3752. URL: http://www.sciencedirect.com/science/article/pii/S0090375206000871. Evaluated Nuclear Data File ENDF/B-VII.0.

[51] P. Sorensen and C. E. Dahl. Nuclear recoil energy scale in liquid xenon with application to the direct detection of dark matter. *Phys.Rev.*, D83:page 063501, 2011. e-Print: 1101.6080.

[52] E. A. A. B. A. B. T. Doke. *Noble Gas Detectors*. Wiley-VCH, 2006.

[53] T. Takahashi *et al.* Average energy expended per ion pair in liquid xenon. *Phys. Rev. A*, 12:page 1771, 1975.

[54] M. Miyajima *et al.* Average energy expended per ion pair in liquid argon. *Phys. Rev. A*, 9:page 1438, 1974.

[55] M. Szydagis, N. Barry, *et al.* NEST: A Comprehensive Model for Scintillation Yield in Liquid Xenon. *JINST*, 6:page P10002, 2011. e-Print: 1106.1613.

[56] C. E. Dahl. *The physics of background discrimination in liquid xenon, and first results from Xenon10 in the hunt for WIMP dark matter. The physics of background discrimination in liquid xenon, and first results from Xenon10 in the hunt for WIMP dark matter. The physics of background discrimination in liquid xenon, and first results from Xenon10 in the hunt for WIMP dark matter. The physics of background discrimination in liquid xenon, and first results from Xenon10 in the hunt for WIMP dark matter*. Ph.D. thesis, Princeton University, 2009.

[57] S. Kubota, M. Hishida, *et al.* Dynamical behavior of free electrons in the recombination process in liquid argon, krypton, and xenon. *Phys. Rev. B*, 20:page 3486, 1979.

[58] J. V. Dawson *et al.* A study of the scintillation induced by alpha particles and gamma rays in liquid xenon in an electric field. *Nucl. Instrum. Meth.*, A545:page 690, 2005. e-Print: arXiv:physics/0502026.

[59] C. Monteiro, L. Fernandes, *et al.* Secondary Scintillation Yield in Pure Xenon. *JINST*, 2:page P05001, 2007. e-Print: physics/0702142.

[60] E. Gushchin, A. Kruglov, and I. Obodovskil. Electron dynamics in condensed argon and xenon. *Sov. Phys. JETP*, 1982.

[61] L. Miller, S. Howe, and W. Spear. Charge Transport in Solid and Liquid Ar, Kr, and Xe. *Phys.Rev.*, 166:pages 871–878, 1968.

[62] E. Shibamura, A. Hitachi, *et al.* Drift velocities of electrons, saturation characteristics of ionization and W-values for conversion electrons in liquid argon, liquid argon-gas mixtures and liquid xenon. *Nucl.Instrum.Meth.*, 131:pages 249–258, 1975.

[63] E. Morikawa, R. Reininger, *et al.* Argon, krypton, and xenon excimer luminescence: From the dilute gas to the condensed phase. *J. Chem. Phys.*, 91:page 1469, 1989.

[64] P. K. Leichner, K. F. Palmer, *et al.* Two- and three-body collision coefficients for Xe($^3p_1$) and Xe($^3p_2$) atoms and radiative lifetime of the $xe_2(1_u)$ molecule. *Phys. Rev. A*, 13:pages 1787–1792, May 1976. URL: `http://link.aps.org/doi/10.1103/PhysRevA.13.1787`.

[65] F. K. S. J. W. Keto, R. E. Gleason. Exciton lifetimes in electron beam excited condensed phases of argon and xenon. *J. Chem. Phys.*, 71:page 2676, 1979.

[66] P. Millet, A. Birot, *et al.* Time resolved study of the uv and near uv continuums of xenon. *The Journal of Chemical Physics*, 69(1):pages 92–97, 1978. URL: `http://link.aip.org/link/?JCP/69/92/1`.

[67] H. D. Wenck, M. C. Castex, *et al.* In *Proceedings of the 6th International Conference on VUV Radiation Physics (unpublished)*. Charlottesville, Virginia, 1980.

[68] G. Thornton, E. D. Poliakoff, *et al.* Fluorescence decay of the o[sup +][sub u] and 1[sub u] states of xe[sub 2]. *The Journal of Chemical Physics*, 71(1):pages 133–139, 1979. URL: `http://link.aip.org/link/?JCP/71/133/1`.

[69] T. D. Bonifield, F. H. K. Rambow, *et al.* Time resolved spectroscopy of xenon excimers excited by synchrotron radiation. *The Journal of Chemical Physics*, 72(5):pages 2914–2924, 1980. URL: `http://link.aip.org/link/?JCP/72/2914/1`.

[70] P. Moutard, L. J.-L., *et al.* Pressure effects on kinetics and decay processes in xenon after selective photoexcitation. *J.Chem.Phys.*, 1988.

[71] Y. Salamero. *ThÂŔse d'Etat*. Ph.D. thesis, UniversitÂŐ Pual Sabatier, 1984.

[72] H. A. Koehler, L. J. Ferderber, *et al.* Vacuum-ultraviolet emission from high-pressure xenon and argon excited by high-current relativistic electron beams. *Phys. Rev. A*, 9:pages 768–781, Feb 1974. URL: http://link.aps.org/doi/10.1103/PhysRevA.9.768.

[73] P. Sorensen. Anisotropic diffusion of electrons in liquid xenon with application to improving the sensitivity of direct dark matter searches. *Nucl.Instrum.Meth.*, A635:pages 41–43, 2011. e-Print: 1102.2865.

[74] E. Aprile *et al.* First dark matter results from the XENON100 experiment. *Phys. Rev. Lett.*, 105:page 131302, 2010.

[75] E. Aprile *et al.* Design and performance of the XENON10 dark matter experiment. *Astropart. Phys.*, 34:page 679, 2011. e-Print: 1001.2834.

[76] D. Akerib *et al.* Technical Results from the Surface Run of the LUX Dark Matter Experiment. *Astropart.Phys.*, 45:pages 34–43, 2013. e-Print: 1210.4569.

[77] J. Angle, E. Aprile, *et al.* First results from the xenon10 dark matter experiment at the gran sasso national laboratory. *Phys. Rev. Lett.*, 100:page 021303, Jan 2008. URL: http://link.aps.org/doi/10.1103/PhysRevLett.100.021303.

[78] T. Shutt, C. E. Dahl, *et al.* Performance and Fundamental Processes at Low Energy in a Two-Phase Liquid Xenon Dark Matter Detector. *Nucl.Instrum.Meth.*, A579:pages 451–453, 2007. e-Print: astro-ph/0608137.

[79] D. Barker, D.-M. Mei, and C. Zhang. Muon-induced background study for an argon-based long baseline neutrino experiment. *Phys. Rev. D*, 86(5):054001, September 2012. e-Print: 1202.5000.

[80] D. S. Akerib, X. Bai, *et al.* Radio-assay of Titanium samples for the LUX Experiment. *ArXiv e-prints*, December 2011. e-Print: 1112.1376.

[81] D. Leonard, P. Grinberg, *et al.* Systematic study of trace radioactive impurities in candidate construction materials for exo-200. *Nuclear Instruments and Methods in Physics Research Section A: Accelerators, Spectrometers, Detectors and Associated Equipment*, 591(3):pages 490 – 509, 2008. ISSN 0168-9002. URL: http://www.sciencedirect.com/science/article/pii/S016890020800346X.

[82] D. S. Akerib, X. Bai, *et al.* The LUX prototype detector: Heat exchanger development. *Nuclear Instruments and Methods in Physics Research A*, 709:pages 29–36, May 2013. e-Print: 1207.3665.

[83] D. Akerib, X. Bai, *et al.* Data acquisition and readout system for the {LUX} dark matter experiment. *Nuclear Instruments and Methods in Physics Research Section A: Accelerators, Spectrometers, Detectors and Associated Equipment*, 668(0):pages 1 – 8, 2012. ISSN 0168-9002. URL: http://www.sciencedirect.com/science/article/pii/S0168900211021073.

[84] S. Agostinelli, J. Allison, *et al.* GEANT4-a simulation toolkit. *Nuclear Instruments and Methods in Physics Research A*, 506:pages 250–303, 2003.

[85] J. Allison, K. Amako, *et al.* Geant4 developments and applications. *IEEE Transactions on Nuclear Science*, 53:pages 270–278, February 2006.

[86] D. S. Akerib, X. Bai, *et al.* LUXSim: A component-centric approach to low-background simulations. *Nuclear Instruments and Methods in Physics Research A*, 675:pages 63–77, May 2012. e-Print: 1111.2074.

[87] D. S. Akerib, H. M. Araujo, *et al.* Radiogenic and Muon-Induced Backgrounds in the LUX Dark Matter Detector. *ArXiv e-prints*, March 2014. e-Print: 1403.1299.

[88] A. Baldini, C. Bemporad, *et al.* Absorption of scintillation light in a 100 l liquid xenon γ-ray detector and expected detector performance. *Nuclear Instruments and Methods in Physics Research A*, 545:pages 753–764, June 2005. e-Print: physics/0407033.

[89] C. Silva, J. Pinto da Cunha, *et al.* A model of the reflection distribution in the vacuum ultra violet region. *Nuclear Instruments and Methods in Physics Research A*, 619:pages 59–62, July 2010. e-Print: 0910.1058.

[90] C. E. Dahl. *The physics of background discrimination in liquid xenon, and first results from XENON10 in the hunt for WIMP dark matter*. Ph.D. thesis, Princeton University, Jan. 2009. URL: http://gradworks.umi.com/33/64/3364532.html.

[91] T. Doke *et al.* LET dependence of scintillation yields in liquid argon. *Nucl. Instrum. Meth.*, A269:page 291, 1988.

[92] A. Mozumder. Free-ion yield and electron-ion recombination rate in liquid xenon. *Chem. Phys. Lett.*, 245:page 359, 1995.

[93] J. Thomas and D. A. Imel. Recombination of electron-ion pairs in liquid argon and liquid xenon. *Phys. Rev. A*, 36:page 614, 1987.

[94] I. M. Obodovskii and K. T. Ospanov. Scintillation output of liquid xenon for low-energy γ-quanta. *Instruments and Experimental Techniques*, 37:page 42, 1994.

[95] M. Yamashita, T. Doke, *et al.* Scintillation response of liquid Xe surrounded by PTFE reflector for gamma rays. *Nucl. Instrum. Meth.*, A535:page 692, 2004.

[96] E. Aprile *et al.* Simultaneous measurement of ionization and scintillation from nuclear recoils in liquid xenon for a dark matter experiment. *Phys. Rev. Lett.*, 97:page 081302, 2006.

[97] A. Manalaysay *et al.* Spatially uniform calibration of a liquid xenon detector at low energies using ^{83m}Kr. *Rev. Sci. Instrum.*, 81:page 073303, 2010. e-Print: 0908.0616.

[98] G. Plante *et al.* New measurement of the scintillation efficiency of low-energy nuclear recoils in liquid xenon. 2011. e-Print: 1104.2587.

[99] A. Manzur, A. Curioni, *et al.* Scintillation efficiency and ionization yield of liquid xenon for monoenergetic nuclear recoils down to 4 keV. *Phys. Rev. C*, 81:page 025808, 2010.

[100] M. Horn *et al.* Nuclear recoil scintillation and ionisation yields in liquid xenon from ZEPLIN-III data. *ArXiv e-prints*. e-Print: 1106.0694.

[101] A. Teymourian, D. Aharoni, *et al.* Characterization of the QUartz Photon Intensifying Detector (QUPID) for Noble Liquid Detectors. *Nucl.Instrum.Meth.*, A654:pages 184–195, 2011. e-Print: 1103.3689.

[102] A. Hitachi *et al.* LET dependence of the luminescence yield from liquid argon and xenon. *Nuclear Instruments and Methods in Physics Research*, 196:page 97, 1982. ISSN 0167-5087. URL: http://www.sciencedirect.com/science/article/pii/0029554X8290622X.

[103] D. Y. Akimov, V. Batyaev, *et al.* Liquid xenon for WIMP searches: Measurement with a two-phase prototype. pages 371–376, 2002.

[104] S. Kubota, A. Nakamoto, *et al.* Recombination luminescence in liquid argon and in liquid xenon. *Physical Review B*, 17:pages 2762–2765, 1978.

[105] K. Ueshimal. *Study of pulse shape discrimination and low background techniques for liquid xenon dark matter detectors*. Ph.D. thesis, University of Tokyo, Nov. 2010.

[106] J. Mock, N. Barry, *et al.* Modeling pulse characteristics in Xenon with NEST. *Journal of Instrumentation*, 9:T04002, April 2014. e-Print: 1310.1117.

[107] S. F.P., T. Dias, *et al.* Three-dimensional monte carlo calculation of the vuv electroluminescence and other electron transport parameters in xenon. *J. Phys. D: Appl. Phys.*, 27:pages 42–48, 1994. URL: http://iopscience.iop.org/0022-3727/27/1/007.

[108] S. Biagi. Magboltz - transport of electrons in gas mixtures, March 2011. URL: http://magboltz.web.cern.ch/magboltz/.

[109] J. Angle *et al.* First results from the xenon10 dark matter experiment at the gran sasso national laboratory. *Phys. Rev. Lett.*, 100:page 021303, 2008.

[110] P. Sorensen. *A Position-Sensitive Liquid Xenon Time-Projection Chamber for Direct Detection of Dark Matter: The XENON10 Experiment*. Ph.D. thesis, Brown University, May 2008.

[111] P. Sorensen *et al.* Lowering the low-energy threshold of xenon detectors. 2010. e-Print: 1011.6439.

[112] H. Koehler, L. Ferderber, *et al.* Vacuum-ultraviolet emission from high-pressure xenon and argon excited by high-current relativistic electron beams. *Physical Review A*, 9:pages 768–781, 1974.

[113] M. Woods. *A Comprehensive Study of the Large Underground Xenon Detector*. Ph.D. thesis, University of California, 2014.

[114] D. Akerib *et al.* The Large Underground Xenon (LUX) Experiment. *Nucl.Instrum.Meth.*, A704:pages 111–126, 2013. e-Print: 1211.3788.

[115] D. Akerib, H. Araujo, *et al.* Radiogenic and Muon-Induced Backgrounds in the LUX Dark Matter Detector. 2014. e-Print: 1403.1299.

[116] A. Smith. Homestake (dusel) samples - results of radiometric analyses at lbnl. Technical report, LBNL, 2007.

[117] D. Akerib, X. Bai, *et al.* An Ultra-Low Background PMT for Liquid Xenon Detectors. *Nucl.Instrum.Meth.*, A703:pages 1–6, 2013. e-Print: 1205.2272.

[118] C. Z. D. Mei. Neutron yield in materials <http://neutronyield.usd.edu>.

[119] D.-M. Mei, C. Zhang, and A. Hime. Evaluation of (alpha,n) Induced Neutrons as a Background for Dark Matter Experiments. *Nucl.Instrum.Meth.*, A606:pages 651–660, 2009. e-Print: 0812.4307.

[120] V. Kuz'minov, V. Novikov, *et al.* Radioactive85kr in krypton enriched with a light isotope. *Atomic Energy*, 73(6):pages 1010–1011, 1992. ISSN 1063-4258. URL: http://dx.doi.org/10.1007/BF00761444.

[121] L. Kastens, S. Bedikian, *et al.* A 83Krm Source for Use in Low-background Liquid Xenon Time Projection Chambers. *JINST*, 5:page P05006, 2010. e-Print: 0912.2337.

[122] *LUX Calibrations*, 2014. UCLA DM 2014.

[123] PandaX Collaboration, M. Xiao, *et al.* First dark matter search results from the PandaX-I experiment. *ArXiv e-prints*, August 2014. e-Print: 1408.5114.

[124] S. Uvarow. *Search for Low-Mass WIMPs with LUX*. Ph.D. thesis, University of California, in preparation.

[125] R. Barlow. Extended maximum likelihood. *Nuclear Instruments and Methods in Physics Research Section A: Accelerators, Spectrometers, Detectors and Associated Equipment*, 297(3):pages 496 – 506, 1990. ISSN 0168-9002. URL: http://www.sciencedirect.com/science/article/pii/0168900290913348.

[126] G. Cowan, K. Cranmer, *et al.* Asymptotic formulae for likelihood-based tests of new physics. *European Physical Journal C*, 71:page 1554, February 2011. e-Print: 1007.1727.

[127] L. Moneta, K. Cranmer, *et al.* The RooStats project. In *Proceedings of the 13th International Workshop on Advanced Computing and Analysis Techniques in Physics Research. February 22-27, 2010, Jaipur, India. http://acat2010.cern.ch/. Published online at <A href="http://pos.sissa.it/cgi-bin/reader/conf.cgi?confid=93">http://pos.sissa.it/cgi-bin/reader/conf.cgi?confid=93</A>, p.57*. 2010. e-Print: 1009.1003.

[128] R. Agnese, Z. Ahmed, *et al.* Silicon detector dark matter results from the final exposure of cdms ii. *Phys. Rev. Lett.*, 111:page 251301, Dec 2013. URL: http://link.aps.org/doi/10.1103/PhysRevLett.111.251301.